

IN SITU ANALYSIS OF AQUEOUS STRUCTURE AND ADSORPTION AT
FLUOROCARBON, HYDROCARBON AND MINERAL SURFACES

by

ADAM JUSTIN HOPKINS

A DISSERTATION

Presented to the Department of Chemistry
and the Graduate School of the University of Oregon
in partial fulfillment of the requirements
for the degree of
Doctor of Philosophy

September 2010

University of Oregon Graduate School

Confirmation of Approval and Acceptance of Dissertation prepared by:

Adam Hopkins

Title:

"In situ analysis of aqueous structure and adsorption at fluorocarbon, hydrocarbon and mineral surfaces"

This dissertation has been accepted and approved in partial fulfillment of the requirements for the Doctor of Philosophy degree in the Department of Chemistry by:

Thomas Dyke, Chairperson, Chemistry
Geraldine Richmond, Advisor, Chemistry
James Hutchison, Member, Chemistry
Mark Lonergan, Member, Chemistry
Qusheng Jin, Outside Member, Geological Sciences

and Richard Linton, Vice President for Research and Graduate Studies/Dean of the Graduate School for the University of Oregon.

September 4, 2010

Original approval signatures are on file with the Graduate School and the University of Oregon Libraries.

©September 2010

Adam Justin Hopkins

An Abstract of the Dissertation of

Adam J. Hopkins for the degree of Doctor of Philosophy

in the Department of Chemistry to be taken September 2010

Title: IN SITU ANALYSIS OF AQUEOUS STRUCTURE AND
ADSORPTION AT FLUOROCARBON, HYDROCARBON AND
MINERAL SURFACES

Approved:

Dr. Geraldine L. Richmond

Altering and controlling the properties of solid surfaces in aqueous or other liquid phase environments has been a sought after objective for decades. With the discovery of chemisorbed self-assembled monolayers, this dream has become a reality. Oxide and metal surfaces can now be readily coated with an array of commercially available products to produce a desired functionality. The presence of these coatings on solid surfaces affects properties of the interfacial region by altering interfacial electrostatic fields, changing the structure of interfacial water molecules and altering the interactions of adsorbed species.

This dissertation reports on *in situ* studies of adsorption at several solid/aqueous interfaces using vibrational sum-frequency spectroscopy, a surface specific technique.

These studies are augmented by the use of atomic force microscopy and contact angle goniometry to characterize the prepared surfaces and their interactions with adsorbates. The studies investigate how changes in the surface structure and chemistry, as well as the bulk aqueous phase, affect interfacial structure.

The studies within are primarily focused on the interactions of water with bare and functionalized fused silica and the relationship between the aqueous phase composition and the structure of fluorocarbon and hydrocarbon self-assembled monolayers. The variations in aqueous structure are then examined in detail using ionic strength controlled experiments to understand the direct interactions of water hydrophobically coated silica. This analysis is followed by an investigation of the competitive adsorption of methanol and water at fluorocarbon and hydrocarbon monolayers which show spectroscopic signatures of the interaction strength between fluorocarbons and hydrocarbons. Further studies are performed using butylammonium chloride to verify these spectroscopic signatures and reveal different molecular structures of adsorbed species at chemically different hydrophobic surfaces. Lastly, specific ion effects on the CaF_2 /water interface are shown using equilibrium and time-resolved sum-frequency spectroscopy. The results of all these studies have implications for an array of surface chemical applications from mineral flotation to biocompatibility.

This dissertation includes previously published co-authored material.

CURRICULUM VITAE

NAME OF AUTHOR: Adam Justin Hopkins

GRADUATE AND UNDERGRADUATE SCHOOLS ATTENDED:

University of Oregon, Eugene, Oregon
Florida State University, Tallahassee, Florida

DEGREES AWARDED:

Doctor of Philosophy in Chemistry, 2010, University of Oregon
Master of Science in Chemistry, 2007, University of Oregon
Bachelor of Science in Chemistry with Honors, 2002, Florida State
University

AREAS OF SPECIAL INTEREST:

Surface Analytical Chemistry, Materials Science, Laser Spectroscopy
Science Policy
Public Speaking and Presentation Skills

PROFESSIONAL EXPERIENCE:

Graduate Research Assistant, Department of Chemistry
University of Oregon, 2003 – 2010
Graduate Teaching Fellow, Department of Chemistry
University of Oregon, 2002 – 2003
Research Assistant, Department of Chemistry
Florida State University, 1999 – 2002

Teaching Assistant, Department of Chemistry
Florida State University, 2001 – 2002
Undergraduate Researcher
Oak Ridge National Laboratory, 2001

GRANTS, AWARDS AND HONORS:

Magna cum Laude, Florida State University, Tallahassee, Florida, 2002

Undergraduate Research Award (to an outstanding student in the field of chemistry), Florida State University, Tallahassee, Florida, 2002

Phi Beta Kappa, Florida State University, Tallahassee, Florida, 2000

PUBLICATIONS:

- Hopkins, A. J.; Richmond, G. L., "Sensitivity of vibrational sum-frequency spectroscopy to quality of self-assembled monolayers" *Langmuir*, in revision.
- Hopkins, A. J.; Shrödle, S.; Richmond, G. L., "Specific ion effects of salt solutions at the CaF₂/water interface" *Langmuir* **2010**, *26*, 10784-10790.
- Hopkins, A. J.; McFearin, C. L.; Richmond, G. L., "Investigations of the solid-aqueous interface with vibrational sum-frequency spectroscopy" *Current Opinion in Solid State and Materials Science* **2005**, *19*, 19-27.
- Fu, J. M.; Surapaneni, Y.; Hopkins, A. J.; Allen, S. D. "Analysis of contaminants on CaF₂ surfaces by infrared laser induced desorption" *Journal of Vacuum Science and Technology A* **2004**, *22*, 2126-2130.
- Allen, S.D.; Fu, J. M.; Surapaneni, Y.; Hopkins, A. J.; Davis, P. "Surface analysis by laser induced desorption time-of-flight mass spectrometry" *Proceedings of the SPIE* **2003**, *4977*, 1-9.

ACKNOWLEDGEMENTS

I would never have been able to finish this dissertation without the help of my advisor, Geri Richmond. Thanks for having the patience to see this through. I think I have done some interesting science and it is a shame this project is not being continued, because there are so many fascinating experiments that could be done. You have let me pursue my interests, sent me to meetings and helped me to develop my strengths and identify weaknesses.

To the group, past and present, it has been a blast. I have learned and taught so much in group meeting, subgroup, Friday lunch, etc. that would not have been possible without you; I am eternally grateful. Former members Kevin Becraft and Megan Leich ensured I knew what I was doing. A former postdoc, Simon Schrödle, was an inspiration to work with. Special thanks to Pat Blower, Stephanie Ota and Dan Beaman for helping in various capacities with this dissertation.

I want to single out my REUs for all their hard work; I have had some great summer students. Liz Surano (now Wittkop), Rachel Pollock and Brittany Willis all helped out with working out the kinks in monolayer deposition. Phil Cox, my current REU, has done some excellent work on a new project and chased down a false lead in Chapter 5!

Dad, thanks for coming out and visiting and for always being available for a grilling consultation. Without meat and fire, I do not think I could have made it. To my grandparents, aunts and uncles - this would not have been possible without you, not just for the obvious reasons, but because you have been amazingly supportive and understanding. I never knew how important everyone was to me until I moved across the country. This whole graduate school thing is for me, but it reflects on you. Thanks for encouraging me to be an independent thinker and tinkerer.

The cookouts, ultimate frisbee games, hikes, skiing excursions and near death experiences have made my time here most enjoyable. Thanks to all my friends for those and for crazy nights getting kicked out of Rennie's, Max's and Lucky's. Special thanks to Zack Mensinger for always being up for photography and trivia; Joe Henderson and my whole running group for keeping me thin and healthy; and my roommate, best friend, sister I never had and surrogate mother, Mary Smeller.

Finally, I want to thank my girlfriend, Jennifer. You're a wonderful woman. Thanks for putting up with my irritability these past months. Thanks for being willing to stay with a poor graduate student for nearly two years after you graduated. If we can handle this, we can handle anything. I love you.

To everyone I have left out: I offer my sincerest apologies, I have not meant to offend. There are a lot of names and they only allow two pages of acknowledgements.

To Dad, Grandmother and Medaddy,

To Grandma, I wish you could have seen this day.

TABLE OF CONTENTS

Chapter	Page
I. INTRODUCTION.....	1
II. OVERVIEW OF VIBRATIONAL SUM-FREQUENCY SPECTROSCOPY AND SPECTRAL ANALYSIS.....	8
Introduction.....	8
Vibrational Sum-Frequency Spectroscopy.....	9
Mathematical Background and Symmetry Considerations.....	9
Spectral Fitting.....	16
Contact Angle.....	20
Conclusion.....	22
III. EXPERIMENTAL CONSIDERATIONS.....	24
Vibrational Sum-Frequency Spectrometer System.....	24
Nanosecond Laser System.....	24
The Interface.....	27
Calibration and Normalization of Sum-Frequency Spectra.....	28
Coated Sample Preparation and Characterization.....	31
Materials.....	31
Substrate Preparation.....	32
Octadecylsilane Deposition.....	33
1H,1H,2H,2H-perfluorodecylsilane Deposition.....	34
Z Dol 4000 Deposition.....	35
Contact Angle Measurements.....	36
Atomic Force Microscopy.....	37
Conclusion.....	38

Chapter	Page
IV. INVESTIGATIONS OF MONOLAYER PREPARATION METHODS WITH VIBRATIONAL SUM-FREQUENCY SPECTROSCOPY	39
Introduction	40
Experimental	42
Monolayer Preparation	42
Sum-Frequency Generation	43
Results and Discussion.....	44
Hydrocarbon SAMs	44
Fluorocarbon SAMs	58
Conclusion	69
V. EFFECTS OF DIFFERENT HYDROPHOBIC COATINGS ON INTERFACIAL WATER STRUCTURE	71
Introduction	72
Experimental	74
Results and Discussion.....	75
SiO ₂ /Water Interface	77
SiO ₂ /ODS/Water Interface	85
SiO ₂ /FDS/Water Interface	89
SiO ₂ /Zdol/Water Interface	94
Conclusion	105
VI. FLUOROCARBON AND HYDROCARBON MONOLAYER INTERACTIONS WITH METHANOL	108
Introduction	109
Experimental	110
Results and Discussion.....	111
Fluorocarbon SAM/Methanol Interface: OH Region	111
Fluorocarbon SAM/Methanol Interface: CH Region	115

Chapter	Page
Hydrocarbon SAM/Methanol Interface.....	126
Conclusion	129
VII. FLUOROCARBON AND HYDROCARBON MONOLAYER INTERACTIONS WITH BUTYLAMINE HYDROGEN CHLORIDE ...	131
Introduction.....	132
Experimental	133
Results and Discussion.....	135
VSFS of BuNH ₃ Cl Adsorption at pH 2: FDS	136
VSFS of BuNH ₃ Cl Adsorption at pH 2: ODS.....	142
VSFS of BuNH ₃ Cl Adsorption at pH 5.7	147
Contact Angle and Interfacial Tension Measurements.....	149
Conclusions	156
VIII. SPECIFIC ION ADSORPTION AT THE CaF ₂ /WATER INTERFACE.....	159
Introduction.....	160
Experimental	162
Laser System.....	162
Sample Preparation	163
Results and Discussion.....	164
Solution Equilibrium Structure	164
Ion Kinetics at the CaF ₂ /Water Interface	175
Conclusions	183
IX. CONCLUSIONS.....	185
APPENDIX: METHANOL ORIENTATION CALCULATION	188
BIBLIOGRAPHY.....	195

LIST OF FIGURES

Figure	Page
2.1. Laboratory frame with $C_{\infty v}$ symmetry.....	12
2.2. Interference effects in VSFS spectra	18
2.3. Illustration of water drop contact angle.....	20
3.1. Schematic of the nanosecond VSFS laser system	25
3.2. Sample setup for a VSFS experiment on a hydrophobic surface.....	27
3.3. IR output in a VSFS scan.....	30
3.4. Molecules used for coating substrates.....	32
3.5. Surface pressure isotherm of FDES	34
4.1. AFM images of a bare glass substrate and ODS monolayers	45
4.2. VSFS spectra of HQODS and LQODS monolayers in air	48
4.3. VSFS spectra of HQODS monolayer/ D_2O and LQODS monolayer/ D_2O interfaces	50
4.4. SSP amplitude ratios for HQODS and LQODS	51
4.5. Spectra of HQODS/water and LQODS/water interfaces.....	53
4.6. Tapping mode AFM images of three FDS monolayers on $SiSiO_2$ wafer substrates	60
4.7. VSFS spectra of the FDS/air interface	61
4.8. SSP spectra of FDS12, FDS17 and LIQFDS monolayers in D_2O	63
4.9. Fit amplitude ratios of the two CH_2 peaks of FDS12, FDS17 and LIQFDS	63
4.10. Spectra of FDS12, FDS17 and LIQFDS monolayer/water interfaces	65
5.1. VSFS spectra of the SiO_2/H_2O interface at different pH values.....	77
5.2. VSFS spectra of the SiO_2/H_2O interface at pH 5.8 with NaCl	79
5.3. VSFS spectrum of the neat SiO_2/H_2O interface with two different fitting schemes	83
5.4. VSFS spectra of the $SiO_2/ODS/H_2O$ at pH 2, 7 and 11	85
5.5. VSFS spectra of the $SiO_2/ODS/H_2O$ interface at pH 5.8 with NaCl	87
5.6. VSFS spectra of the FDS/water interface at pH 2, 7 and 11	89

Figure	Page
5.7. VSFS spectra of the FDS/water interface at pH 5.8 with NaCl	91
5.8. VSFS spectra of the Zdol/water interface at selected pH values	94
5.9. VSFS spectra of the Zdol/water interface at pH 5.8 with NaCl	96
5.10. Nonlinear peak fitting amplitudes of SiO ₂ and Zdol samples	98
5.11. Zdol VSFS signal as a function of water exposures	101
5.12. Water contact angle of Zdol, FDS and ODS	102
5.13. AFM scans of Zdol coated GE-124 glass	104
6.1. VSFS spectra of neat CH ₃ OH/FDS and H ₂ O/FDS interfaces	112
6.2. SFS of the FDS/CH ₃ OH:H ₂ O solution interface	113
6.3. Amplitude and location of the free-OH peak at different molar percentages of CH ₃ OH	114
6.4. SSP and PPP polarized VSFS spectra of CH ₃ OD:D ₂ O/FDS interface	116
6.5. VSFS spectra of FDS in D ₂ O and CD ₃ OD	118
6.6. Peak location of the CH ₃ (ss) at the FDS interface	119
6.7. CH ₃ OH bonding environment	120
6.8. Fit amplitude ratio of the CH ₃ (ss) peak at the FDS surface	121
6.9. Methanol adsorption isotherm on FDS	122
6.10. Amplitude of free-OH mode versus effective surface number density of CH ₃ OH	126
6.11. VSFS spectra of CH ₃ OD:D ₂ O/ODS interface	127
6.12. VSFS spectra of an ODS/D ₂ O and ODS/CD ₃ OD interface	128
7.1. Isotopomers of BuNH ₃ Cl used	135
7.2. Spectra of BuND ₃ Cl on the FDS surface in pD 2 D ₂ O	137
7.3. SPS spectra of BuND ₃ Cl on the FDS surface in pD 2 D ₂ O	139
7.4. Amplitude ratio as a function of BuND ₃ Cl concentration at pD 2 on FDS	140
7.5. VSFS spectra of d ₉ -BuNH ₃ Cl adsorbing onto an FDS monolayer in pH 2 HCl	141
7.6. Spectra of the CH and OH stretching region of an ODS monolayer with d ₉ -BuNH ₃ Cl at pH 2	143
7.7. SSP and SPS spectra of an ODS monolayer with BuND ₃ Cl	144
7.8. Amplitude of CH ₃ (ss) and CH ₃ (as) stretches	146
7.9. VSFS spectra of the FDS/BuNH ₃ Cl(aq) interface at pH 5.7	147

Figure	Page
7.10. VSFS spectra of the ODS/BuNH ₃ Cl(aq) interface at pH 5.7	147
7.11. Static contact angle measurements of aqueous BuNH ₃ Cl solutions on ODS and FDS.....	150
7.12. Interfacial tension measurements of aqueous BuNH ₃ Cl	151
7.13. Solid-liquid interfacial tension of ODS and FDS monolayers with BuNH ₃ Cl	154
7.14. Possible confirmations of BuNH ₃ Cl	155
8.1. VSFS spectra of aqueous NaCl solutions at the CaF ₂ surface.....	166
8.2. VSFS spectra of aqueous NaBr solutions at the CaF ₂ surface	168
8.3. VSFS spectra of aqueous NaF at the CaF ₂ surface.....	169
8.4. VSFS spectra of 0.1 M NaF, 0.1 M Na ₂ SO ₄ and 1 M CaCl ₂ solutions	170
8.5. VSFS spectra of aqueous Na ₂ SO ₄ at the CaF ₂ surface	173
8.6. VSFS spectra of the CaF ₂ /CaCl ₂ (aq) interface	174
8.7. VSFS signal monitored over time for NaBr, NaCl and Na ₂ SO ₄ at CaF ₂ /water interface	176
8.8. VSFS signal monitored over time for NaF at CaF ₂ /water interface	178
8.9. VSFS signal monitored over time for CaCl ₂ at CaF ₂ /water interface	180
9.1. VSFS geometry used to define beam angles.....	190

LIST OF TABLES

Table	Page
5.1. Fitting parameters for two models used to describe the SiO ₂ /H ₂ O interface	82
6.1. Comparison of CH ₃ OH and H ₂ O at FDS, ODS and air interfaces.....	129
7.1. Parameters from contact angle and surface tension measurements of BuNH ₃ Cl solutions	153
8.1. Fitting parameters for H ₂ O and salt solutions at the CaF ₂ surface.....	167

CHAPTER I

INTRODUCTION

The properties of the wall or canvas dictate what paints can be used. A mere fingerprint can prevent the formation of a patina on bronze. Perhaps most notably, construction in ancient Egypt could not have been done without copious amounts of lard to enhance the sliding of great rocks and statues. Esoterically, the degree to which socks stay up is dependant on the material and coating's interactions with skin and is a subject in therapeutic research.[1] These are just a few examples of processes that are affected by surface properties.

One of the common ways of modifying surface properties is through the use of monolayer chemistry. Irving Langmuir pioneered this chemistry making when he discovered that hydrophobic molecules spread over a liquid surface in a molecularly thin layer.[2] Monolayer chemistry has found wide use as thin coatings of surfactants, polymers and silanes on solid surfaces are used in industrial applications from the very large (e.g. mineral flotation)[3-5] to the very small (microelectromechanical devices).[6-8] The choice of composition of the thin surface coating depends on the desired properties: surface energy, thermal stability, dielectric constant, etc. Increasingly, many of the properties desired in modern applications are provided by fluorocarbon materials.

Fluorocarbon coatings, relative to their hydrocarbon counterparts, have different molecular structures and lower surface energies as shown in the foundational work of Zisman et al.[9–12] Superior thermal, chemical and dielectric stability have led to numerous investigations into fluorocarbon applications.[8, 13–24] The principle focus of this dissertation is to enhance the molecular level understanding of some of the unique properties of fluorocarbon surfaces, such as their hydrophobic and lipophobic nature. To do this, one needs to understand the interfacial interactions of adsorbates with these fluorinated surfaces and compare and contrast them with hydrocarbons.

Self-assembled monolayers and vibrational sum-frequency spectroscopy (VSFS) provide an ideal testing ground and investigative tool for directly observing such interactions. Silane self-assembled monolayer (SAM) chemistry has been extensively studied[25–35] since the seminal works of Sagiv et al. describing silane SAM formation.[36–40] These surfaces provide durable, uniform, transparent coatings for investigating interfacial adsorption phenomena. VSFS has been applied to silane and other monolayers since its development in the 1980s by Shen et al.[41–44] This technique is an ideal tool for these studies because it is inherently surface specific and can provide molecular level information on the structure, orientation and chemical bonding environments of species in the interfacial region.[45–47] The surface specificity of VSFS makes it particularly valuable because the buried solid/liquid interface can be examined *in situ* without the need to remove large signals originating from the bulk molecules. This sets apart VSFS from other surface analytical

techniques, which often require high vacuum and may be destructive to the samples. Using VSFS both the solid and adsorbed phase can be simultaneously investigated. The studies within combine the spectroscopic power of VSFS with atomic force microscopy and contact angle goniometry to build a more complete picture of the chemistry and fundamental properties of these interfaces.

The investigations within this manuscript examine the orientation, conformation and electrostatics of adsorption processes at fluorocarbon and hydrocarbon SAMs as well as two mineral surfaces, SiO_2 and CaF_2 . The theoretical principles behind the studies and techniques used are discussed in Chapter II. The discussion in this chapter begins with a short explanation of the theory of VSFS and the information that can be gained from it. Because of the complexity of analysis of VSFS data, the process of spectral analysis is also discussed with particular attention paid to interference effects between different vibrational modes. Following these sections, a brief discussion of contact angle measurements ensues. Additionally mathematical formalisms for describing adsorption processes are explained as needed within the text.

The high field strengths necessary for VSFS generation require a pulsed infrared and visible light source; these are provided by a custom built laser system that is described in Chapter III. This chapter also describes the basic operating parameters for the instrumentation used and the standard procedures used in collecting and analyzing data. The chapter concludes with a discussion of the types of samples used

and details on the preparation methodology. Basic analysis of the samples validating the methods is presented as well. Analysis of monolayer samples prepared by these and other methods is carried out in Chapter IV.

The data sections of this dissertation begin with Chapter IV, in which the sensitivity of VSFS to monolayer structure is evaluated. Because the vast majority of the work discussed within relies on custom made samples, establishing the best methods for sample preparation was necessary. Silane monolayer formation is highly sensitive to a variety of parameters and “best” methods for monolayer preparation vary within the literature, even for the same molecule. To evaluate different preparation methods studied, hydrocarbon and fluorocarbon monolayers were produced via multiple pathways and the results were analyzed using water contact angle measurements to establish surface coverage and atomic force microscopy (AFM) to examine the surface morphology. These measurements are correlated with VSFS data to show that direct measurement of the monolayer vibrational modes is surprisingly uncorrelated to the surface morphology. The behavior of interfacial water molecules, however, is quite sensitive to the differences in the coating structure. Differences in the interfacial water structure are observed and noted, leading to the investigations in the following chapter.

Chapter V uses the developed synthetic routes to produce monolayers and carefully study their interactions with water. These interactions are compared to bare fused silica and a thin coating of Fomblin Z dol perfluoropolyether. Two types of

VSFS studies are performed here. The first is ionic strength controlled pH titrations, which vary the surface charge but keep the charge screening depth constant. The second is an ionic strength titration, which leaves the surface charge constant but compresses the electric double layer. These studies show that interfacial bonding is significantly different at all three of the hydrophobic surfaces studied in this chapter. The results in this chapter also show that the origin of the electrostatic charge at these surfaces is primarily due to ions at the interface, not deprotonation of the SiO_2 substrate. Additionally, these experiments show small but significant changes in the spectroscopy of the Z dol coating over time, which were investigated further with VSFS, AFM and contact angle measurements. The results in this chapter have been submitted for publication and are currently under revision.

Having established differences in the interfacial behavior of water at fluorocarbon and hydrocarbon surfaces, attention is now turned to adsorption of organic compounds and how they compare these two surfaces. Chapter VI is the first of two such studies described in this document and covers the adsorption of methanol from aqueous solutions. From the VSFS studies, it is determined that methanol is preferentially adsorbed at hydrophobic interfaces. Using these data, the methanol adsorption isotherm and free energy has been calculated and compared to values in the literature showing that methanol behaves quite similarly at fluorocarbon, hydrocarbon and air interfaces. The results also show clear differences in the interfacial frequency of methanol at the different interfaces.

Organic adsorption studies are continued using butylamine HCl solutions in Chapter VII at bulk pHs yielding nearly neutral and negatively charged interfaces. Using a series of isotopically substituted butylamines, the effect of adsorption on both monolayer and water structure were studied with VSFS to reveal that adsorption begins before it is detected in contact angle measurements. Contact angle results were combined with surface tension data to calculate the free energy of adsorption. The differences in the free energy help explain the spectroscopic differences of the adsorbate between the two surfaces.

The final data chapter, Chapter VIII, is a departure from the monolayer studies in the previous chapters. In this chapter, ion specific effects on the interfacial water structure at a calcium fluoride surface are studied. The ionic strength studies in Chapter V rely on non-specific adsorption phenomena; however, semi-soluble materials such as calcium fluoride can be affected by ions in solution other than H^+ and OH^- . This study reveals information important in understanding ion effects on surfactant adsorption at this interface using both equilibrium and nonequilibrium VSFS measurements. The results in this chapter have been published with coauthors Simon Schrödle and Geraldine Richmond in *Langmuir*.

The interfacial systems presented in chapters IV-VIII are model systems for investigating fundamental differences between molecular interactions at solid/liquid interfaces. The monolayer studies in chapters IV-VII build a complete case for the differences in the interfacial structure and bonding at fluorocarbon and hydrocarbon

interfaces. Chapter VIII takes the ion studies in Chapter V one step farther by examining ion specific adsorption, which is known to affect surfactant adsorption. The studies encompassed within this document greatly enhance the fundamental understanding of molecular adsorption at solid/liquid interfaces.

CHAPTER II

OVERVIEW OF VIBRATIONAL SUM-FREQUENCY SPECTROSCOPY AND SPECTRAL ANALYSIS

Introduction

Vibrational sum-frequency spectroscopy (VSFS) is a surface specific, nonlinear optical technique[48] that has been widely applied to aqueous interfacial systems.[45, 46, 49, 50] VSFS was first predicted by Bloembergen and Pershen in 1962[51] and experimentally verified by Shen et al in 1987.[41, 42] In experimental practice VSFS response is generated by coupling two high intensity laser sources in space and time at an interface between two immiscible phases. One of the laser sources is a fixed frequency visible beam (ω_{vis}) and the other is a tunable infrared beam (ω_{IR}). These two beams generate a third beam (ω_{sfg}) at the sum of the two incident frequencies. By tuning the infrared beam through a molecular vibrational transition, a vibrational spectrum of the molecule is produced. The principle advantage of VSFS is its ability to investigate buried interfaces without the production of large signal from the bulk media. The frequency dependence of the VSFS response is unique to those molecules in the interfacial region, which allows for the characterization of interfacial structure and bonding. Furthermore, because VSFS is a coherent molecular process, the

signal is polarization encoded and can be used to give detailed molecular orientation information.

Vibrational Sum-Frequency Spectroscopy

Mathematical Background and Symmetry Considerations

The electron clouds of molecules respond to low intensity electromagnetic radiation by oscillating harmonically with it. In condensed media, this is referred to as the polarization of the medium. However, with high intensity electromagnetic fields, this harmonic approximation breaks down leading to the induced polarization no longer being linear, but rather described by a power series expansion in the electric field, $\vec{E}(\omega)$, as in Equation II.1 below.

$$\vec{P}(\omega) = \vec{P}^{(0)} + \epsilon_0 \left(\vec{\chi}^{(1)} \vec{E}(\omega) + \vec{\chi}^{(2)} \vec{E}(\omega) \vec{E}(\omega) + \vec{\chi}^{(3)} \vec{E}(\omega) \vec{E}(\omega) \vec{E}(\omega) + \dots \right) \quad (\text{II.1})$$

$\vec{P}^{(0)}$ is the static polarization and is not present in many materials and is typically very small. ϵ_0 is the permittivity of free space. $\vec{\chi}^{(n)}$ are the susceptibilities of the medium describing the optical response of the medium to the incident electric field. These $\vec{\chi}^{(n)}$ terms contain the frequency dependence and Fresnel coefficients associated with the medium and system geometry. The first order term, $\vec{\chi}^{(1)} \vec{E}(\omega)$ is responsible for the everyday effects of reflection and refraction. The higher order terms become significant when the incident field is large; this is the case in VSFS.

In the case of sum-frequency generation, the second order nonlinear susceptibility, $\overset{\leftrightarrow}{\chi}^{(2)}$, couples two incident fields with distinct frequencies, ω_1 and ω_2 . The relevant component of the second order nonlinear polarization can be written as:

$$\vec{P}^{(2)}(\omega_{sf}) = \epsilon_0 \overset{\leftrightarrow}{\chi}_{sf}^{(2)} \vec{E}(\omega_1) \vec{E}(\omega_2) \quad (\text{II.2})$$

These second order processes are forbidden under the dipole approximation in any centrosymmetric (possesses inversion symmetry) media.[48] When this symmetry breaks, such as at an interface; the process is allowed. Thus, molecules feeling the effects of an interface can be sum-frequency active and generate VSFS response. It is important to note that in the case of high static electric fields, such as at charged interfaces, $\overset{\leftrightarrow}{\chi}^{(3)}$ effects can contribute to the overall VSFS response.[52–54] This effect takes the form of:

$$\vec{P}^{(3)}(\omega_{sf}) = \epsilon_0 \overset{\leftrightarrow}{\chi}_{sf}^{(3)} \vec{E}(\omega_1) \vec{E}(\omega_2) \vec{E}(\omega_0) \quad (\text{II.3})$$

where $\vec{E}(\omega_0)$ is the static electric field. $\overset{\leftrightarrow}{\chi}^{(3)}$ effects may be caused by several factors including the nonlinear electronic polarizability, $\vec{\alpha}^{(3)}$, the alignment of molecules by the electrostatic field and the magnitude of the field itself. The presence of a large electrostatic field aligns polarizable interfacial molecules, such as water; removing the centrosymmetry and allowing more molecules to contribute to the nonlinear polarization.[53] The implications of this effect will be discussed further in Chapter V.

Equation II.2 completely describes the second order optical response of the material due to the incident electric fields. The second order susceptibility, $\overset{\leftrightarrow}{\chi}_{sf}^{(2)}$,

is a third rank tensor comprised of 27 elements. Each of these elements involves the response along the Cartesian coordinates of the individual electric fields at the interface in the lab frame. This expression can be fully expanded for the lab frame where x and y are the interfacial plane and the z-axis is perpendicular to the plane of the interface.

$$\begin{bmatrix} P_x^{(2)} \\ P_y^{(2)} \\ P_z^{(2)} \end{bmatrix} = \epsilon_0 \begin{bmatrix} \chi_{xxx} & \chi_{xxy} & \chi_{xxz} & \chi_{xyx} & \chi_{xyy} & \chi_{xyz} & \chi_{xzx} & \chi_{xzy} & \chi_{xzz} \\ \chi_{yxx} & \chi_{yyx} & \chi_{yxz} & \chi_{yyz} & \chi_{yyy} & \chi_{yyz} & \chi_{yzx} & \chi_{yzy} & \chi_{yzz} \\ \chi_{zxx} & \chi_{zxy} & \chi_{zxz} & \chi_{zyx} & \chi_{zyy} & \chi_{zyz} & \chi_{zzx} & \chi_{zzz} & \chi_{zzz} \end{bmatrix} \times \begin{bmatrix} E_x(\omega_1)E_x(\omega_2) \\ E_y(\omega_1)E_x(\omega_2) \\ E_z(\omega_1)E_x(\omega_2) \\ E_x(\omega_1)E_y(\omega_2) \\ E_y(\omega_1)E_y(\omega_2) \\ E_z(\omega_1)E_y(\omega_2) \\ E_x(\omega_1)E_z(\omega_2) \\ E_y(\omega_1)E_z(\omega_2) \\ E_z(\omega_1)E_z(\omega_2) \end{bmatrix} \quad (\text{II.4})$$

At liquid interfaces, the x and y axes are interchangeable by rotation about the z-axis, as shown in Figure 2.1. This $C_{\infty v}$ symmetry, reduces the 27 elements in the $\vec{\chi}_{sfg}^{(2)}$ tensor to seven non-zero elements, four of which are unique and are shown in Equation II.5.

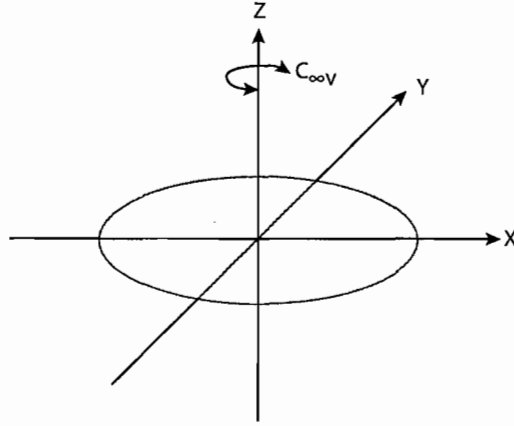


Figure 2.1. Laboratory reference frame with $C_{\infty v}$ symmetry about the z-axis. The interface is in the xy plane.

$$\begin{aligned}
 \overset{\leftrightarrow}{\chi}_{xxz}^{(2)} &= \overset{\leftrightarrow}{\chi}_{yyz}^{(2)} \\
 \overset{\leftrightarrow}{\chi}_{xzx}^{(2)} &= \overset{\leftrightarrow}{\chi}_{yzy}^{(2)} \\
 \overset{\leftrightarrow}{\chi}_{zxx}^{(2)} &= \overset{\leftrightarrow}{\chi}_{zyy}^{(2)} \\
 \overset{\leftrightarrow}{\chi}_{zzz}^{(2)} &
 \end{aligned} \tag{II.5}$$

These are the only elements that can lead to sum-frequency generation.[47] The intensity of the sum-frequency response is connected to the $\overset{\leftrightarrow}{\chi}^{(2)}$ elements through the square of the second order polarization through the following proportionality where a host of constants (pulse widths, the speed of light, permittivity of free space, etc.) have been omitted for clarity:

$$I_{sfg} \propto |P^{(2)}(\omega_{sfg})|^2 \propto \left| \overset{\leftrightarrow}{\chi}_{ijk}^{(2)} \vec{E}_j(\omega_{vis}) \vec{E}_k(\omega_{IR}) \right|^2 \tag{II.6}$$

Access to each of the four non-zero tensor elements is provided by selecting

specific polarization combinations of the sum frequency, visible and infrared light. Incorporating the nonlinear and linear Fresnel coefficients, $\tilde{f}_s \tilde{f}_g \tilde{f}_{vis} \tilde{f}_{IR}$, which describe the intensity of the transmitted and reflected beams as governed by the refractive indices of the two media, the following expressions for the intensity of the VSFS can be generated:[55, 56]

$$\begin{aligned}
I_{ssp}(\omega_3) &\propto |\tilde{f}_y \tilde{f}_y \tilde{f}_z \vec{E}(\omega_{vis}) \vec{E}(\omega_{IR}) \chi_{xxz}^{(2)}|^2 \\
I_{sps}(\omega_3) &\propto |\tilde{f}_y \tilde{f}_z \tilde{f}_y \vec{E}(\omega_{vis}) \vec{E}(\omega_{IR}) \chi_{zzx}^{(2)}|^2 \\
I_{ppp}(\omega_3) &\propto |\tilde{f}_x \tilde{f}_x \tilde{f}_z \vec{E}(\omega_{vis}) \vec{E}(\omega_{IR}) \chi_{xxz}^{(2)} + \tilde{f}_x \tilde{f}_z \tilde{f}_x \vec{E}(\omega_{vis}) \vec{E}(\omega_{IR}) \chi_{xxz}^{(2)} + \\
&\quad \tilde{f}_z \tilde{f}_x \tilde{f}_x \vec{E}(\omega_{vis}) \vec{E}(\omega_{IR}) \chi_{zzx}^{(2)} + \tilde{f}_z \tilde{f}_z \tilde{f}_z \vec{E}(\omega_{vis}) \vec{E}(\omega_{IR}) \chi_{zzz}^{(2)}|^2 \quad (\text{II.7})
\end{aligned}$$

in which s and p subscripts denote the polarization of the sum-frequency, visible and infrared light relative to the interfacial plane. s designates that the electric field oscillates in the plane and p denotes oscillations normal to the plane of incidence. Thus, by selecting the polarizations of the input beams and the detected signal, specific components of $\chi^{(2)}$ and therefore vibrational modes of a specific orientation relative to the interface can be probed. Transition dipole moments that have components perpendicular to the interface are probed in the *SSP* polarization combination. Those transition dipole moment components parallel to the interfacial plane are probed in *SPS*. As can be seen in Equation II.7, the *PPP* polarization scheme probes all four of the non-zero components of $\chi^{(2)}$.

The individual elements of $\chi^{(2)}$ can be broken down into contributions originating

from two sources: a resonant and a nonresonant component, as shown in Equation II.8.

$$I_{sfg} \propto \left| P_{sfg}^{(2)} \right|^2 \propto \left| \chi_{NR}^{(2)} e^{i\phi_{NR}} + \sum_v \chi_{Rv}^{(2)} e^{i\phi_v} \right|^2 I_{vis} I_{IR} \quad (\text{II.8})$$

The nonresonant component, $\chi_{NR}^{(2)}$ depends on the polarizability of the molecules at the interface and is influenced by the static electric field of a charged interface.[57] The resonant component, $\chi_{Rv}^{(2)}$, arises when the frequency of the incident IR light is close to that of a vibrational mode of an interfacial molecule. The resonant response is an orientationally averaged sum of all of the sum-frequency active vibrational modes of that molecule. The terms I_{vis} and I_{IR} are the intensities of the visible and infrared beams, respectively. The coherent nature of the sum-frequency response gives rise to phase factors for the resonant ($e^{i\phi_v}$) and nonresonant ($e^{i\phi_{NR}}$) components and leads to interference effects between vibrational modes and the nonresonant background.

The macroscopic properties of the resonant component, $\chi_{Rv}^{(2)}$, found in Equation II.8 are related to the vibrational modes of interfacial molecules by the orientational average of the molecular hyperpolarizability, $\left\langle \vec{\beta}_v \right\rangle$, and the number of molecules (N) at the interface.[58]

$$\chi_{Rv}^{(2)} = \frac{N_v}{\varepsilon \varepsilon_0} \left\langle \vec{\beta}_v \right\rangle \quad (\text{II.9})$$

In Equation II.9, ε is the relative dielectric constant of the interface and ε_0 is the vacuum permittivity. The hyperpolarizability contains the overall vibrational and orientational information about interfacial species. The molecular expression for the

hyperpolarizability has been derived from perturbation theory and can be written as:

$$\vec{\beta}_{lmn,v}^{\leftrightarrow} = \frac{\langle g | \alpha_{lm} | v \rangle \langle v | \mu_n | g \rangle}{2\hbar(\omega_v - \omega_{IR} - i\Gamma_v)} \quad (\text{II.10})$$

when the visible light is far from electronic resonance and only electric dipole transitions are considered.[48] The subscripts l, m, n refer to coordinates in the molecular frame. The Raman transition probability, α_{lm} , and the infrared transition dipole, μ_n , are in the numerator and dictate that for a vibrational mode to be sum-frequency active, it must be both IR and Raman active. The denominator assumes Lorentzian linewidth and shows the resonant enhancement of sum-frequency. When ω_{IR} matches ω_v , the IR transition frequency, the denominator becomes very small, which enhances the magnitude of β . Γ_v is the transition damping constant.

The microscopic resonant hyperpolarizability in Equation II.10 can be substituted into Equation II.9 following transformation from the molecular frame to the lab frame. This is accomplished by a Euler transformation for each element of β . After transforming and taking the orientational average, an expression for the macroscopic nonlinear susceptibility can be obtained:

$$\chi_{Rv}^{(2)} = \frac{N_v}{\epsilon\epsilon_0} \frac{M_{IJ}A_K}{(\hbar\omega_v - \hbar\omega_{IR} - i\Gamma_v)} \quad (\text{II.11})$$

in which M_{IJ} is the Raman transition probability and A_K is the IR transition dipole moment matrix element. Thus, the VSFS intensity can be written as:

$$I_{sfg} \propto \left| \chi_{NR}^{(2)} e^{i\phi_{NR}} + \sum_v N_v \frac{M_{IJ}A_K}{(\hbar\omega_v - \hbar\omega_{IR} - i\Gamma_v)} e^{i\phi_v} \right|^2 I_{vis} I_{IR} \quad (\text{II.12})$$

As can be seen from Equation II.12, the sum-frequency signal is dependant on the IR and Raman transition strength, the number of molecules excited and their orientation. This expression forms the basis for the analysis of VSFS spectra through spectral fitting, described in the next section.

Spectral Fitting

A distinguishing feature of VSFS, and nonlinear spectroscopies in general, is coherence. This arises because the nonlinear susceptibility is complex, with every component having an amplitude and phase. When the terms are summed and then squared, as in Equation II.12, to attain the VSFS intensity, interferences arise between the resonant terms with each other and the nonresonant background, complicating spectral interpretation. However, these interferences can result in unique lineshapes that make it easier to assign certain vibrational modes because of known phase relationships between them. This information may be used further to understand the relative orientation of interfacial molecules. More sophisticated analyses can be employed using the symmetry of vibrational modes and different polarization schemes to calculate absolute molecular orientations.[49, 59–62] One such analysis is shown in Appendix 1.

Analysis of VSFS spectra begins with normalization (for experimental details see Chapter III) and then spectral fitting. Spectra must be fit to deconvolve the resonant modes and nonresonant background from each other. The resonant modes contain information on the orientation, strength of bonding and molecular environment of

interfacial species and accurate assignment is imperative. For example, shifts in bond frequency indicate changes in the bonding environment while relative amplitudes can indicate orientation. Spectral fits are based on Equation II.12, using an analytical routine developed in our laboratory and modeled after the procedure initially introduced by Bain et al.[63, 64] The equation used to deconvolve VSFS spectra is:

$$\left| \chi_{eff}^{(2)} \right|^2 = \left| \chi_{NR}^{(2)} e^{i\phi_{NR}} + \sum_{i=0}^n A_i e^{i\phi_i} \int_0^{\infty} \frac{1}{\omega_i - \omega_{IR} + i\Gamma_{L_i}} e^{\left(-\frac{\omega_i - \omega_{IR}}{\Gamma_{\gamma_i}} \right)^2} d\omega_i \right|^2 \quad (\text{II.13})$$

The principle components of this equation are the nonresonant background, $\chi_{NR}^{(2)}$ and its associated phase, ϕ_{NR} ; and the sum of all the resonant vibrational modes. This resonant vibrational response convolves the homogenous linewidth of the transition, Γ_i , with a Gaussian expression to account for inhomogenous broadening (Γ_{γ_i}) due to the wide array of intermolecular environments experienced by condensed phase molecules. A_i is an amplitude term representing the effective strength of the sum-frequency transition, the number of molecules in the transition and their orientation. The center frequencies of the Lorentzian and Gaussian bands are given by ω_i and ω_{γ_i} , respectively.

Examples of typical interferences that occur in VSFS spectra are shown in Figure 2.2. There are two closely spaced, narrow modes at 2915 cm^{-1} and 2955 cm^{-1} as well as a broad mode at 3200 cm^{-1} . The two narrow modes are typical of CH stretching modes and have Gaussian widths of 7 cm^{-1} and Lorentzian widths of 2 cm^{-1} . The broad mode is typical of that seen in for water at solid/liquid interfaces

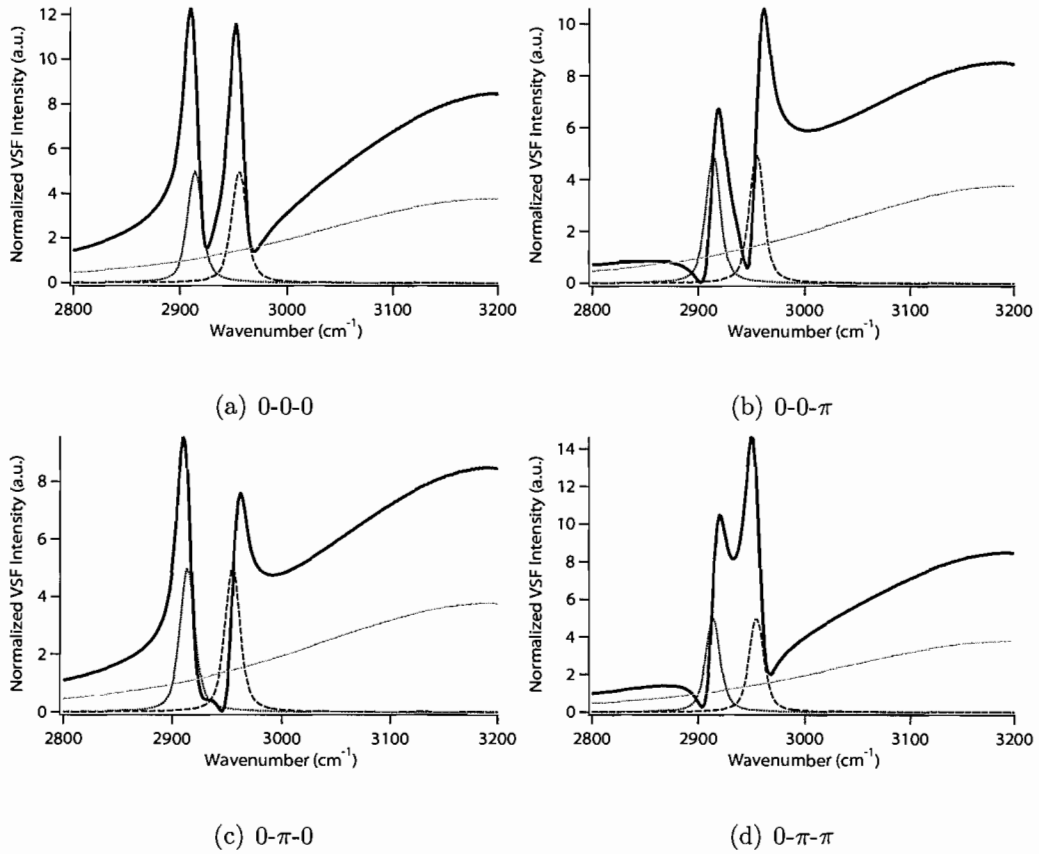


Figure 2.2. Examples of interference effects in VSFS spectra. The figures represent the four unique interferences for the this three resonant peak system. The solid line is the simulated experimental data and the dotted and grey lines are the resonant contributions to the spectrum. The phases of the peaks, in order of wavelength are shown underneath the individual figures.

and has a Lorentzian linewidth of 5 cm^{-1} and a Gaussian width of 200 cm^{-1} as is typical of interfacial water modes studied in this dissertation. The amplitude of all the peaks is set to 3. The thick black line in the subfigures is the simulated spectra derived from Equation II.13 for these three peaks. The four panels show the unique phase combinations of the resonant modes, listed in order of wavelength. For simplicity, the non-resonant signal is not considered in these figures.

Figures 2.2a and 2.2b show the physical effects on the VSFS spectra of a phase change from 0 to π of the 3200 cm^{-1} peak, when both of the CH modes have phases of 0. This phase change has a large effect on the overall shape of the VSFS spectra. When the broad mode is in phase with the two narrow modes, there are destructive interferences near 2920 cm^{-1} and 2960 cm^{-1} from the overlap of the modes. When the broad mode is out of phase, the destructive interference shifts to near 2900 cm^{-1} and 2950 cm^{-1} . Figures 2.2c and 2.2d show the same phase change of the broad mode, but with the two narrow modes having phases of 0 and π . In this case, there is constructive interference below 2900 cm^{-1} and near 3000 cm^{-1} , with a large destructive interference between the two narrow modes. This is reversed in Figure 2.2d when the phase of the broad mode is changed from 0 to π . The phase angle contains information about the relative orientation of interfacial species; for example, the changing of the broad mode from 0 to π indicates that the orientation of the molecules represented by this peak has reversed. Thus, the phase angle, which is explicitly present in Equation II.13 provides a means of estimating molecular orientation.

Interferences also affect the intensity and apparent location of features in a VSFS spectrum. As Figure 2.2 shows, the maximum intensity of the spectra changes from ≈ 9 to ≈ 14 depending on the phase combinations. Looking at the second vibrational mode at 2950 cm^{-1} , its apparent location changes from 2950 to 2960 cm^{-1} just by changing the phase of the broad mode. Note that the amplitude and frequencies of

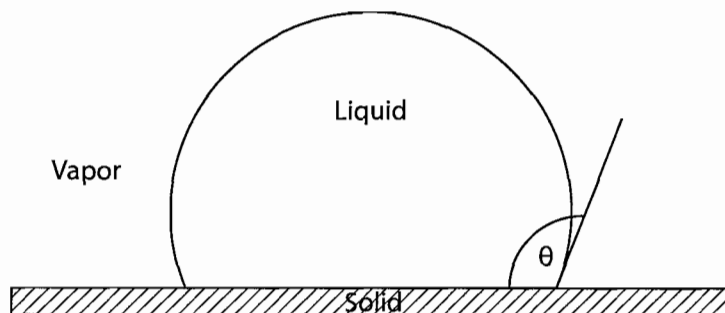


Figure 2.3. Illustration of a water drop on a hydrophobic solid surface with contact angle θ .

the modes themselves remain unchanged in this demonstration. The changes in the spectra are due solely to the phase interactions between the peaks.

Because of these complex interference phenomena, interpreting VSFS results can be quite complex. It is useful to employ strategies to simplify the VSFS spectra and to collect data under an array of solution conditions so that global analysis can be performed. When possible, global analysis of the VSFS spectra within was used to fit whole series of spectra simultaneously, making certain parameters as common to all spectra. Additionally, deuteration of water or CH modes can be used to shift the deuterated mode out of the spectral window. For example, using D_2O instead of H_2O would make the amplitude of the 3200 cm^{-1} peak in Figure 2.2 zero, yielding a spectrum with just the two narrow modes and easing spectral assignment. This technique is used to great effect in chapters IV-VII.

Contact Angle

Contact angle measurements have been used to describe wetting phenomena for

nearly 200 years.[65] In a contact angle experiment, a drop of liquid is placed on a surface and imaged. The angle of the line tangent to the drop and the plane of the surface is the contact angle. In the case of a hydrophobic surface and water, this angle (θ) is greater than 90° . Such a condition is shown in Figure 2.3. The contact angle is indirectly related to the surface composition, but is also greatly affected by surface roughness. Thomas Young, in 1805, introduced a simple equation that describes the equilibrium of forces at the point of contact between a liquid and a solid.[66] This equation is:

$$\gamma_{lv} \cos \theta = \gamma_{sv} - \gamma_{sl} \quad (\text{II.14})$$

where γ denotes the tension, or excess free energy per unit area, of the given interface indicated by the indices l , v and s . These indices correspond to the liquid, vapor and solid phase respectively. Water contact angles are commonly used to characterize the degree of surface hydrophobicity and is roughly related to the surface coverage via the Cassie equation:[67]

$$\cos \theta = n_1 \cos \theta_1 + n_2 \cos \theta_2 \quad (\text{II.15})$$

where n_i is the fractional composition of component i and θ_i is the ideal contact angle of that component. Assuming that one of the components is silica, which has a contact angle of $\approx 30^\circ$, then any contact angle greater than 30° indicates increasing coverage of the surface by the hydrophobic component. It is important to note that advancing contact angles are commonly reported in the literature, but that in this dissertation, only static angles are used. Advancing angles are collected by slowly increasing the

volume of the liquid drop on the surface to determine the maximum contact angle without increasing the surface area. This measurement was not possible on the home-built contact angle system which was used for the majority of this research. Static contact angles tend to be lower than advancing and thus comparisons between the two are only qualitative.

Contact angles are affected by changes in the liquid-vapor interfacial tension as well as by adsorption at surfaces. This feature can be used to quantify interfacial adsorption processes,[68, 69] as is done in Chapter VII. Explanations of this type of analysis are provided there.

Conclusion

This chapter provides background information for vibrational sum-frequency spectroscopy (VSFS), which is used throughout this dissertation to examine interfacial molecular structures and interactions at the solid/liquid interface. The interfacial sensitivity of VSFS arises from its second order nature in which only those molecules with a net anisotropic molecular environment and orientation contribute to the overall nonlinear susceptibility, $\chi^{(2)}$. Such an environment is inherently present at the interface between two materials, such as a solid and a liquid. The detected VSFS intensity is proportional to the square of $\chi^{(2)}$ and the intensity of the incident optical pulses. The following chapter deals with the generation of these intense light pulses and the process of correcting the VSFS for variations in these pulses. The coherent

nature of VSFS has also been discussed, which leads to uniquely informative spectra. This is due to interferences between the different resonant contributions as well as the non-resonant background. Spectral fitting is required to analyze the collected data and deconstruct the spectral interferences which lead to complex lineshapes.

The principles of contact angle measurements have also been introduced, which are used to characterize all of the samples produced in this dissertation. Contact angle measurements are provided to estimate the degree of coverage of samples and later used to investigate adsorption processes.

CHAPTER III

EXPERIMENTAL CONSIDERATIONS

In this chapter, the VSFS experiment, sample preparation methods and other analytical methods used are described. First, the components and characteristics of the laser system are detailed. Next, sample cell and mounts are depicted. Following this, the technique used to calibrate and normalize the VSFS spectra are discussed. In the next section, the methods for preparing samples are described. The final two sections describe the contact angle and atomic force microscopy experiments used to characterize the prepared samples.

Vibrational Sum-Frequency Spectrometer System

Nanosecond Laser System

VSFS experiments were performed using a custom built IR generation system, shown in Figure 3.1. The master oscillator is a Spectra-Physics Lab 110 Nd:YAG laser operating at a 10 Hz repetition rate with a wavelength of 1064 nm. Each pulse is 6.5 ns long with an energy of 600 mJ. The output of this laser is split into two beams of 200 and 400 mJ. The 200 mJ portion pumps a potassium titanyl phosphate (KTP) frequency doubling crystal and the 400 mJ beam is sent towards the optical

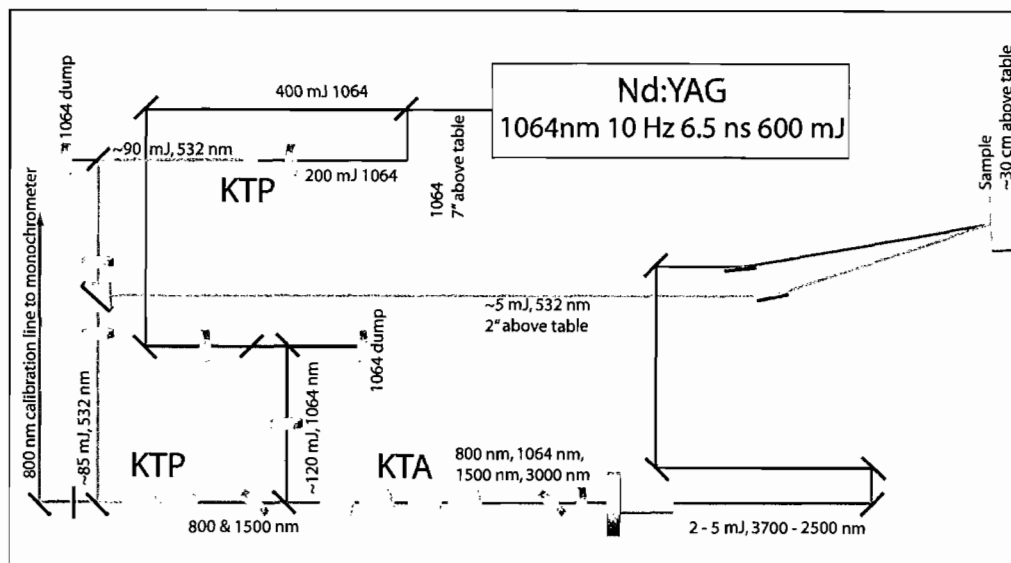


Figure 3.1. Schematic of the nanosecond VSFS laser system, showing the major components and general beam path, used for the hydrophobic surface and SiO_2 experiments.

parametric oscillator (OPO). Approximately 90 mJ of frequency doubled output at 532 nm is generated from the 200 mJ 1064 nm input; the remaining 1064 nm light is dumped using a dichroic mirror. The amount of 532 nm light generated can be adjusted depending on experimental needs. Nominally 85 mJ of this light is sent into the IR generation beamline and the remaining 5 mJ is made available for the VSFS experiments and is polarization selected using a waveplate/polarizer/waveplate assembly. The amount of 532 nm used in these experiments varies depending on experimental conditions.

The 532 nm light sent to the OPO is internally injected into the double pass OPO cavity, which produces relatively narrow bandwidth output (± 0.05 nm) and produces up to 9 mJ of combined 800 nm signal and 1500 nm idler light. The wavelengths of the

signal and idler are changed by angle tuning the crystals. The 1500 nm photons are now the signal and are mixed with ≈ 120 mJ of the 400 mJ of 1064 nm pump in a two stage (four crystal) potassium titanyl arsenate optical parametric amplifier (OPA) to produce the IR light for the VSFS experiments. Angle tuning the OPA crystals maximizes the amount of IR generated. The excess 1064 nm light is dumped using a waveplate and polarizer combination. After filtering out the undesired frequencies, the usable range of the OPA is from 2600 cm^{-1} to 4000 cm^{-1} (2500-3846 nm), with energies ranging from 1 to 4 mJ and pulses having a 2 cm^{-1} bandwidth. This narrow bandwidth is the same as the homogeneous linewidth of C-H stretching vibrations and much less than the typical inhomogeneous Gaussian linewidths of condensed phase CH spectra, which allows high resolution spectroscopy and the identification of small changes in peak locations. The polarization of the IR is adjusted using a quarter waveplate and IR polarizer (II-IV, Inc.). If more IR is needed for the VSFS experiments, more of the 1064 nm pump can be directed to the OPA. The VSFS signal is collected with a photomultiplier tube (PMT) mounted on a variable angle arm and digitized with a boxcar integrator before being sent to a PC running LabVIEW, which records the PMT voltage and controls the IR generator.

In the total internal reflection geometry used in the nanosecond VSFS experiments (shown in Figure 3.2), the VSFS signal is spatially close to the transmitted 532 nm input. To separate the VSFS signal from the 532 nm light, the angle of the detector arm is rotated to the VSFS angle, which is typically $0.2\text{--}0.5^\circ$ from the 532 nm beam.

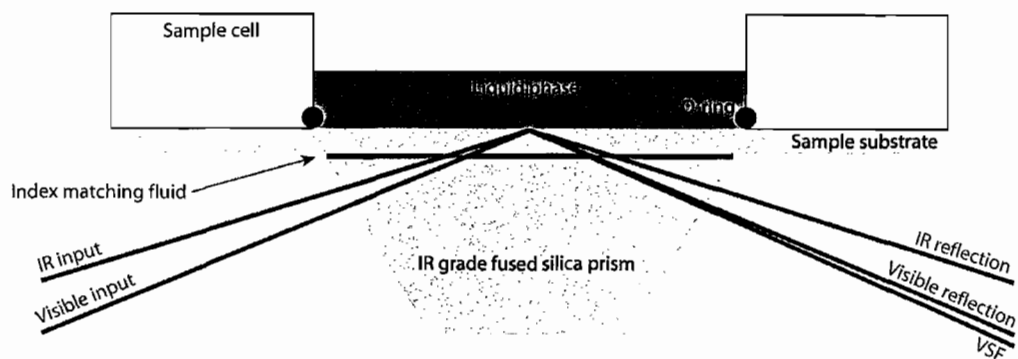


Figure 3.2. Sample setup for a VSFS experiment on a hydrophobic surface. The prism is coupled to the coated sample via a drop of index matching fluid. The laser pulses are overlapped at the interface between the sample and the liquid phase.

This signal is then spatially filtered by two irises and a skimmer. Spectral filtration is done by a blue glass filter, a holographic notch filter coated for 532 nm, a long wave pass filter, a short wave pass filter and a final 532 nm holographic notch filter. These filters block the remaining 532 nm photons and prevent any generated difference frequency or second harmonic photons from entering the PMT. The polarization of the detected VSFS signal is selected by rotating a Glan-Laser polarizer in the PMT detector assembly.

The Interface

Because the interfaces being studied were those of films deposited onto glass substrates, the glass substrates were coupled to an IR grade fused silica prism (ISP Optics) cut at 23° , near the critical angle for 532 nm light at the $\text{SiO}_2/\text{H}_2\text{O}$ interface, as shown in Figure 3.2. The index matching fluid (Cargille, code 43421) nearly matches the refractive index of the visible beam in SiO_2 and allows transmission of

the beams through the prism and into the sample. The sample itself is compression fitted to the prism via a Kalrez o-ring fit into a groove in a teflon or Kel-F sample cell, depending on the sample size, which provides a liquid tight seal on the sample surface. The cells have sufficient volume for both a pH meter and stirrer. Prior to assembling the sample cell, the cell and o-ring are soaked in concentrated H_2SO_4 with NoChromix (Godax Laboratories) overnight, then rinsed copiously in nanopure water and dried in an oven.

The sample cell is mounted on a five axis translation stage which allows the interface to be positioned at the desired height and leveled. One axis of the stage translates the sample horizontally, allowing different locations on the interface to be probed. Because the area sampled in the VSFS experiment is small relative to the area of the sample, the samples have to be investigated at multiple locations to check for heterogeneity.

Calibration and Normalization of Sum-Frequency Spectra

Upon setup or realignment of the IR generation beamline, the IR output is calibrated with a monochromator (McPherson) and liquid nitrogen cooled mercury-cadmium-telluride detector (Source). This is performed by measuring the wavelength of the $\approx 800\text{ nm}$ light produced in the OPO. The cavity end mirror is partially transparent near 800 nm which allows this beam to be picked off and sent to the monochromator. The monochromator is calibrated using the output of a helium neon light at the specular, half, first, 1.5 and second order diffraction peaks. To convert

the measured light into the IR wavenumber, the frequency of the measured light is first calculated using $\nu = c/\lambda$.

$$\nu_{Idler,OPO} = \nu_{Pump,OPO} - \nu_{Signal,OPO} \quad (III.1)$$

Equation III.1 shows the calculation of the OPO idler frequency, in which $\nu_{Pump,OPO}$ is the frequency of the 532 nm pump and $\nu_{Signal,OPO}$ is the frequency of the light measured in the monochrometer.

$$\nu_{Idler,OPO} = \nu_{Signal,OPA} \quad (III.2)$$

$$\nu_{Idler,OPA} = \nu_{Pump,OPA} - \nu_{Idler,OPA} \quad (III.3)$$

In the OPA, the idler from the OPO is now the signal, as shown in Equation III.2. Equation III.3 shows that the frequency of this signal is then subtracted from the frequency of the 1064 nm pump ($\nu_{Pump,OPA}$) to give the frequency of the idler pulse ($\nu_{Idler,OPA}$), which is the IR for the VSFS experiments. This is then converted into the IR wavenumber. There are a total of 42 calibrated positions in the crystal tuning curve, all generated in this way. The calibration is spot checked as needed using the IR spectrum of polystyrene and atmospheric water lines.

As VSFS is a non-linear optical process where the signal intensity is proportional to the intensities of the incoming light ($I_{sf} \propto |\chi^{(2)}|^2 I_{vis} I_{IR}$), it is critical to normalize all spectra for variations in the input energies. Figure 3.3 shows the IR output of the laser system and the transmission spectrum of a prism and plate system through which the IR must travel. The prism causes a nearly 30 percent loss of IR energy at low

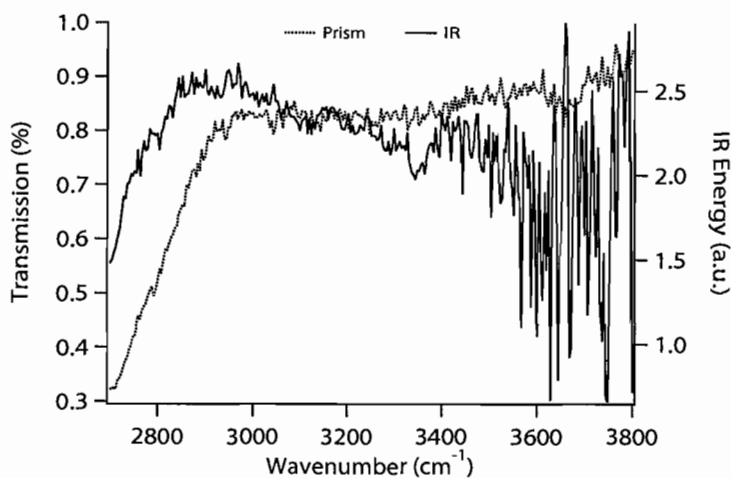


Figure 3.3. The IR output measured in a typical VSFS scan is shown in the black trace and the prism absorption IR spectrum at the interface is plotted with the dotted line on the right axis.

wavenumber, which has a significant effect on the VSFS intensity below 2750 cm^{-1} . It is also clear that the IR output varies with wavelength and is absorbed by atmospheric water above 3550 cm^{-1} . To correct for these effects, all spectra are normalized. IR spectra are collected on a dedicated normalization beamline. In this line, a small portion of the IR beam is picked off prior to the sample cell by reflection off a CaF_2 window and sent to an energy meter; the pathlength and number of optics in this line is identical to that of the main IR line to the sample. The energy meter on the normalization line detects the energy of each pulse and the voltage is integrated and digitized by boxcar, then transmitted to the computer controller. In this way, an IR energy spectrum is collected simultaneously with each VSFS spectrum. Equation III.4 shows the formula used to normalize the collected VSFS spectra.

$$I_{sfg,n} = \frac{I_{sfg}}{I_{vis}I_{IR}\sqrt{\frac{I_{prism}}{I_{IR}}}} \quad (\text{III.4})$$

$I_{sfg,n}$ is the normalized VSFS intensity and I_{sfg} is the intensity of the detected VSFS signal. I_{vis} is the energy of the visible beam, which is collected after the experiments are completed because the green energy varies only slightly from shot to shot. I_{prism} is the IR spectrum of the sample cell, collected with no liquid phase in the cell and is normalized by the incident IR energy. The prism is inside the radical because the VSFS spectra are generated at the midpoint of the prism. Normalization in this way accounts for loss of IR signal due to adsorption of water vapor in the beam path and adsorption/dispersion losses due to the sample.

Coated Sample Preparation and Characterization

Materials

Three different types of hydrophobic coatings deposited on SiO_2 are used in the following chapters. Deviations from the procedures described below will be noted where appropriate. The different molecules deposited are shown in Figure 3.4 and are octadecyltrichlorosilane (ODCS), 1H,1H,2H,2H-perfluorodecyltriethoxysilane (FDES) and Fomblin Z Dol 4000 (Zdol). All silanes were filtered through a $0.1 \mu\text{m}$ Teflon membrane (to remove any large polymerization products) and copper

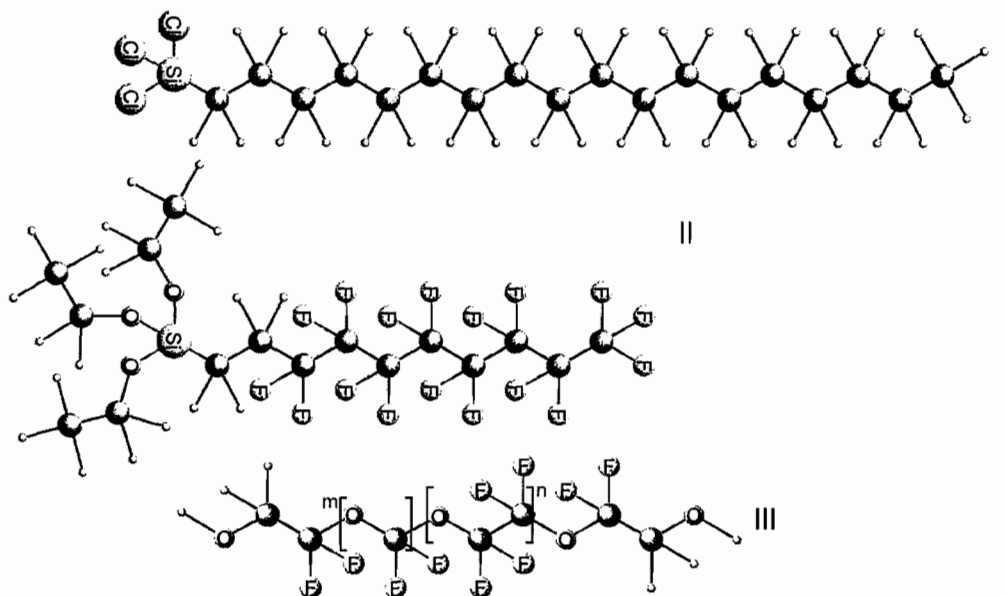


Figure 3.4. Precursor molecules used for coating the glass and silicon wafer substrates: (I) ODCS, (II) FDES and (III) Fomblin Z Dol 4000.

stabilizer. Full characterization of samples deposited via the methods below is undertaken in Chapter IV (ODCS and FDES) and Chapter V (Zdol).

All organic solvents used were HPLC grade or their nearest equivalent and typically came from Aldrich. Concentrated sulfuric acid and 30% H_2O_2 were purchased from UO Science Stores. $\text{Ca}(\text{NO}_3)_2$ for the humidity chamber was purchased from Aldrich and baked out at 225°C for 24 hours prior to use.

Substrate Preparation

The substrates used for the VSFS experiments were low bubble, 0.0625 in. thick GE-124 type fused silica, obtained from Quartz Scientific Products or Behm Quartz. This grade of fused silica is significantly less expensive than synthetic optical grade

silica, while having similar IR transmission characteristics due to its being fused electrically. Some silane samples were also prepared on Si/SiO₂ wafers for AFM analysis and were found to have nearly identical structure and composition compared to their glass counterparts; this is expected since silanes only bond to a small percentage of the surface hydroxyls.[27, 28] All substrates were rinsed and wiped with chloroform, acetone and methanol to remove visible organic residues. Following this, substrates were ultrasonically cleaned for 10 minutes in each of three solvents: chloroform, acetone and methanol. The substrates were then rinsed under flowing nanopure water for 10 minutes before being dried in a clean oven for 15 to 30 minutes. Substrates were then immersed in 7:3 (vol:vol) piranha solution (concentrated H₂SO₄ and 30% H₂O₂) for one hour. Finally, the substrates were rinsed under flowing nanopure water for 20 minutes and dried at 110°C until dry and ready for deposition.

Octadecylsilane Deposition

Octadecylsilane (ODS) monolayers have been deposited in closed and silanized glass staining jars, one at a time. Dry substrates were placed in a 64% relative humidity chamber for 30 minutes prior to deposition to build up a layer of water on the substrate. Chemical analysis by TOF-SIMS and XPS found the substrates to be free of significant organic chemical contamination before and after this step. The constant humidity of the chamber was maintained by filling the bottom of the chamber with a saturated solution of Ca(NO₃)₂. [70] The depositions were performed by making a 1 mM solution of ODCS in a 4:1 (vol:vol) mixture of hexadecane and

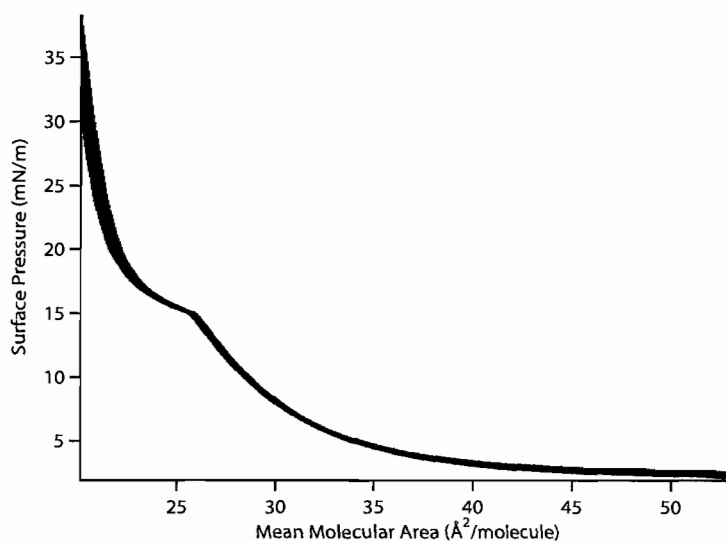


Figure 3.5. Surface pressure isotherm of FDES on pH 2 HCl after equilibration. The figure shows an average isotherm with associated standard deviations.

carbon tetrachloride. The ODCS was first filtered through a $0.1 \mu\text{m}$ Teflon membrane to remove any large polymerization products. The required amount of ODCS was then injected into the deposition solvent via a calibrated Eppendorf pipette. The deposition solution was then sonicated for 10 seconds to mix the ODCS, after which the substrate was inserted into the reaction vessel. After a 6 hour incubation, the ODS coated sample was removed and rinsed thoroughly with hexadecane, chloroform, acetone, methanol, acetone and chloroform. Each sample was then sonicated for 1 minute in CHCl_3 and then rinsed with acetone and methanol. Finally, the samples were blown dry with argon and baked at 110°C for 1 hour and stored under vacuum until used.

1H,1H,2H,2H-perfluorodecylsilane Deposition

Monolayers of 1H,1H,2H,2H-perfluorodecylsilane (FDS) were primarily prepared

by Langmuir-Blodgett (LB) deposition with FDES. The surface pressure isotherm of FDES is shown in Figure 3.5. The plateau corresponds to the transition between isolated gas phase molecules and a condensed solid phase. Ohnishi et al. found a similar isotherm for the same molecule.[71] To prepare samples using the LB technique, a KSV Minitrough was cleaned with chloroform, ethanol and water and its cleanliness verified by measuring the surface tension of water (72.4 ± 0.2 mN/m). After cleaning, the trough was filled with 0.1 M HCl to catalyze the cleavage of the ethoxy groups on the FDES molecule. After immersing the substrate in the dipping well, a 1 – 3 μ M solution of precursors in CHCl_3 , the exact concentration determined by mass, was spread on the surface of the liquid layer to a starting density of 1 molecule per 45\AA^2 . These surface layers were then equilibrated for 30 minutes and compressed to the deposition pressure, typically 15 mN/m, at a rate of 5 mN/m/min before withdrawing the substrate at 5 mm/min. The FDS coated substrates were then baked at 110°C for 1 hour and stored in a vacuum desiccator cabinet until used.

Z Dol 4000 Deposition

The Zdol used for this thesis is a 4000 Dalton molecular weight polymer made primarily of fluoromethoxy (m in Figure 3.4) and fluoroethoxy (n in Figure 3.4) repeat units where $m/n \approx 1$. Samples were prepared by immersing a glass substrate in a teflon chamber filled with 0.2% by volume solution of Zdol in perfluorohexanes. After a 10 minutes incubation, the glass substrates were withdrawn from the vessel at a constant speed of 2.1 mm/min. The Zdol was bonded to the substrate by heating the

samples in an oven at a temperature of 150°C for 30 minutes. This method has been shown to produce highly uniform Zdol coatings with thicknesses of 2.3 nm.[72] The Zdol coated samples were stored in vacuum until used.

Contact Angle Measurements

Contact angle measurements were performed via the static sessile drop method.[73, 74] This involves lowering a small drop of solution, typically with a 5 to 15 μL volume onto a solid surface. When the drop touches the solid surface, it leaves the dispensing needle and settles onto the surface. After a brief equilibration period of 30 to 60 seconds, an image of the drop is captured and its shape analyzed using computer software to calculate the contact angle. Contact angle measurement in Chapters 4, 5 and 6 were performed on a home built instrument consisting of an Olympus digital camera focused to infinity through a two lens microscope which captures an image of the contacting solution drop. Images were captured at a resolution of 1024×768 pixels in greyscale mode. The system was calibrated by recording the image of a ruler, which established the number of pixels per mm. This information was input into the LB-ADSA plugin for ImageJ that is fully described in the literature[75] to generate a contact angle.

Experiments in Chapter VII used a KSV Theta optical tensiometer operating using the same methods. Contact angles on this instrument were then determined using the

included software package. Deviations in measured contact angles between the two instruments is less than 1° , which is approximately the accuracy of the measurements.

For large samples, such as those deposited out of the liquid phase, nominally 10 distinct drop measurements were made so as to sample the entire surface. For LB deposited samples and small substrate samples where the covered area is small ($\approx 1 - 4 \text{ cm}^2$), a minimum of five drops were imaged. The sample surfaces were blown off with argon as needed to make room for a new contacting drop.

Prior to each contact angle experiment, the syringe and needle used to deliver the solution were cleaned in concentrated H_2SO_4 with NoChromix and rinsed copiously with water and dried in an oven.

Atomic Force Microscopy

All AFM results shown were collected on a Digital Instruments Nanoscope IIIa in intermittent contact mode with Nanosensors PPP-NCST or PPP-NCH tips. To ensure trueness of results, the instrument parameters were adjusted so that the forward and reverse scans overlapped and the tip was not clipping on any objects on the surface. AFM analysis was performed on a desktop PC running Gwyddion 2.12. Collected data was corrected for tilt and bowing of the piezoelectric actuators as needed using the minimum amount of correction necessary; typically not more than leveling the data with a 2^{nd} order polynomial in one direction.

AFM samples were prepared by either custom depositing films on $\approx 1 \text{ cm}^2$

substrates or by taking samples made on large substrates and cutting them down to size on a lint free cloth. Cut samples were blown off with argon and gently wiped with methanol immediately after cleaving to remove detritus from the scribing procedure. Samples were carefully blown off with dusting gas as needed in the instrument room. Because of the small allowable size of samples in the AFM, it was not possible to collect VSFS data on samples analyzed via AFM.

Conclusion

This chapter presents the details of the laser system used to perform the VSFS experiments in Chapters IV-VII. The system generates narrow bandwidth pulses that allow high resolution spectroscopy of the CH and OH stretching regions. Water vapor absorption affects the IR transmitted to the interface, as does absorption by the SiO₂ prism and plate. This causes the VSFS spectra to require normalization when looking at features at high or low wavenumber. This normalization method has been described. This chapter has also presented the general synthetic methods used for making the hydrophobically coated samples studied within and the methods of characterizing them.

CHAPTER IV

INVESTIGATIONS OF MONOLAYER PREPARATION METHODS WITH
VIBRATIONAL SUM-FREQUENCY SPECTROSCOPY

Hydrocarbon and fluorocarbon self-assembled monolayers on fused silica have been prepared using several different methods to evaluate the sensitivity of VSFS to differences in monolayer structure and determine the best methods for producing samples. The studies in this chapter show that differences readily seen by AFM and contact angle measurements do not necessarily show up in sum-frequency spectra for monolayer samples in air, which is the most common way ODS monolayers are characterized in VSFS. However, when immersed in water, there is a clear difference in the behavior of the films that are nearly ideal and those that are covered in polymer aggregates. For fluorocarbon samples, there are no apparent differences in the behavior of the monolayers in water. However, only the small CH portion of the monolayer chain can be probed in the VSFS experiment. The interfacial water structure, which shows significant differences between high and low quality ODS samples is not sensitive to the differences in the fluorocarbon samples. Significant differences in the interfacial water structure are observed for fluorocarbon and hydrocarbon monolayers that indicate that the interfacial charge is greater at the fluorocarbon surfaces. The first spectroscopic evidence that direct interactions

between fluorocarbons and water are weaker than hydrocarbons and water is also obtained.

Introduction

Hydrocarbon and fluorocarbon self-assembled monolayers (SAMs) have been the subject of much fundamental and applied research, particularly as coatings to alter the biological[76–79] and tribological[80–84] properties of solid surfaces. There are several types of self assembling molecular systems; some of the most common are alkylsilanes, which form strong chemical bonds with SiO_2 surfaces and crosslink with each other to form a durable organic coating. The most heavily studied of these coatings is octadecylsilane (ODS), which is commonly deposited on SiO_2 surfaces using the methods pioneered by Sagiv.[36] However, the preparation of a smooth, uniform surface from alkylsilanes is a non-trivial task. It is well known that the structure ODS monolayers are sensitive to a variety of parameters. Humidity[85] and temperature[26, 85] can have significant effects on the monolayer formation, causing variations in chain order and the deposition of silane aggregates. Deposition solvent has been shown to affect surface coverage[40, 86] and even the age of the ODS precursors[87] has been noted as causing variations in monolayer properties. Given all of these sensitivities, it is not surprising that multiple SAM configurations can be obtained from the same procedure and that methods for SAM preparation vary widely.

An increasingly used technique for characterizing SAM surfaces is VSFS, because of its inherent surface sensitivity to molecular structure and conformation as well as its ability to access buried interfaces. VSFS has been used to investigate the structure[43, 88] and growth of ODS monolayers.[32] It has also been used to study pH driven behavior of water at ODS[89] and aminopropylsilane[90] surfaces, as well as several different adsorption processes.[34, 91–93] In many of these VSFS studies, the assumption is made that the prepared surfaces are smooth and defect free. This is a critical assumption since changes in SAM topography may alter the orientation of adsorbing species and gaps in coverage will surely affect the electrostatics of the interface, as SiO_2 is known to be charged surface in aqueous environments.[94] Because of the sensitivity of the silanization process to the deposition environment, it is unlikely that this assumption is true. In fact, a study by Ye et al. noted significant differences in the VSFS spectra of SAMs formed under “identical” conditions.[89]

In this chapter, the sensitivity of VSFS to differences in fully formed SAM coatings of ODS and 1H,1H,2H,2H-perfluorodecylsilane (FDS) is investigated. Monolayer coverage and quality are first analyzed using contact angle goniometry and atomic force microscopy. The results within show that when the surface is fully covered with ODS or FDS, VSFS is insensitive to the presence of alkylsilane aggregates, as indicated by changes in CH stretching vibrations.

Experimental

Monolayer Preparation

For the analysis of the effect of monolayer quality on VSFS spectra, five types of monolayer depositions were undertaken. Each deposition was performed five times to make five identical samples. Water contact angles of all of the samples were measured to ensure homogeneity of the methodology. One sample from each of these lots was selected for AFM analysis.

Two types of hydrocarbon monolayer (ODS) sample preparations were used. The first is the previously described solution phase deposition from dry solvents in Chapter III. The second is using water saturated solvents. Water saturated hexadecane and CCl_4 were prepared by injecting 1 mL of nanopure water into flasks containing each solvent. The flasks were then shaken and equilibrated overnight. The saturated solvents were then decanted from the water layer at the bottom of the flask. Water saturation has been found to increase the speed of the silanization reaction and yield monolayers of equal hydrophobicity and spectroscopic character compared to monolayers formed in dry solvents.[32]

Fluorocarbon monolayers (FDS) were deposited via the LB method at both 12 and 17 mN/m as described in Chapter III. FDS samples were also prepared from the trichlorosilane form of the precursor, referred to hereafter as FDCS. This was done by soaking the substrates in a 2.3 mM solution of fluorinated chlorosilane in heptane for

20 minutes. The silanes were delivered to the solution using a calibrated Eppendorf pipette. A FDS samples were also made on silicon wafers for AFM measurements to compare the differences between the films deposited at both pressures and the liquid phase sample.

For the water studies, the solutions used were unbuffered pH 2 HCl, pH 10 NaOH and H₂O. The solution pHs were measured using a three point calibrated pH meter. Deuterated studies were carried out in unbuffered pD 2 DCl, pD 10 NaOD and D₂O. The pDs were measured using pH indicator paper. Acid and base solutions were made from reagent grade concentrated HCl and NaOH pellets purchased from Fisher. D₂O was purchased from Cambridge Isotopes and DCl and NaOD solutions were from CDN Isotopes.

Sum-Frequency Generation

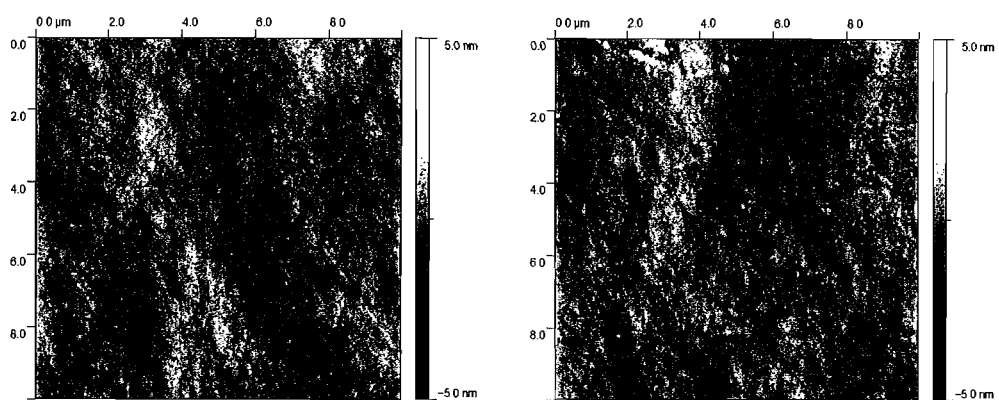
VSFS experiments were performed as described in Chapter III. Samples were compression fitted onto a Kel-F sample cell with a Kalrez o-ring. IR and visible beams were directed at the sample through a 23.1°, triangular IR grade fused silica prism with a 1 in² top surface (ISP Optics). Beam angles relative to the optical bench surface were 17° and 23.1° for the IR and 532 nm, respectively. Samples were mated to the prism via a drop of microscope immersion oil (Cargille, custom code 43421). Data (20 shots per point) were collected at 2 cm⁻¹ resolution in the air and D₂O studies from 2800–3000 cm⁻¹ and every 5 cm⁻¹ from 2800–3800 cm⁻¹ in the H₂O studies. Each spectrum shown is an average of three spectra. Raw VSFS data were

background corrected for scatter and then normalized for variations in IR intensity and adsorption by the SiO₂ prism and plate. All spectra shown here are in the SSP polarization scheme unless otherwise noted, which probes components of the transition dipole moment normal to the interfacial plane.

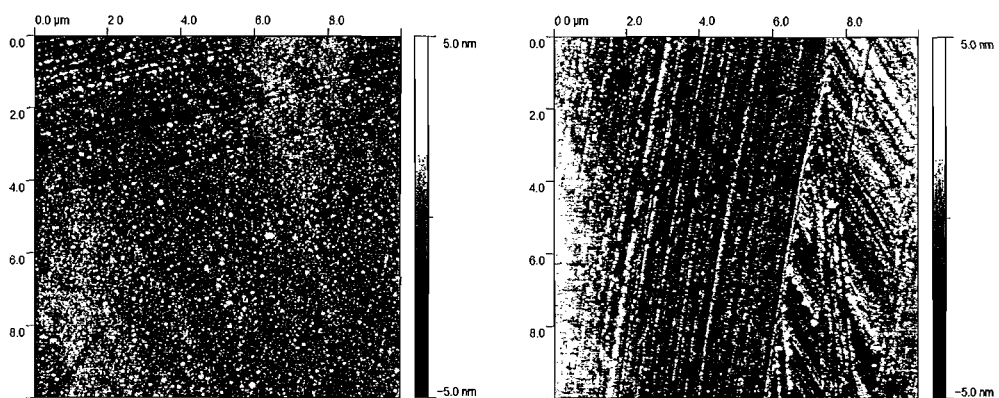
Results and Discussion

Hydrocarbon SAMs

To explore the sensitivity of VSFS to the quality of various SAM films, a series of ODS and FDS films were prepared using different methods. Representative AFM images of a SiO₂ substrate and a uniform monolayer of ODS are shown in Figure 4.1(a) and Figure 4.1(b) respectively. The two images are nearly indistinguishable. Previous AFM studies have measured a decrease in the RMS roughness of an ODS coated glass slide relative to an uncoated blank.[95] This ODS sample replicates the low amplitude texture of the clean glass substrate, except for a few features that are attributed to solution polymerized ODS that has deposited on the surface. The AFM data in combination with aqueous contact angle measurements is used to assess the quality of the sample surfaces. ODS monolayers from this batch, hereafter referred to as high quality ODS samples (HQODS), have static contact angles from 110° to 112° with average deviations of $\pm 1^\circ$. Previous static contact angle measurements of ODS layers on glass agree well with these results, suggesting that the surface is purely methylated.[30, 34]

(a) SiO_2

(b) HQODS



(c) LQODS

(d) LQODS after wiping

Figure 4.1. Tapping mode AFM images of a: (a) bare glass substrate, (b) “high quality” ODS monolayer, (c) “low quality” ODS monolayer before wiping and (d) “low quality” ODS monolayer after wiping.

In this laboratory, the ideal monolayer (HQODS) can only be formed within a narrow range of conditions and each sample comes from a fresh solution. The most common problem encountered is polymerized aggregates of ODS on the surface, as observed by AFM. A representative AFM image of this type of sample is shown in Figure 4.1(c). Compared to the high quality sample in Figure 4.1(b), there are clear differences. Much of the ODS coating in Figure 4.1(c) appears similar to the underlying glass texture, except for a high density of polymerized ODS aggregates on the surface. These aggregates are relatively unaffected by sonication in an array of solvents and remain on the sample after wiping. The results of wiping such a sample is shown in Figure 4.1(d). Wiping ODS surfaces after deposition has been reported to improve their orientation;^[87, 96] however, the aggregates appear not to be removed from the sample only smeared over it.

Deposition of ODS aggregates was found to be a significant problem when using ODS precursors from a vial that had been in use for more than two weeks, despite storing them in a desiccator. Trichlorosilanes react with water introduced into the vial when it is open to the atmosphere, resulting in formation of alkylsilanols. These alkylsilanols then condense with each other to make aggregates.^[35] Aggregate deposition was also a problem when the reaction was performed with solvents that were not freshly opened. In this case, the reaction solutions became cloudy due to ODS polymerization more quickly than when the reaction was performed with fresh solvents. To replicate the effect of using old solvents or ODS precursors, a

batch of samples was prepared in the same way as the HQODS batch, but reacted in water saturated solvents. Samples from this batch are referred to as low quality ODS monolayers (LQODS). Representative AFM images of an LQODS sample are shown in Figure 4.1(c) and Figure 4.1(d). These LQODS samples have water contact angles of $105 \pm 3^\circ$ to $108 \pm 3^\circ$. This lower contact angle may be due to a number of factors including more exposed SiO_2 , increased surface roughness or CH_2 groups from silane aggregates. Because the conditions used to make LQODS have been reported as producing highly covered SAMs, it is unlikely that there is a significant SiO_2 that is accessible to water. Contact angle measurements can be significantly affected by surface roughness, with rougher surfaces having greater hysteresis between advancing and receding contact angles; [30] greater hysteresis will result in a lower static contact angle. Fully CH_2 terminated surface have an ideal contact angle of 94° , which is lower than that of a purely methylated surface (112°). [30] LQODS samples are rougher than HQODS and have aggregates which are primarily solvent accessible methylene groups; both of these effects are likely reasons for the lower contact angle of LQODS.

To gain an idea of how sensitive the VSFS measurements are to the obvious differences in monolayer quality as measured by AFM (Figure 4.1(b) and Figure 4.1(c)) and contact angle, spectra of the alkyl chains of the monolayer/air interfaces were collected and are shown in Figure 4.2. For the HQODS samples (\square), two narrow peaks at $2874 \pm 1\text{cm}^{-1}$ and 2934 ± 1 from the $\text{CH}_3(\text{ss})$ Fermi resonance pair are prominent. Smaller contributions at $2912 \pm 1\text{cm}^{-1}$ and $2960 \pm 1\text{cm}^{-1}$ are due to

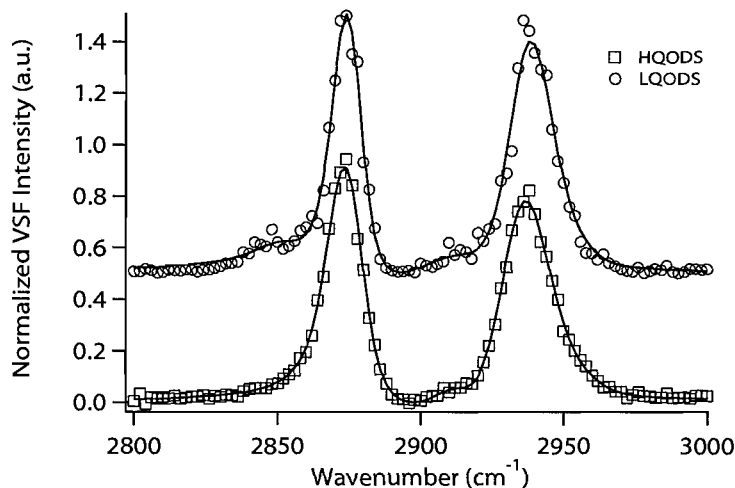
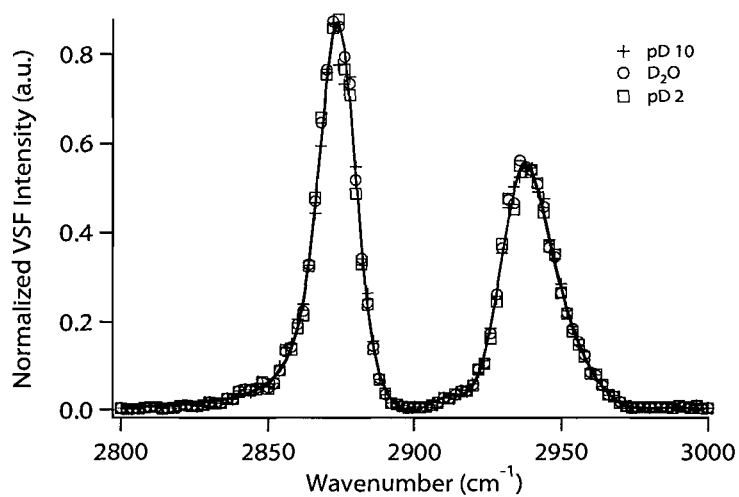


Figure 4.2. SSP polarized VSFS spectra of HQODS and LQODS monolayers in air, offset for clarity. The solid lines are fits to the data.

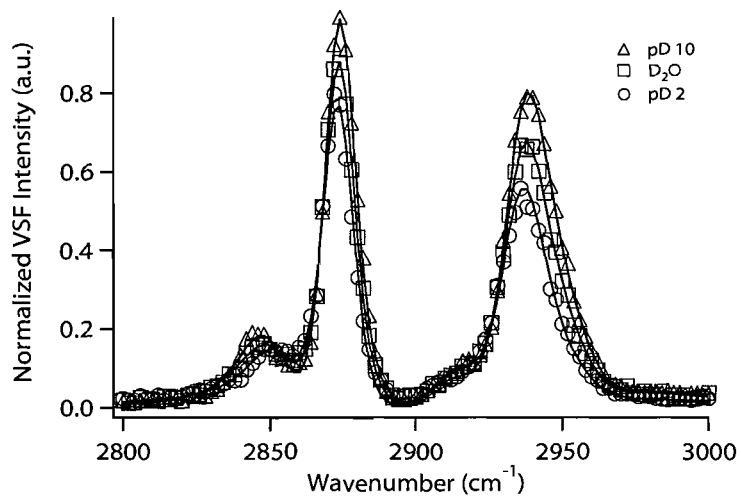
the $\text{CH}_2(\text{as})$ and $\text{CH}_3(\text{as})$ vibrational modes, respectively. These results are in good agreement with previous VSFS studies of well-ordered monolayers[32, 89, 92] where it has been concluded that the chains are in an all-trans configuration, free of gauche defects. There are very minor differences between the HQODS and LQODS spectrum where surface aggregates are present. All of the modes in the HQODS spectrum are present in the LQODS sample spectrum (\circ) with an additional small shoulder at $2852 \pm 2\text{cm}^{-1}$ originating from symmetric stretching vibrations of methylene groups in the chains of the monolayer or surface aggregates. These modes are known to appear when chain order decreases.[32, 89] Liu et al. found that at long reaction times the $\text{CH}_2(\text{ss})$ due to gauche defects disappears as the monolayer becomes more ordered, but does not make note of disordered surface aggregate deposition.[32] The LQODS/air VSFS spectra shown here are insensitive to the location sampled and

are relatively consistent from sample to sample, with only minor changes in relative intensities of the $\text{CH}_2(\text{ss})$ and $\text{CH}_3(\text{as})$ peaks. In general, VSFS spectra from both samples show similar features, despite the significant differences in the topography and water contact angle.

To understand how water might affect these spectra, the samples were immersed in water (D_2O) and the VSFS response was measured. D_2O was used to minimize spectral interference from OH stretching modes. Measurements were made at three pD values and the ratios of spectral peak amplitudes derived from spectral fitting data are shown in Figure 4.4. From a visual comparison of HQODS in Figure 4.2 and Figure 4.3(a), it does not appear that the structure of HQODS changes significantly with exposure to water or changes in pD. As can be seen in Figure 4.3(a), the monolayer spectra at high, low and neutral pD values are nearly identical. Spectral fitting finds all three of these spectra are dominated by the $\text{CH}_3(\text{ss})$ -FR pair at 2874 ± 1 and $2934 \pm 1 \text{ cm}^{-1}$, with small contributions from the $\text{CH}_3(\text{as})$ at 2960 cm^{-1} and $\text{CH}_2(\text{as})$ at 2912 cm^{-1} . Analysis of the spectral fitting reveals some differences between the HQODS samples in air and in D_2O . The amplitude ratio of the $\text{CH}_3(\text{ss})$ - 2874 cm^{-1} to the $\text{CH}_3(\text{as})$ mode is shown in the (■) trace in Figure 4.4. Immersing the sample in water slightly decreases this ratio, indicating a change in the molecular orientation of the monolayer; however, this change is unaffected by pD. Increasing the tilt of the methyl group from the surface normal increases the $\text{CH}_3(\text{as})$ intensity in the SSP polarization scheme used here, which reduces the amplitude ratios in Figure 4.4.



(a) HQODS



(b) LQODS

Figure 4.3. VSFS spectra of (a)HQODS monolayer/ D_2O and (b)LQODS monolayer/ D_2O interface at pD 10, D_2O and pD 2 in the SSP polarization scheme. The solid lines are fits to the data.

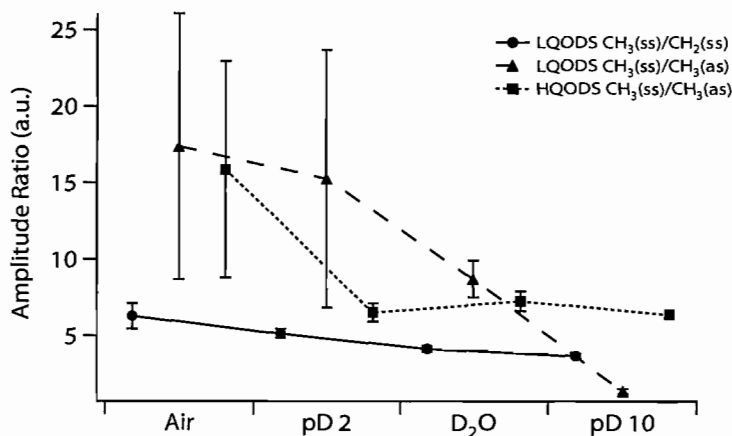


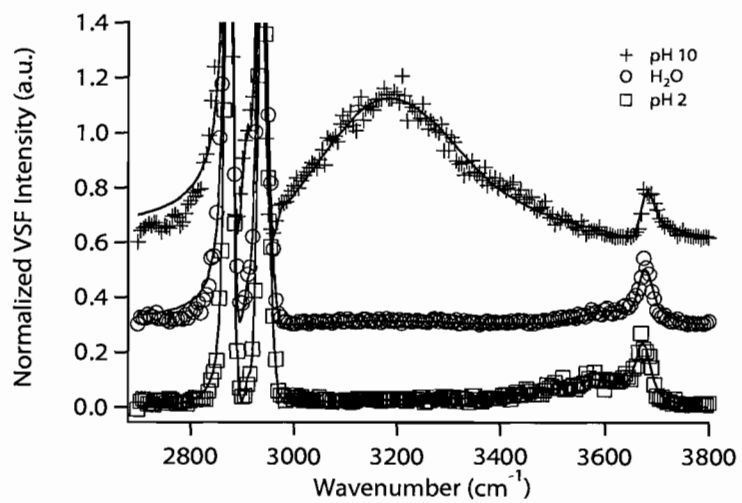
Figure 4.4. SSP amplitude ratios of $\text{CH}_3(\text{ss})$ - 2874 cm^{-1} to the $\text{CH}_2(\text{ss})$ and $\text{CH}_3(\text{as})$ peaks for HQODS and LQODS. HQODS ratios with $\text{CH}_2(\text{ss})$ are not shown because this peak was not required for spectral analysis.

Despite changes in the methyl group orientation, introduction of D_2O does not appear to cause gauche defects in the HQODS sample, as there are no features in the spectra attributable to $\text{CH}_2(\text{ss})$; thus this ratio is not shown in Figure 4.4. The HQODS samples remain well-ordered in water, with chains in an all-*trans* configuration. This finding concurs with that of a recent molecular dynamics study that found water is able to only slightly perturb the structure of well-ordered ODS SAMs.[97]

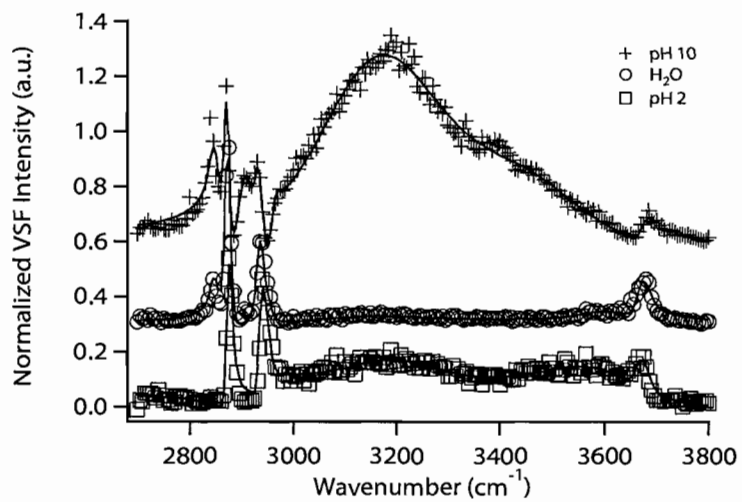
Unlike HQODS, there are apparent differences between the VSFS spectra of LQODS in air and in D_2O . In D_2O , the $\text{CH}_2(\text{ss})$ at 2852 cm^{-1} appears more distinct than in air. As the pD is increased, the overall intensity of the spectra increase and the peak near 2930 cm^{-1} seems to shift as its amplitude increases. These changes are primarily due to increases in the amplitude of the CH_2 resonance at 2852 cm^{-1} and the $\text{CH}_3(\text{as})$ at 2960 cm^{-1} . Analysis of the ratio of $\text{CH}_3(\text{ss})$ - 2874 cm^{-1} amplitude to the $\text{CH}_3(\text{as})$ amplitude, shown in the (\blacktriangle) trace in Figure 4.4, shows that the

amount of $\text{CH}_3(\text{as})$ increases greatly with increasing pD. The (●) trace in Figure 4.4 shows that the ratio of $\text{CH}_3(\text{ss})$ - 2874 cm^{-1} to $\text{CH}_2(\text{ss})$ decreases when the LQODS sample is exposed to water. Taken together, it is apparent that the presence of water significantly alters the organization of the LQODS samples, changing the orientation of the methyl headgroups and the methylene groups in the alkyl chains. Assuming a dense, uniform ODS monolayer, the decrease in the $\text{CH}_3(\text{ss})/\text{CH}_2(\text{ss})$ ratio can be attributed to increasing the number of gauche defects in the monolayer chains. However, LQODS samples are highly aggregate covered, so the degree to which these small changes are due to polymerized ODS versus ODS bound to the substrate in the monolayer itself is uncertain.

To understand the role of water in the changes at the ODS surface, VSFS measurements of water structure have been made. Figure 4.5 shows monolayer/water spectra of a HQODS sample (Figure 4.5(a)) and of a LQODS sample (Figure 4.5(b)). Spectra are shown at three pH values, corresponding to the pD values in the D_2O experiments. The large, narrow features in the traces of Figure 4.5(a) are from the previously discussed $\text{CH}_3(\text{ss})$ -FR pair at 2874 cm^{-1} and 2934 cm^{-1} , with small contributions at 2912 cm^{-1} and 2960 cm^{-1} due to the $\text{CH}_2(\text{as})$ and $\text{CH}_3(\text{as})$, respectively. The CH stretching features do not change with pH, confirming the D_2O analysis. Extending from ≈ 3000 – 3800 cm^{-1} is the water region of these HQODS pH spectra, which contains signals from transition dipole moments of water molecules having some projection normal to the interfacial plane. At pH 10, the water region is



(a) HQODS



(b) LQODS

Figure 4.5. SSP spectra of (a) HQODS/water with CH₃ peaks truncated and (b) LQODS/water interfaces at high, intermediate and low pH values. The solid lines through the data are the spectral fits. The spectra are offset for clarity.

dominated by a broad feature corresponding to water molecules in a range of hydrogen bonding environments. Based on spectral fitting, this broad feature can be described by two bands near 3200 cm^{-1} and 3400 cm^{-1} . A narrow peak at $3672 \pm 2\text{ cm}^{-1}$ due to uncoupled OH oscillators (free-OH mode) pointing into the hydrocarbon monolayer has been seen at ODS and other water/hydrophobe interfaces.[43, 89, 98–100] The free-OH mode maintains a constant amplitude and position across the pH range examined; this is expected since there are no changes in the HQODS sample structure with changing pD. At neutral pH, shown by the (o) trace in Figure 4.5(a), the coordinated water region near 3200 cm^{-1} is flat, indicating that there is little net orientation of water molecules normal to the interface. An additional peak grows in as the pH is decreased: a shoulder on the right side of the free-OH at $3618 \pm 5\text{ cm}^{-1}$ with a width of $81 \pm 7\text{ cm}^{-1}$. At pH2, the coordinated water signal remains low, but spectral fitting reveals that its phase has reversed, which indicates a reversal in the orientation of the interfacial water molecules and thus the interfacial charge. This pH behavior is quite similar to that seen in second harmonic and VSFS studies of ODS monolayers[89, 101] and SiO_2 . [102]

Several sources are possible for the peak at 3618 cm^{-1} : silanols, $\text{SiOH}\cdots\text{H}_2\text{O}$ hydrogen bonds and intra-chain water molecules. This mode cannot be isolated silanols for two reasons. First, isolated silanols are located near 3688 cm^{-1} according to a study of silica gel in CCl_4 , a 60 cm^{-1} difference.[103] Furthermore, if this mode were due to bare silanols, it would not be able to reverse orientation with a change

interfacial potential. The same study identified silanol-water hydrogen bonds as having energies near 3520 cm^{-1} , [103] which would be included in the coordinated water envelope. Because this peak changes phase with the reversal of the surface potential, as well as its unique location, it can be concluded that this resonance arises from water molecules in the hydrocarbon chains. Water molecules solvated in CCl_4 have previously been identified in the same location by IR [104] and VSFS [105] studies and have been found to partially penetrate into ODS SAMs. [97] Further support for this assignment comes from the alteration of ODS monolayer orientation when it is exposed to water, as seen in the D_2O analysis. Tian and Shen have observed a similar peak at the ODS/water interface and proposed that it is due to the incorporation of ions that disrupt the hydrogen bonding of the topmost layer of interfacial water molecules; [98] this may also contribute to the signal, but these two possible contributions cannot be distinguished by this analysis.

VSFS spectra of LQODS are shown in Figure 4.5(b). The CH stretching region from $2800\text{--}3000\text{ cm}^{-1}$ appears dramatically different in these spectra compared to the CH spectra of LQODS shown in Figure 4.3(b), but these differences are due to interferences with OH stretching modes and are well fit with parameters similar to those used to fit the D_2O results. Major differences between the spectra of LQODS and HQODS occur in the coordinated water region around $3200\text{--}3400\text{ cm}^{-1}$. At high pH, shown in the (+) trace of Figure 4.5(b), the water signal in the $3000\text{--}3600\text{ cm}^{-1}$ region is largely due to the electrostatic orientation of water by the

negatively charged SiO_2 substrate. Decreasing the pH to neutral, seen in the (o) trace, reduces the coordinated water signal greatly and reveals the CH stretching modes more clearly. At pH 2, the signal from coordinated water molecules increases and reverses phase, indicating a charge reversal of the interface. The signal from coordinated water molecules at the LQODS interface is larger relative to the CH stretching modes than at the HQODS interface at the pHs examined, indicating that electrostatic field at the LQODS/ H_2O interface is larger.

The pH behavior of both ODS samples is most readily explained by the surface charging characteristics of SiO_2 . At high pH, bare SiO_2 is negatively charged. As the pH decreases, so does the surface charge, down to pH 2, which is the isoelectric point of SiO_2 . [102] Decreasing this charge decreases the interfacial electric field and thus the number of water molecules with dipole components oriented normal to the interface and the associated VSFS signal. LQODS samples have a greater VSFS signal at high pH than HQODS; the integrated area of the coordinated water peaks in LQODS is 25% greater than in HQODS and the maximum VSFS intensity is 10% larger. This greater signal means that either the water molecules are more well-ordered at LQODS or there are more ordered water molecules. Given the AFM results which show that LQODS is covered in aggregates and the greater disruption of LQODS monolayer structure by water, it is unlikely that water molecules are more ordered at LQODS than HQODS. This means there are more water molecules ordered at this interface. The source of the larger number of ordered molecules is a greater interfacial

charge from SiO_2 . LQODS, because of the rapid rate of formation may have a larger number of surface defects that are formed by poor packing of the large aggregates that form in the deposition process. This kind of poor packing has been shown to affect surface topography and may increase access to the surface.[35] These monolayer defects result in more surface SiO_2 groups being accessible to water that can donate or accept a proton, which results in a higher surface charge at a given pH and larger interfacial electrostatic field to orient the water molecules. The apparent reversal of surface charge at low pH is not consistent with SiO_2 measurements, which have found the surface does not reverse charge before pH 2.[33, 102, 106] Reducing the number of silanol groups on the substrate has been used to account for the shifting of the isoelectric point of ODS coated surfaces to a higher pH.[33] The apparent charge reversal may also be due to water molecules directly interacting with the SiO_2 surface, as suggested by Ye et al.[89] The exact source of water orientation, for well-formed monolayers will be addressed in the next chapter.

These results show that differences in monolayer quality are not readily observable by VSFS in air, but are in water. Immersion of ODS SAMs in water alters the orientation of the alkyl chains slightly, however these changes are different for high and low quality surfaces. When an ODS SAM is well-formed, changes in pH have very little effect on the structure of the alkyl chains and less water penetrates to the substrate. However, for poorly structured films the orientation of the alkyl chains changes with bulk pH because more water penetrates through the SAM to the substrate.

Fluorocarbon SAMs

Fluorocarbon monolayers, FDS samples, were examined in a similar manner to ODS, characterizing the samples with AFM and contact angle measurements prior to VSFS experiments. Because of the high reactivity of the FDCS precursors, both solution phase and LB deposition techniques were studied. FDS deposited from trichlorosilanes in solution significantly coats a substrate from as little as 2 minutes up to 10 minutes. However, the results of such depositions were highly variable. Careful control of the coating parameters, using newly opened FDCS precursors and heptane freshly dried through an activated alumina column led to fairly reproducible FDS surfaces with 20 minutes of reaction time. Samples prepared in this manner, liquid phase deposition, are referred to as LIQFDS. Very short reaction times strongly suggest that the FDCS molecules were hydrolyzing and condensing in solution rapidly to form large aggregates that deposited on the surface. Large numbers of aggregates were identified on surfaces prepared without using optimized reaction parameters using optical microscopy. Rapid deposition kinetics and significant role of water in the deposition solvent are in agreement with the results of Bunker et al., who studied the formation of FDS monolayers from different solutions.[31]

Deposition via the LB method proved more able to give reproducible results, as measured by AFM and contact angle. Using the LB method with FDES allows the molecules to be individually hydrolyzed, and then to react with each other in an ordered manner on the water surface. This prevents aggregate formation, which

plagues the solution deposition method and allows deposition of the highest density monolayers. Shown in Figure 3.5 is the surface pressure isotherm of FDES, with a plateau corresponding to the transition between isolated gas phase molecules and a condensed solid phase. Ohnishi et al. found a similar isotherm for the same molecule.[71] Deposition pressures just above and below the plateau, at 12mN/m and 17mN/m were investigated. Samples deposited at 12mN/m are referred to FDS12 and those deposited at 17mN/m are called FDS17 hereafter.

Representative images of FDS SAMs prepared via liquid phase deposition and LB deposition are shown in Figure 4.6. These images are from samples deposited on Si/SiO₂ wafers, which show the differences in monolayer structure more clearly than glass substrates. Differences in monolayer structure are expected to be significant for FDS12 and FDS17 samples because of the different average molecular areas (27\AA^2 and 23\AA^2) and phases of FDES, as seen in Figure 3.5. An uncoated wafer, shown in Figure 4.6(a), is very flat without the low amplitude roughness of a glass substrate, as seen in Figure 4.1(a). A sample deposited from the liquid phase, LIQFDS, is shown in Figure 4.6(b) and is covered in polymer aggregates of FDS of varying size and lower islands indicative of multilayer growth, similar to the topography of FDS layers deposited from isooctane.[31] LIQFDS samples have static water contact angles of $110 \pm 2^\circ$. A sample deposited at 17 mN/m, FDS17, shown in Figure 4.6(c), appears very similar to LIQFDS with a flat background and small aggregates on the surface. The aggregates are due to the FDS molecules beginning to pile up on each other as

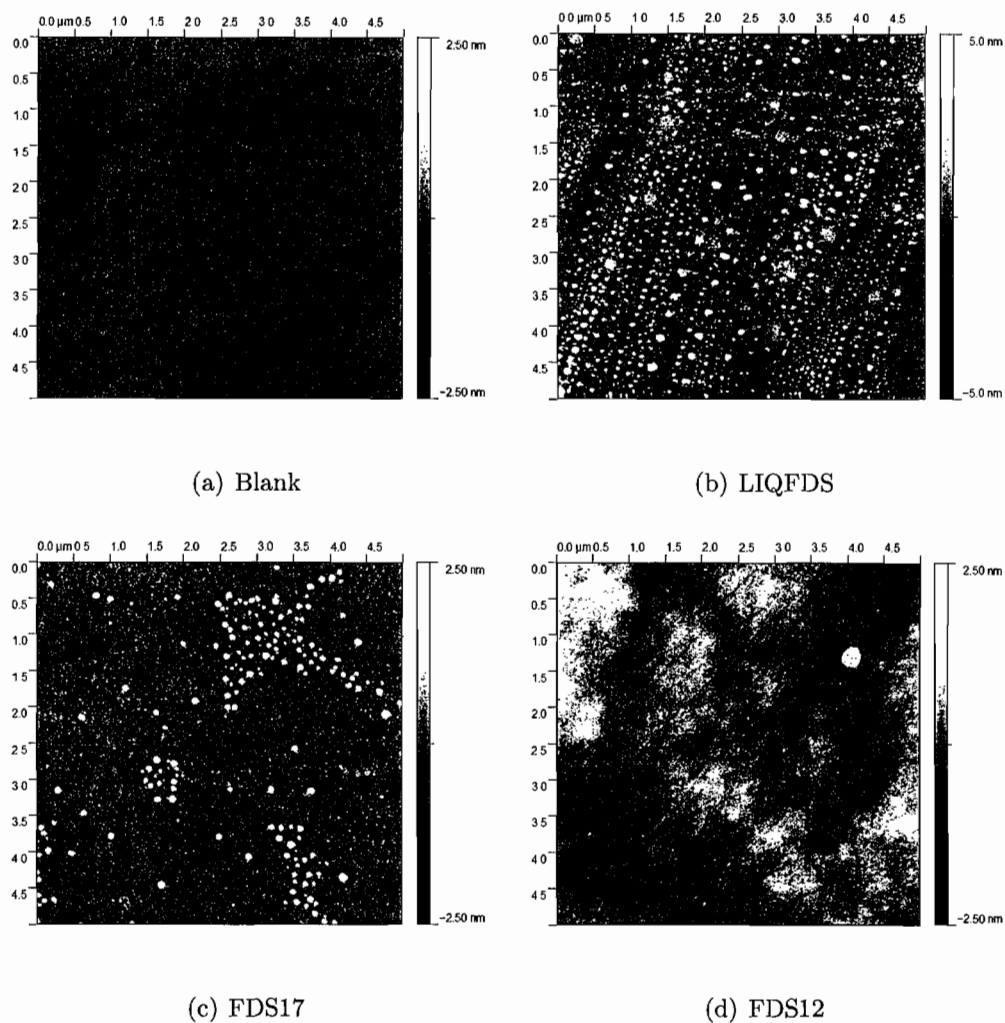


Figure 4.6. Tapping mode AFM images of three FDS monolayers on Si/SiO₂ wafer substrates. (a) Representative scan of a Si/SiO₂ wafer before deposition. (b) Sample prepared from FDCS precursors in the solution phase and is covered with polymerized FDS. (c) Monolayer deposited from FDES precursors via LB deposition at 12 mN/m and (d) Sample deposited at 17 mN/m.

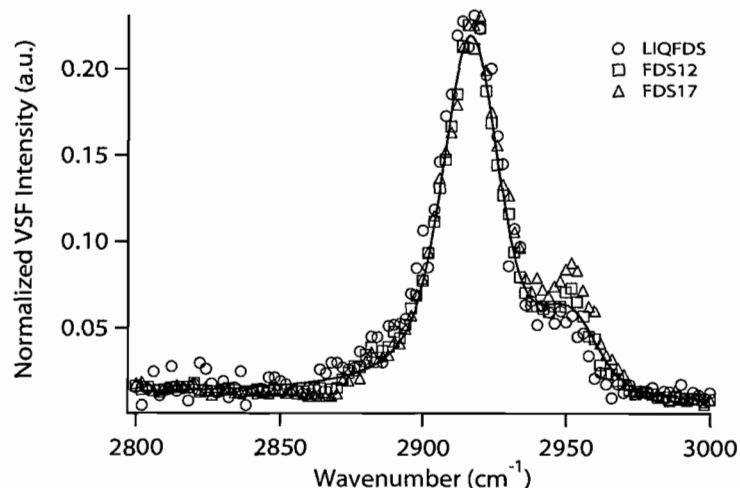


Figure 4.7. VSFS spectra of the FDS/air interface for LIQFDS, FDS12 and FDS17. The solid line is a fit to LIQFDS. The data are normalized to appear on the same scale and are all SSP polarized.

the film is compressed in the solid phase on the trough surface. FDS17 samples have a contact angle of $113 \pm 2^\circ$. A sample deposited at the lower pressure of 12mN/m, FDS12, is shown in Figure 4.6(d) and is quite different from the other samples. FDS12 is free of polymer aggregates and has an amorphous, cloudy appearance. As FDS12 samples were deposited prior to the phase transition, the FDS is in a more expanded state and will not deposit as a well-ordered coating. Despite this, the average water contact angle of samples prepared this way was $111 \pm 1^\circ$. The relatively high contact of all the surfaces indicate that they are all highly covered with FDS, with the sample deposited at 17 mN/m slightly more highly covered or better ordered.

Differences in FDS layer topography suggest that the SAM structures, as measured by VSFS may also be distinct. To examine this, VSFS spectra of monolayers from the three different deposition conditions in air were collected and are shown in Figure 4.7.

After normalizing and scaling the spectra, it is clear that they are identical. Slight differences in the spectra shown are within the variations of depositions; on a given sample, the spectra were found to be constant at multiple locations. The CH_2 signal arises from the FDS monolayer and not solely FDS aggregates, as aggregates are not present on FDS12, which has the same spectrum as the other samples.

Spectral fitting of the CH_2 resonances yields two peaks of opposite phase at $2918 \pm 1 \text{ cm}^{-1}$ and $2949 \pm 2 \text{ cm}^{-1}$. These resonances are due to the $\text{CH}_2(\text{as})$ vibrations of the two methylene spacer groups in the FDS molecule separating the CF portion of the chain from the Si atom and are split due to their unique intramolecular bonding environments. In contrast to a well-ordered ODS chain, the signals from the CH_2 groups do not cancel out because each of the two methylene groups in the FDS chain is in a unique molecular environment. The low energy resonance is in agreement with reported locations of the $\text{CH}_2(\text{as})$ of ODS SAMs earlier in this work and with literature reports.[89] The second peak is shifted from its native location at 2917 cm^{-1} due to chemical bonding with the electron withdrawing silicon atom. Shifts of this magnitude have previously been seen for methyl groups directly bound to silicon.[95] The opposite phases of the two groups are attributed to the different orientations of their transition dipole moments, possibly due to a systematic gauche defect similar to that seen in SDS at air/water interfaces.[107–109] The CF_3 and CF_2 portion of the monolayer chains lies outside the IR range of this laser system, as a result these modes have not been investigated.

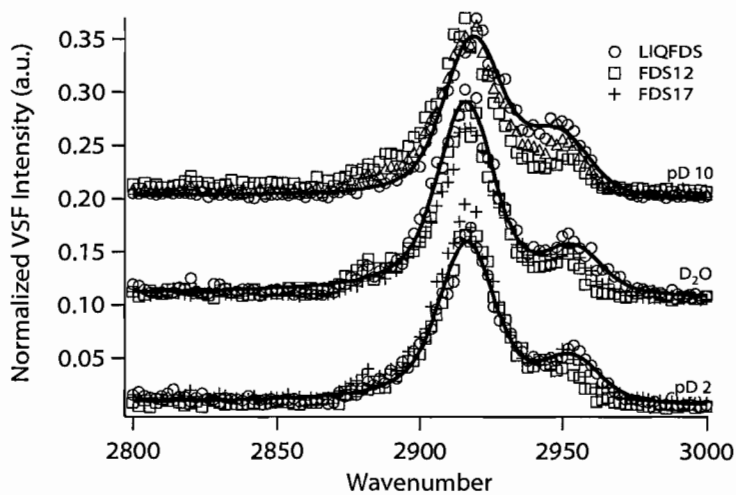


Figure 4.8. SSP spectra of the CH stretching region of FDS12, FDS17 and LIQFDS monolayers in pD 10 D_2O , D_2O and pD 2 D_2O . The solid lines are fits to the LIQFDS data. The spectra of each solution have been normalized to appear on the same scale and offset for clarity.

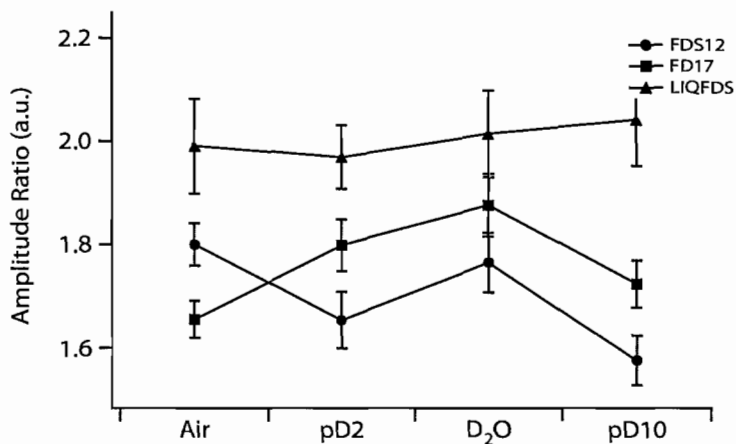


Figure 4.9. Fit amplitude ratios of the two CH_2 peaks of FDS12, FDS17 and LIQFDS.

While the monolayer topography does not affect the CH_2 group orientation in air, the significant differences in contact angle suggest that the surface coverages are different, which will alter the interactions of water with the FDS surfaces. Figure 4.8 shows the spectra of the different FDS/ D_2O interfaces. Visual comparison of these spectra reveals only minor differences between the different monolayer preparations on this portion of the monolayer chain. Spectral fitting reveals that the peaks of the monolayers remain located at $2918 \pm 1 \text{ cm}^{-1}$ and $2949 \pm 2 \text{ cm}^{-1}$ and the widths remain a constant $10.5 \pm 0.5 \text{ cm}^{-1}$ for both peaks. There are small variations in the fit amplitudes of the peaks, but comparison of the ratio of the peak intensities in air and D_2O in Figure 4.9 shows the differences to be minor. This indicates that the interaction of water molecules with the FDS coatings does not change the structure of the methylene spacer. However, the CH_2 groups are at the bottom of the monolayer chain and will be somewhat conformationally locked by the van der Waals interactions of the chains and their position near the fully coordinated silane linkage. A recent molecular dynamics study of a perfluorodecyl monolayer found that water has little effect on the monolayer conformation when the molecular area is 28 \AA^2 per molecule,[110] which is near the mean molecular area used in the LB depositions.

How water is affected by the different monolayer structures was investigated by collecting SSP polarized VSFS spectra of the FDS/ H_2O interface for each of the sample types, shown in Figure 4.10. In pure H_2O , the middle traces of Figure 4.10, the spectra are nearly identical. Two narrow modes of the $\text{CH}_2(\text{as})$ resonances, a broad

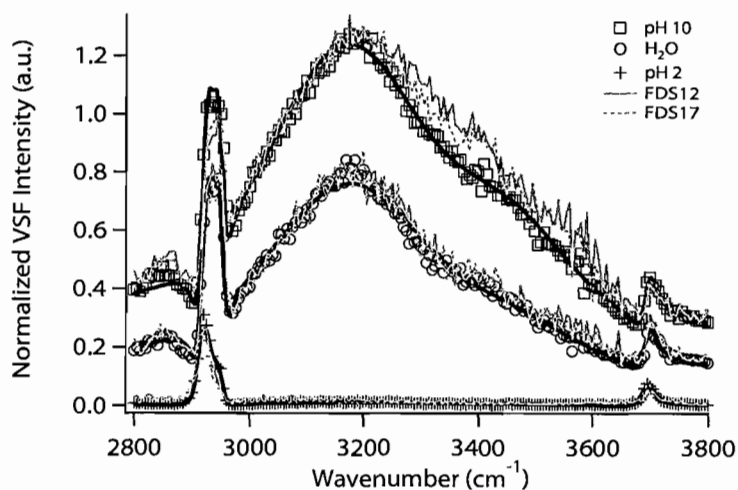


Figure 4.10. Spectra of FDS12, FDS17 and LIQFDS monolayer/water interfaces at pH 10, H₂O and pH 2 in the SSP polarization. The solid black lines are fits to the data points of LIQFDS. The spectra are offset for clarity.

band centered near 3200 cm^{-1} and a narrow mode near 3700 cm^{-1} are all apparent in the water spectra. The CH₂ mode at 2949 cm^{-1} appears to be larger in water than in D₂O, but spectral fitting shows this is due to interference effects. Coordinated water region of the spectra can be fit with two broad modes at $3209 \pm 2\text{ cm}^{-1}$ and $3435 \pm 3\text{ cm}^{-1}$ that model the range of water coordination environments present at this interface. This narrow mode at $3694 \pm 1\text{ cm}^{-1}$ is due to the previously described free-OH mode. This frequency is higher than for the hydrocarbon SAMs (3672 cm^{-1}), indicative of the weaker water-fluorocarbon interaction. At the air/water interface, the free-OH is located at $\approx 3705\text{ cm}^{-1}$. [111]

For ODS interfaces with H₂O, there is a large coordinated water signal, suggesting that there is a significant electrostatic field orienting interfacial water at the FDS/H₂O interface. To determine if the electrostatic behavior of FDS is the same as ODS and

SiO₂ surface was examined at high and low pH in D₂O and H₂O. VSFS spectra of FDS12, FDS17 and LIQFDS in D₂O at pD 2 and 10 are shown in Figure 4.8. None of the VSFS spectra are affected by the change in pD, which can be clearly seen by comparing the amplitude ratios of the two CH₂ peaks in Figure 4.9. While the ratios are slightly different for the different films, they are constant in each environment within a given film.

Spectral behavior of H₂O at the FDS interfaces with changes in pH is similar to that seen at ODS surfaces. At high pH, when the SiO₂ substrate should have a large negative charge, the number of coordinated water molecules with dipole components normal to the interface increases. This is seen in the pH 10 VSFS spectra (\square) in Figure 4.10 by an increase in the signals at 3209 cm⁻¹ and 3435 cm⁻¹. At pH 2, when a bare SiO₂ substrate is uncharged there should be less electrostatically oriented water, resulting in a decreased SSP VSFS signal. Almost no signal from coordinated water molecules is found in the pH 2 spectra ($+$) of Figure 4.10, indicating that the electric field that orients interfacial water molecules normal to the interface is nearly zero. This behavior of increasing water signal with increasing pH is the same as that seen with the HQODS samples. There are a few small differences between the spectra of FDS17, LIQFDS and FDS12. FDS12 and FDS17 both have more intensity in between 3200 and 3600 cm⁻¹ than LIQFDS, indicating that the hydrogen bonding environments are slightly different between the liquid phase deposited film and the LB films. There also appears to be a small shoulder near 3600 cm⁻¹ present in these two

films, indicating possible entrapment of water molecules in the monolayers. However, these differences are small and not highly reproducible from deposition to deposition. The general trend of decreasing water signal with decreasing pH is apparent across all the samples tested, as is the increased coordinated water signal of FDS relative to ODS.

A greater water signal means that the effective electric field at the interface must be greater at the FDS surfaces than at the ODS surfaces. Zeta potential measurements at FDS and ODS surfaces show very similar electrokinetic behavior and have suggested that the surface potential originates from the SiO₂ substrate.[33, 106] SiO₂ is typically a highly charged solid and has been shown to be only partially directly bonded with silane monolayers and unaffected by the functionality of the monolayer forming molecules.[85, 101] If one assumes that the substrate is the source of the interfacial potential and is equally charged with FDS and ODS monolayers, then the most like reason for a difference between the two monolayer types is the difference in capacitance between the monolayers. The Stern model is commonly used to explain behavior at highly charged interfaces and detailed explanations of the model can be found in the literature.[112, 113] The potential drop over a layer of constant capacitance is given by:

$$\psi_0 - \psi_d = \frac{-\sigma_0 d}{\epsilon \epsilon_0} \quad (\text{IV.1})$$

Where ψ_0 is the surface potential and ψ_d is the potential on the other side of the Stern layer. The surface charge is σ_0 , d is the layer thickness, ϵ and ϵ_0

are the relative permittivity of the medium and the permittivity of free space. Taking the surface potential of SiO_2 as -35 mV at near neutral pH,[102, 114] and the charge density as $-3.2 \times 10^{-4} \frac{\text{C}}{\text{m}^2}$,[115] chemical specific parameters of the monolayers can then be used to calculate the electric potential at the monolayer surface. Dielectric constants of FDS and ODS SAMs are estimated as having values equivalent to those of polytetrafluoroethylene and polyethylene, which are 2.1 and 2.33, respectively.[116] The thickness of the FDS layer was assumed to be 1.1 nm and the ODS monolayer 1.9 nm, based on ellipsometry measurements by Hozumi et al.[33] Using these parameters, the potential at the FDS surface is -16 mV and -5.5 mV for the ODS layer. This large difference in interfacial potential partially explains why there are more oriented water molecules at the FDS/water interface than at the ODS/water interface. Additionally, fluorocarbons have larger van der Waals diameters than hydrocarbons, 5.6 and 4.2 \AA , respectively,[117] which may create more strain on the Si-O-Si crosslinks ($\approx 4 \text{ \AA}$)[118] at the base of the monolayer and lead to more defects in the SAM, allowing more water to access the surface.

It is important to note that recent phase-sensitive VSFS results suggest that the isoelectric point of ODS surfaces is near pH 3 because of competitive adsorption of H^+ and Cl^- and OH^- at the hydrophobic surface. The adsorption of ions at this interface creates an electrostatic field which then orients water molecules, giving rise to the observed VSFS response in the coordinated water stretching region.[98] Because

the experiments in this chapter are not ionic strength controlled, this possibility has not been investigated.

Conclusion

Two types of monolayers, hydrocarbon and fluorocarbon, have been prepared in different ways to determine the sensitivity of VSFS to the surface morphology. Using AFM and contact angle, clear differences in the surfaces of these monolayers can be seen. Large number of aggregates on the hydrocarbon surface decrease the contact angle and significantly alter the surface topography. Changes in the deposition method of the fluorocarbon SAMs do not result in different static water contact angles, but do affect the monolayer structure itself. However, none of the differences in ODS or FDS SAM structure result in obvious changes in the VSFS spectra of the SAM/air interface. Caution must therefore be used when using VSFS to determine the quality of self-assembled monolayers.

When in water, however, VSFS can help discern differences. For hydrocarbon SAMs, VSFS results show that the chains have some flexibility due to imperfections in the monolayer. The effect of these imperfections is more apparent when one analyzes the OH stretching modes. For the low quality hydrocarbon monolayers, one sees more penetration of water into the chains towards the surface and a significantly more highly charged surface due to the greater area of the SiO₂ substrate that is solvent accessible. This is manifested in the stronger water signal at the low quality monolayer

surface relative to the high quality monolayer. These results provide examples of spectral signatures indicative of lower quality SAMs, particularly in the OH stretching region. Despite the differences in the water region, there is not any signal that can be obviously attributed to surface aggregates, as one might expect since these CH modes are most likely very random in orientation. VSFS of the fluorinated surfaces, for which only the methylene groups have been analyzed, show that these groups are insensitive to immersion in water and pH, which is explained by their close proximity to the surface bonding group. Differences in surface morphology of the fluorocarbon SAMs do not lead to significant deviations in the structure of interfacial water molecules at the monolayer/water interface. This is due to the smaller thickness of the fluorocarbon layer tested which allows the interfacial electric field at the monolayer terminus to be significantly stronger at pHs above the isoelectric point. Thus, the coordinated water molecules appear to be dominated by electrostatic effects not monolayer specific interactions. These electrostatic effects and the monolayer specific interactions are studied in more detail in the next chapter using ionic strength controlled pH solutions to reveal the differences in interfacial bonding more clearly.

CHAPTER V

EFFECTS OF DIFFERENT HYDROPHOBIC COATINGS ON INTERFACIAL
WATER STRUCTURE

The previous chapter leaves open the question of interfacial charge and how much of the interfacial water structure, as revealed by VSFS, is intrinsic ($\chi^{(2)}$ effect) versus electric field generated ($\chi^{(3)}$ effect). This chapter seeks to answer this question, as well as determine the source of the water signal at the monolayer interfaces - above, within or below the monolayer chains. To do this, the interfacial structure of water has been examined at fluorocarbon and hydrocarbon self-assembled monolayers, as well as at a thin film of Z Dol 4000 perfluoropolyether lubricant. Using a combination of vibrational sum-frequency spectroscopy, contact angle goniometry and atomic force microscopy, permanent changes have been observed in the structure of Z Dol lubricant films, but not FDS or ODS monolayers, after short exposures to water. These changes are understood in terms of penetration of the polymer coating by water and subsequent removal of loosely bound material. This water penetration gives rise to VSFS response that is nearly identical to the $\text{SiO}_2/\text{H}_2\text{O}$ interface, which is found to have a unique spectroscopic signature. Fluorocarbon and hydrocarbon monolayers have distinctly different characteristic spectra from their direct interactions with water molecules. The differences in interfacial water speciation at the FDS, ODS

and Z Dol surfaces is revealed by constant ionic strength titrations and salt screening experiments.

Introduction

Microelectromechanical (MEMs) and other lithographically produced systems are increasingly used for applications in aqueous environments.[119–123] To prevent water from degrading these devices uniform, durable hydrophobic coatings are required. One of the most common strategies for hardening such devices to their environments involves using micro and nanoscale organic coatings to reduce wear or otherwise improve aqueous compatibility.[20, 80, 81, 124–129] One way to attain high durability and small thickness is to use chemically bonded coatings[20, 130–132] and fluorinated materials.[15, 133, 134] Fluorocarbon and hydrocarbon self-assembled monolayer (SAM) and polymer coatings have been heavily investigated as coatings to alter the tribological,[80, 129, 130] chemical[79, 135–137] and biological[138–140] properties of surfaces. Despite this, little is known about how differences in chemical functionality affect the structure of interfacial water molecules.

A nearly ideal tool for investigating these unknowns is vibrational sum-frequency spectroscopy (VSFS) because it is inherently sensitive to interfacial structure, owing to the nature of the nonlinear optical process which produces the signal. VSFS has been used to investigate the structure of numerous polymer surfaces in aqueous environments[141–148] as well as several different SAMs.[43, 88–90, 98, 149–151]

These studies have found that immersion in water and/or coating these surfaces with surfactants and other adsorbates can significantly affect the structure of polymer coatings. However, only a few studies have been undertaken to examine the aqueous structure at solid polymer or SAM interfaces.[88–90, 146–148] VSFS and zeta potential studies have found significant bulk pH driven effects at the hydrocarbon silane/SAM water interface and attributed them to the changes in the charge state of the SiO_2 substrates[33, 89] and the preferential adsorption of OH^- and Cl^- ions to these hydrophobic interfaces.[98]

The results in this chapter address both the effects of ion adsorption and the chemical functionality of hydrophobic surfaces on interfacial water structure and show distinct differences in interfacial water structure at the surfaces, despite similarities in thickness and hydrophobicity. This is done by examining three different thin film coatings on fused silica: ODS SAMs, 1H,1H,2H,2H-perfluorodecylsilane (FDS) SAMs and Fomblin Z Dol 4000 (Zdol). These surfaces have been studied over a range of ionic strengths at pH 5.8 and constant ionic strength phosphate buffer solutions at pH 2, 7 and 11, then compared to a bare SiO_2 substrate as a control. Further characterization of the surfaces was done by contact angle and atomic force microscopy (AFM) to evaluate the effects of water on the coating structures.

Experimental

The VSFS experiments were performed as described in Chapter III. A minimum of three spectra were collected for each interface studied with a 4 cm^{-1} resolution at 20 shots per data point. All spectra were corrected for visible light scatter detected by the photomultiplier tube (PMT) and then normalized for the visible and IR energy. Finally, spectra were corrected for IR absorption by the prism and sample. Because of the wide range of measured VSFS signal intensities in these experiments, the voltage of the PMT was varied as needed between 850 and 1500 V. All the data were analyzed after scaling to 850 V sensitivity levels unless otherwise noted.

Sample characterization was carried out using the home built goniometer and AFM measurements were performed as described in Chapter III. All reported contact angles are averages of 10 individual measurements. The FDS samples, because of deposition size restrictions, were blown off with argon after 5 measurements before new images were collected.

All substrates used in these experiments were 0.0625 in. thick GE-124 glass from Behm Quartz, 2.25×1.25 in. size. Fused silica spectra were collected on substrates prepared as in Chapter III but not deposited on. Coated samples were prepared as in Chapter III.

Phosphoric acid buffers of pH 2, 7 and 11 were prepared from phosphoric acid and its sodium salts with an ionic strength of 0.01 M. Because of the fairly low ionic strength of these solutions, adsorption of atmospheric carbon dioxide caused

pH changes in the pH 7 and 11 buffers over a few days. Ionic strength effects were examined using NaCl solutions at $\text{pH} \approx 5.8$. Solutions were made by serial dilution of a 1 M NaCl(aq) solution to 1×10^{-4} M. Because the VSFS setup does not isolate the sample from the atmosphere, effects of NaCl at lower concentrations than this were irreproducible. To ensure consistency in the spectra, both in terms of ionic strength and pH, fresh solutions were made each day.

Results and Discussion

The principle behind the two types of VSFS experiments in the sections below is the decoupling of $\chi^{(2)}$ effects in the VSFS results from $\chi^{(3)}$ effects. In Chapter II, it was noted that in the case of large electrostatic fields, such as those present at SiO_2 surfaces, the sum frequency response of the medium contains contributions from both effects. The induced sum-frequency polarization can be written as:

$$\vec{P}_{SFG} = \chi^{(2)} \vec{E}(\omega_{vis}) \vec{E}(\omega_{IR}) + \chi^{(3)} \vec{E}(\omega_{vis}) \vec{E}(\omega_{IR}) \vec{E}(\omega_0) \quad (\text{V.1})$$

where the second term is the third-order nonlinear polarization term and contains the electrostatic field dependence, $\vec{E}(\omega_0)$, of the induced interfacial nonlinear polarization. Both of these components contribute to the nonresonant and resonant VSFS response. This third-order term arises from several factors, most notably the magnitude of the electric field itself and the alignment of molecules by this field. These electrostatically aligned molecules are no longer centrosymmetric, thus generating VSFS signal. Second harmonic generation and sum-frequency studies have shown that the intensity

of the nonlinear response is dependant on the interfacial potential, which is dependant on the surface charge density and the solution ionic strength.[52–54, 102, 152] Assuming that $\chi^{(3)}$ is constant over the entire interface and that the electrostatic field is proportional to the interfacial potential, $\Phi(0)$, the nonlinear polarization can be rewritten as:

$$\vec{P}_{SFG} = \left[\chi^{(2)} + \chi^{(3)} \vec{\Phi}(0) \right] \vec{E}(\omega_{vis}) \vec{E}(\omega_{IR}) \quad (\text{V.2})$$

and shows the dependance of the nonlinear polarization on the interfacial potential, $\vec{\Phi}(0)$. These same authors have shown that for surfactants at interface and nonspecific ionadsorption, the interfacial potential can be described by the Gouy-Chapman model:

$$\Phi(0) = \frac{2k_bT}{e} \sinh^{-1} \left[\sigma \left(\frac{\pi}{2\epsilon\epsilon_0 k_b T I} \right)^{\frac{1}{2}} \right] \quad (\text{V.3})$$

where σ is the surface charge density, $\epsilon\epsilon_0$ is the permittivity of the medium and I is the ionic strength of the solution.

Within the confines of the Gouy-Chapman model the depth of the interfacial region, called the electrostatic double-layer, can be expressed by the Debye-Hückle screening length which is written as:

$$\kappa = \left(\frac{\epsilon\epsilon_0 k_b T}{1000 e^2 I N_A} \right)^{\frac{1}{2}} \quad (\text{V.4})$$

where N_A is Avagadro's number, e is the charge of an electron, and I is the ionic strength of the bulk solution expressed in $mol L^{-1}$. From Equations V.3 and V.4 there are two ways to minimize the effect of $\chi^{(3)}$ on the measured VSFS spectra. First, the

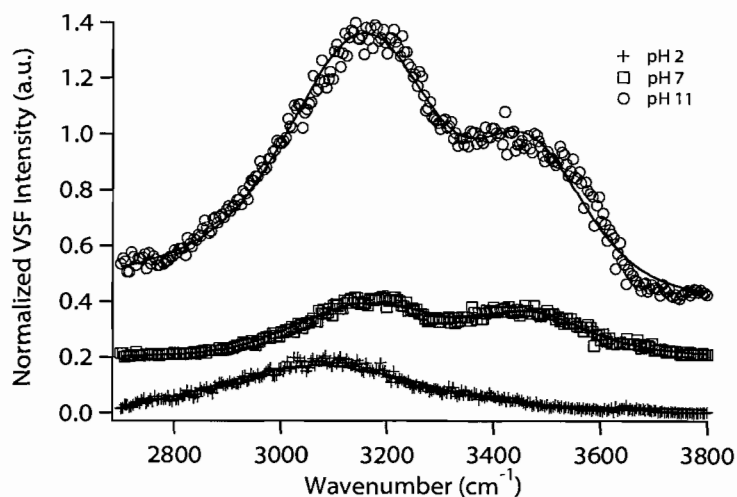


Figure 5.1. VSFS spectra of the $\text{SiO}_2/\text{H}_2\text{O}$ interface at different pH values with an ionic strength of 0.01 M. Solid lines are fits to the data. Spectra are offset for clarity.

interfacial potential can be decreased by decreasing σ , the interfacial charge. This is accomplished in these experiments by changing solution pH. When the surface charge goes to zero, only molecules inherently oriented by the interface generate VSFS signal. The second way is to vary the ionic strength. At a given interfacial charge, the depth of the double layer is decreased from 21 nm to 0.2 nm as the ionic strength is increased from 1×10^{-4} M to 1 M. This also has the effect of reducing the interfacial potential. Thus at high ionic strength only water molecules oriented by their direct interactions with the interface generate VSFS response.

$\text{SiO}_2/\text{Water}$ Interface

The baseline to which the three different surfaces will be compared is $\text{SiO}_2/\text{H}_2\text{O}$ interface, which has been well-described in the literature.[102, 137, 153, 154] At high pH, the $\text{SiO}_2/\text{H}_2\text{O}$ interface is highly negatively charged due to the deprotonation

of SiO-H groups on the SiO₂ substrate. This large negative charge generates a large electrostatic field that increases the double layer thickness resulting in more H₂O molecules being oriented. This results in a large VSFS signal. Decreasing the bulk pH reduces the number of deprotonated surface sites, reducing the interfacial electrostatic field until the surface is no longer charged, the point of zero charge (PZC), which is near pH 2.[102] At the PZC, second harmonic studies have still found signal which is not due to electrostatically oriented water molecules,[102] but inherent in the measurements. The VSFS results shown in Figure 5.1 confirm this picture. At pH 11 the VSFS signal is large due to the electrostatic orientation of water molecules and the spectrum appears to consist of two broad peaks near 3200 and 3450 cm⁻¹. These peaks correspond to more strongly and more weakly coordinated species, respectively. Decreasing the pH to 7 decreases the surface charge, reducing the interfacial potential and thus the number of oriented water molecules, which decreases the VSFS intensity. Further decreasing the pH to 2 reaches the PZC of the SiO₂/H₂O interface, where there is no interfacial potential, but VSFS signal persists. Because these spectra are at constant ionic strength, the double layer thickness is invariant. With no surface charge to orient water molecules, the PH2 VSFS spectrum is a produce of species inherently oriented by their interactions with SiO₂. These spectra are similar to results by Ostroverkhov *et al.*[153, 154] who found decreasing VSFS signal at the SiO₂ and quartz/H₂O interfaces with decreasing pH, but that the signal did not go to

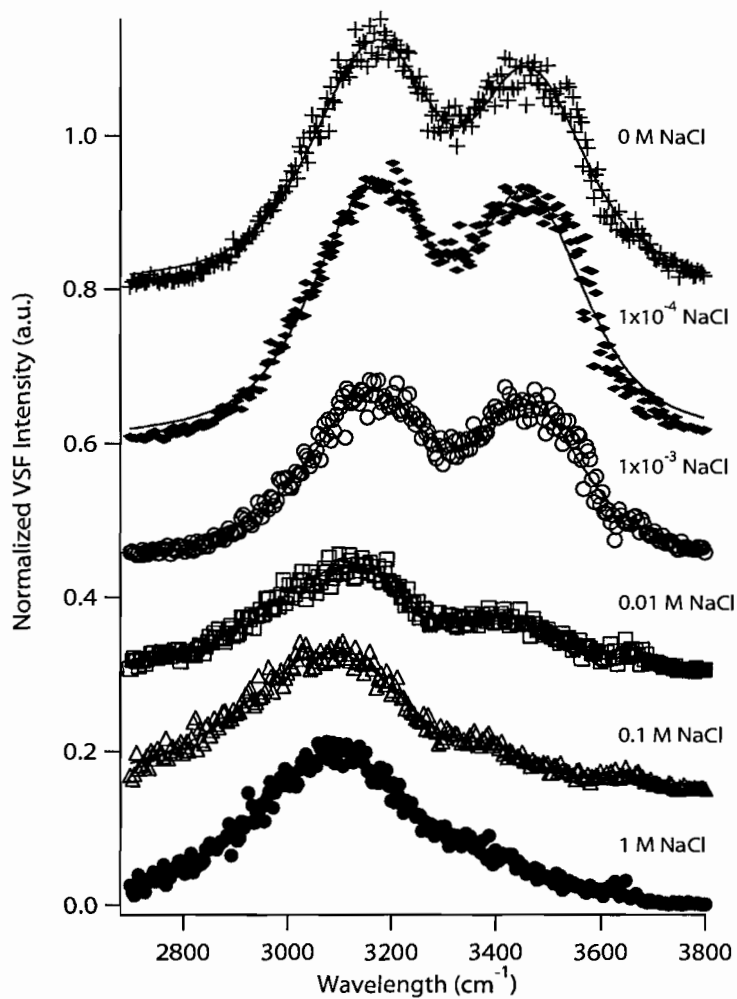


Figure 5.2. VSFS spectra of the $\text{SiO}_2/\text{H}_2\text{O}$ interface at pH 5.8 with increasing NaCl ionic strength. Solid lines are fits to the data. The spectra are offset for clarity.

zero at the PZC. The results also confirm the picture of protonation/deprotonation as a key cause of H_2O orientation.

The effect of increasing ionic strength on interfacial water structure at pH 5.8 is shown in Figure 5.2 and confirms the results of the pH series. Whereas the pH series modifies the surface charge to reveal interfacial species, the ionic strength series holds

the surface charge constant, but compresses the double layer. At this pH, the SiO_2 surface is negatively charged, but significantly less so than at pH 11. It has been estimated that slightly more than 20% of the deprotonatable surface sites have done so at this pH, versus nearly 100% at pH 11.[102] At a suitably high NaCl concentration, the screening length of the ions, plus their disruptive effects on the hydrogen bonding network of the electrostatically oriented water molecules will completely negate the surface charge effects and reveal those molecules directly interacting with the substrate. This is what is seen; the pure water spectrum is dominated by two peaks at ≈ 3200 and $\approx 3450 \text{ cm}^{-1}$ and is qualitatively similar to the pH 7 and 11 spectra in Figure 5.1. At $1 \times 10^{-4} \text{ M}$ NaCl, the VSFS spectrum is virtually unchanged from that of pure water. Increasing the ionic strength to $1 \times 10^{-3} \text{ M}$ decreases the overall intensity of the spectrum, but does not alter the shape. Increasing the ionic strength further, to 0.01 M and higher, results in significant changes in spectral shape yielding a spectrum nearly identical to the that seen at pH 2. This indicates that the interfacial water molecules directly interacting with SiO_2 experience the same interactions as at pH 2. The maximum of this new intensity distribution is near 3050 cm^{-1} , which is redshifted by over 100 cm^{-1} from the maximum at low ionic strength.

Because of the major changes in the spectral distribution with changing ionic strength, which should not alter the speciation at the SiO_2 surface, the source of the distribution change in the spectra is not intuitive. The presence of Na^+ and Cl^- ions in the interfacial region is not expected to increase the hydrogen bonding of water

molecules based on both the need of the ions to be solvated and that neither Cl^- nor Na^+ have been found to increase the intensity in the hydrogen bonding regions of interfacial water spectra at the CaF_2 ,^[155] CCl_4 ^[156] or air^[111] interfaces. To analyze the behavior of this interface and fully understand what species are present, the spectra were globally fit using a nonlinear fitting routine in IgorPro. Traditionally, the coordinated water stretching region at charged solid/liquid interfaces is described with two broad peaks representing different degrees of intermolecular water hydrogen bonding.^[154, 157, 158] However, recent phase sensitive VSFS measurements at the $\text{SiO}_2/\text{H}_2\text{O}$ interface have described the interface as having three broad peaks: a region of more asymmetrically coordinated water near 3450 cm^{-1} , a region of strongly coordinated water near 3200 cm^{-1} and a third peak near 3050 cm^{-1} . This 3050 cm^{-1} peak has opposite phase relative to the other coordinated water peaks and has been attributed to species directly bonded with the SiO_2 substrate.^[153] This interpretation describes the results of the pH and ionic strength studies quite well.

Figure 5.3a shows the VSFS spectrum of the neat $\text{SiO}_2/\text{H}_2\text{O}$ interface shown in 5.2 with best fits from two different fitting schemes, a two peak model and a three peak model, as proposed by Ostroverkhov et al.^[153] Both models fit the data quite well; the deconvolution of each model into its resonant components is shown in 5.3b and 5.3c. The three peak model uses three broad peaks: a negative peak at 3048 cm^{-1} , and two positive peaks at 3194 cm^{-1} and 3430 cm^{-1} . The negative amplitude of the 3048 cm^{-1} peak represents it being out of phase with the other two peaks. The two

Table 5.1. Comparison of spectral fitting parameters for the two models used to describe the SiO₂/H₂O interface. A negative amplitude means the peak has opposite phase to a positive amplitude peak.

Solution	Two Peak Model Parameters			Three Peak Model Parameters		
	Amplitude	Location (cm ⁻¹)	Width (cm ⁻¹)	Amplitude	Location (cm ⁻¹)	Width (cm ⁻¹)
Water	—	—	—	-0.45±0.01	3053±1	187±1
	0.54±0.02	3202±5	144±9	0.55±0.01	3210±1	137±1
	0.46±0.03	3436±5	123±8	0.48±0.01	3457±1	129±1
1 × 10 ⁻⁴ M	—	—	—	-0.45±0.01	3053±1	187±1
	0.55±0.02	3199±4	144±7	0.56±0.02	3210±1	137±1
	0.49±0.01	3433±6	126±7	0.51±0.01	3457±1	129±1
1 × 10 ⁻³ M	—	—	—	-0.45±0.01	3053±1	187±1
	0.44±0.02	3197±6	145±10	0.40±0.01	3210±1	137±1
	0.39±0.02	3432±5	119±8	0.40±0.01	3457±1	129±1
0.01 M	—	—	—	-0.45±0.01	3053±1	187±1
	0.36±0.01	3155±10	181±10	0.27±0.01	3210±1	137±1
	0.19±0.02	3417±10	110±17	0.20±0.01	3457±1	129±1
0.1 M	—	—	—	-0.45±0.01	3053±1	187±1
	0.41±0.01	3133±8	196±7	.017±0.012	3210±1	137±1
	0.14±0.02	3402±12	10±21	0.06±0.01	3457±1	129±1
1 M	—	—	—	-0.45±0.01	3053±1	187±1
	0.45±0.01	3110±8	189±6	0.03±0.01	3210±1	137±1
	0.09±0.02	3375±15	98±27	0.12±0.02	3457±1	129±1
pH 11	—	—	—	0.21±0.09	3053±1	187±1
	0.99±0.01	3190±1	199±1	0.78±0.09	3178±1	198±1
	0.40±0.01	3449±2	103±3	0.42±0.02	3443±2	110±3
pH 7	—	—	—	-0.43±0.03	3053±1	187±1
	0.39±0.01	3177±2	120±2	0.42±0.03	3209±1	135±1
	0.38±0.01	3403±1	150±12	0.35±0.02	3456±2	132±2
pH 2	—	—	—	-0.51±0.01	3053±1	187±1
	0.36±0.01	3052±1	193±1	0.18±0.02	3223±1	135±3
	0.05±0.01	3300±6	150±12	0.08±0.02	3438±5	100±7

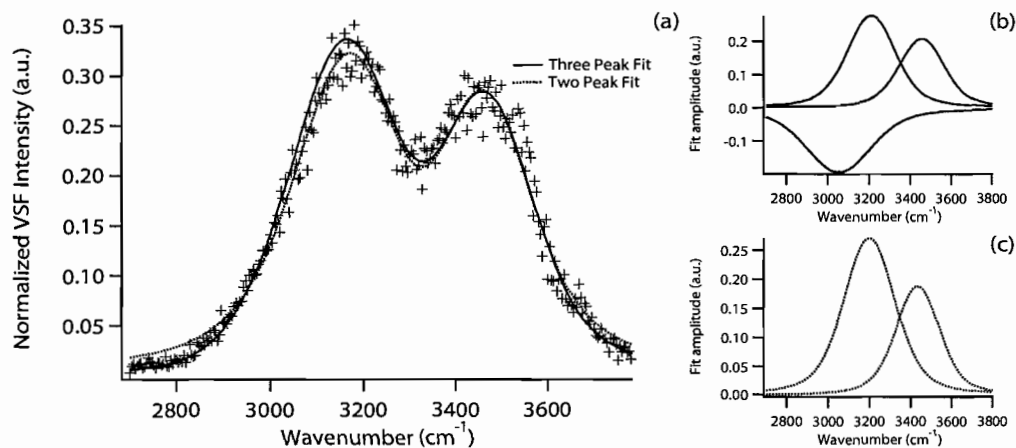


Figure 5.3. (a) VSFS spectrum of the neat $\text{SiO}_2/\text{H}_2\text{O}$ interface with two different fitting schemes: (b) three peak fit and (c) two peak fit.

peak model uses two broad peaks centered at 3200 cm^{-1} and 3430 cm^{-1} . All of the individual spectra can be well fit using either model. To avoid over determining a system, or adding a peak just to make the fits better, there needs to be a compelling justification for the additional peak.

Table 5.1 shows the resonant fitting parameters used to fit all the $\text{SiO}_2/\text{H}_2\text{O}$ spectra. As the results of the fitting show, fitting with only two peaks requires significant changes in the peak width and location in addition to the amplitude for both the ionic strength series and the pH data. This suggests that both NaCl and H^+/OH^- can alter both the surface species and interfacial hydrogen bonding. At high ionic strengths, Na^+ can adsorb to the negatively charged silanols and effectively neutralize them, reversing the orientation of water molecules directly engages in hydrogen bonding with the substrate.[159, 160] However, this also suggests that new water bonding species are being created at the interface. Since only a small percentage

of the surface silanols are deprotonated,[102] there should be very little specific adsorption of Na^+ . By comparison, the three peak model successfully describes the ionic strength results by only varying the amplitudes of the higher energy peaks. The wavelengths and widths of all the peaks remain constant. Furthermore, the peak at 3050 cm^{-1} only changes in amplitude in the pH series, when the protonation of the SiO_2 surface changes. This pH result is in agreement with the results of Ostroverkhov et al.[153] Given the agreement with the phase sensitive measurements, the ability to use non-varying spectral fitting parameters and the experimental findings at other interfaces[111, 155, 156] that Na^+ and Cl^- do not enhance the hydrogen bonding environment, it is clear that there are three principle bonding environments at the $\text{SiO}_2/\text{H}_2\text{O}$ interface. The first is an environment indicative of water molecules directly interacting with protonated SiO_2 and otherwise inherently oriented by the interface and is modeled by a broad mode near 3050 cm^{-1} . The second environment is that of strongly coordinated, electrostatically oriented water molecules that are modeled by a broad mode near 3200 cm^{-1} . The final environment is that of more weakly coordinated, electrostatically oriented water molecules represented by a band near 3450 cm^{-1} . Adding NaCl to the interface screens the electrostatic field and reduces the intensity of the two modes representing the electrostatically oriented water, but has no effect on the directly interacting water molecules. Altering the bulk pH, changes the interfacial charge by changing the protonation of the fused silica and thus affects all three hydrogen bonding environments.

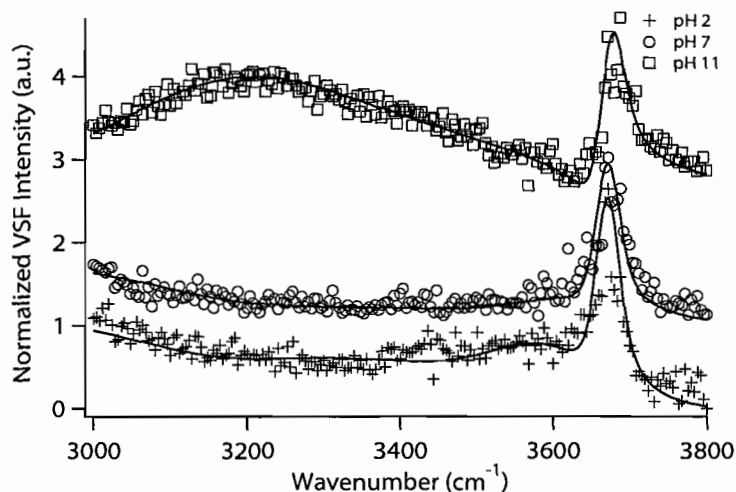


Figure 5.4. VSFS spectra of the $\text{SiO}_2/\text{ODS}/\text{H}_2\text{O}$ at 0.01 M ionic strength with bulk pH 2, 7 and 11. These spectra are enlarged 13.5 times the other intensity of the other interfaces shown in this report. Solid lines are fits to the data. Spectra are offset for clarity.

$\text{SiO}_2/\text{ODS}/\text{Water}$ Interface

With a clear picture of water at the SiO_2 surface, the different hydrophobic surfaces can be fully characterized; the first is ODS. The signal from the ODS chains themselves is much greater than that of the OH stretching modes and was not collected in these VSFS experiments so that the sensitivity could be increased to capture the H_2O signal with greater detail. However, based on AFM, contact angle and VSFS results of samples from this batch the ODS surface shown is believed to be a high-quality, uniform monolayer with chains in a nearly all-*trans* configuration. Figure 5.4 shows pH series spectra of this monolayer type. At high pH, the VSFS spectrum of this interface shows enhanced intensity in the coordinated water stretching region near 3200 cm^{-1} , consistent with a charged interface, due to adsorption of OH^- at the

ODS surface or deprotonation of the SiO_2 substrate. At neutral pH, the VSFS signal in the coordinated water region is minimized, suggesting that there is no charge at the interface, or that the charge is effectively screened at this ionic strength. The slope from 3000 to 3200 cm^{-1} is from the tailing of the CH stretching modes of the monolayer and is treated as a constant in the analysis. At pH 2, the VSFS signal increases slightly due to the positive charge of the interface. Streaming potential measurements of ODS/ H_2O interface have found the PZC of this interface to be near pH 3[33, 106] as opposed to pH 2 for bare SiO_2 , confirming that the interfacial charge is reversed under these conditions. There is also a narrow feature at $3672 \pm 2\text{ cm}^{-1}$ due to uncoupled OH oscillators at this interface of water molecules straddling the interface.

The NaCl solution spectra in Figure 5.5 show the same spectral features as the pH spectra. The pure water spectrum shows significant contributions from strongly coordinated water molecules near 3200 cm^{-1} . However, the addition of $1 \times 10^{-4}\text{ M}$ NaCl increases the signal which shows that Cl^- has some affinity for the ODS/water interface. A recent paper by Tian and Shen[98] found that Cl^- adsorbs to the ODS/water interface and that the surface coverage of Cl^- saturates at some concentration greater than $30\ \mu\text{M}$, which supports this observation. Increasing the ionic strength to 1 mM decreases the VSFS signal in the coordinated water stretching region, indicating that screening, not ion adsorption is responsible for the changes in the interfacial water structure from this concentration on. At ionic strengths greater than 0.01 M , a shoulder on the free-OH is apparent near 3600 cm^{-1} ; spectral

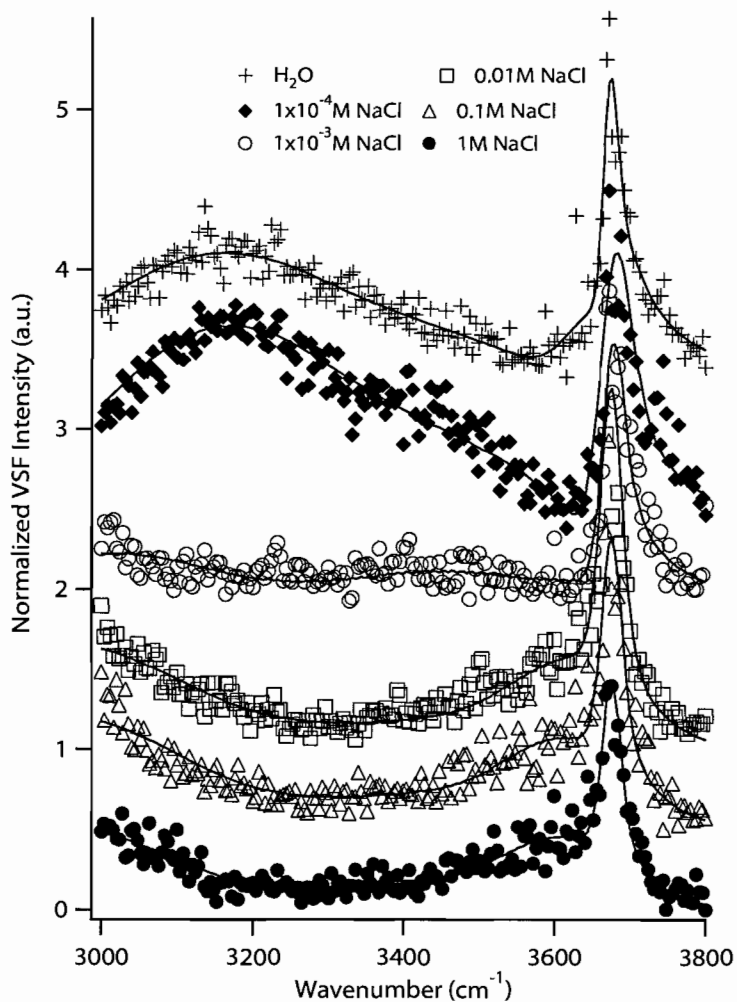


Figure 5.5. VSFS spectra of the $\text{SiO}_2/\text{ODS}/\text{H}_2\text{O}$ interface at pH 5.8 with NaCl. These spectra are magnified 13.5 times the sensitivity of the spectra at the other interfaces shown in this report. Solid lines are fits to the data. Spectra are offset for clarity.

deconvolution fits this peak to a constant location of $3620 \pm 5 \text{ cm}^{-1}$. This peak is also apparent in the pH 2 VSFS spectrum of this interface, shown in Figure 5.4. This location is similar to that proposed for solvated ions at several different interfaces.[111, 155, 161–163] The magnitude of this peak stays relatively constant across the conditions examined, with an amplitude of 0.11 ± 0.04 and a width of $83 \pm 8 \text{ cm}^{-1}$. If this peak were due to water molecules solvating Cl^- ions, its amplitude should increase with increasing concentration, which is not seen. Furthermore, Cl^- ions are not present in the pH 2 buffer solution, but rather dihydrogenphosphate. These different ions have different solvation enthalpies[164, 165] and their solvation shells would likely exhibit different interfacial frequencies, as seen in other interfacial studies.[111, 155] Thus, it can be concluded that this peak is due to water molecules in the ODS chains. Recent molecular dynamics simulations have shown that water molecules can penetrate into the alkyl chains of well-formed hydrocarbon monolayers.[97]

Despite this penetration of water molecules into the monolayer chains, the ODS sample does not have a peak at 3050 cm^{-1} indicative of water molecules directly interacting with SiO_2 , suggesting that there is not a layer of water between the SAM and the substrate, as has been suggested by some authors.[89] It may be that such a layer does exist, but is sufficiently random in orientation as not to be seen. The source of signal from H_2O at the ODS layer is water oriented by H^+ or OH^- ions adsorbed at this interface which create an electrostatic field and orient water molecules. The only

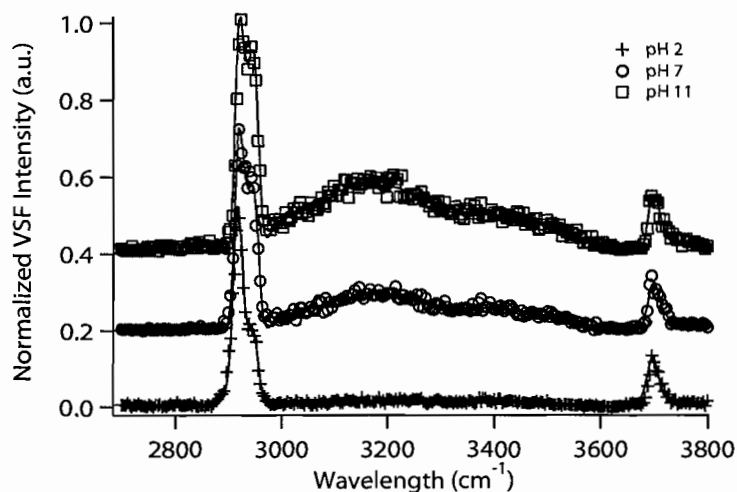


Figure 5.6. VSFS spectra of the FDS/water interface at 0.01 M ionic strength and pH 2, 7 and 11. Solid lines are fits to the data. Spectra are offset for clarity.

intrinsic orientation of H₂O at this interface arises from water sacrificing hydrogen bonds to straddle the monolayer and a small number that penetrate into the chains.

SiO₂/FDS/Water Interface

FDS molecules have a larger van der Waals radius, a buried dipole at that CH₂CF₂ bond and are shorter than ODS, which may lead to greater interactions of H₂O with the SiO₂ substrate and a greater number of orientated water molecules as the electric field calculation at the end of Chapter IV showed. The possibility is studied using the same pH and NaCl titration methods as ODS and SiO₂ to understand the origins of the water signals at this interface and the way FDS interacts with H₂O.

The interfacial behavior of water on FDS coated SiO₂ in buffered pH solutions shows that bulk pH has a significant effect on the water structure, as can be seen in Figure 5.6. There are three main features of this interface, the CH₂(as) stretching

vibrations at 2916 ± 1 and $2955 \pm 2 \text{ cm}^{-1}$, the coordinated OH vibrations from 3000 to 3600 cm^{-1} and the free-OH oscillator at $3694 \pm 2 \text{ cm}^{-1}$. The $\text{CH}_2(\text{as})$ vibrations are unaffected by changes in the bulk pH and are split due to the bonding of one of the CH_2 moieties to the silane group, which shifts its resonant frequency up to 2955 cm^{-1} . Such shifts have previously been seen for methylsilane groups.[95] The free-OH mode is located at 3694 cm^{-1} is also unaffected by changes in the aqueous environment. However, the coordinated water stretching region is strongly affected by solution pH. At high pH, the interface is negatively charged and there is a large signal from the coordinated water molecules near 3200 and 3450 cm^{-1} . This VSFS signal decreases when the solution pH is dropped from from 11 to 7. Because the ionic strength of the solutions remains constant at each of the pH values examined, the charge screening length remains constant and the decrease in VSFS signal is primarily due to decreased interfacial charge. At pH 2 there is much less signal from coordinated H_2O molecules, but results are inconclusive as to whether the interfacial charge is reversed as the as the VSFS signal is nearly flat in the coordinated water region and can be fit by very broad water peaks with phases of π or 0. Measurements of the zeta potential of aqueous FDS interfaces have found the potential to decrease from approximately -60 mV to approximately -30 mV between pH 11 and pH 7.[33, 106]. These same ζ -potential measurements found the potential to be slightly positive at pH 3 for this interface. Based on these measurement, it is assumed that the interfacial charge has transformed from negative to positive at pH 2, just as at ODS. Reducing

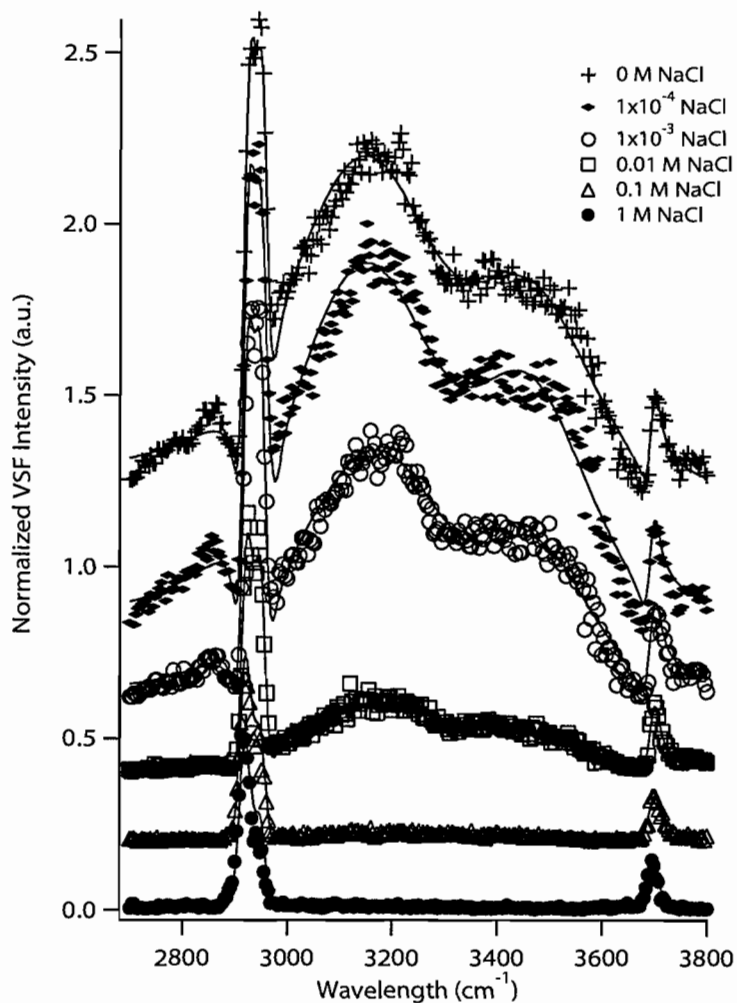


Figure 5.7. VSFS spectra of the FDS/water interface at pH 5.8 with different NaCl concentrations. Solid lines are fits to the data. Spectra are offset for clarity.

the interfacial charge to nearly zero in this experiment shows there is little intrinsic orientation imparted to H_2O by its interaction with FDS.

Ionic strength titrations with NaCl confirm the above conclusion. Addition of a small amount of NaCl ($1 \times 10^{-4}\text{M}$) slightly increases the VSFS signal, as seen in Figure 5.7. This suggests that Cl^- is attracted to this interface, just as with

ODS. However, at 1 mM ionic strength, the added NaCl reduces the VSFS signal in the coordinated water region, indicating that the adsorption process is now being dominated by charge screening. Continuing to add NaCl further reduces the signal to zero at 1 M bulk concentration. That there is no response from coordinated water at 1 M NaCl when the double layer is small, but the interface is slightly positively charged indicates two things. First, FDS causes no intrinsic orientation of water molecules. Second, that the interface charge is reversed at pH 2, as if the charge was zero, there would be no signal from coordinated water molecules.

The results of the two monolayer studies can be used to reinforce each other and look for differences in how the monolayers interact with water. First, the free-OH frequencies are significantly different: $3693 \pm 2 \text{ cm}^{-1}$ at FDS and $3670 \pm 2 \text{ cm}^{-1}$ at ODS. The higher frequency at FDS is close to that of the free-OH at the air/water interface[100] and indicates the interaction between water and fluorocarbons are weaker than with hydrocarbons. The weaker direct interaction with water is further shown by the penetration of water partially into the ODS chains, but not the FDS chains shown by the lack of a peak near 3600 cm^{-1} in the FDS spectra. It can be argued that this peak is due to solvated ions at the ODS/water interface or due to water molecules in the ODS chains. If this peak were due to solvated ions, it is anticipated that it would appear at both monolayer interfaces since both interfaces have an attraction for Cl^- ions and that the location of this peak would be different for solvated phosphate and chloride anions, which have significantly different solvation

energies. The enthalpy of solvation of H_2PO_4^- is -63.8 kJ/mol [164] and Cl^- is -367 kJ/mol ,[165] which should lead to different solvation environments and thus IR frequencies. As the peak is present at only the ODS surface and does not change its spectral position, it is unlikely the resonance is due to solvated ions. The other explanation, water in the ODS monolayer chains seems more plausible. ODS chain orientation was shown to be affected by water in Chapter IV and in molecular dynamics work.[97] A recent molecular dynamics simulation, on the other hand, found that a monolayer of perfluorodecane with a mean molecular area of 28 \AA^2 is barely penetrated by water.[110] Based on the deposition isotherms for the FDS monolayers, the mean molecular area is 26 \AA^2 , a film density that should not be penetrated by water. Thus, it can be concluded that the source of the resonance near 3600 cm^{-1} is due to intrachain water molecules which are buried under the coordinated water peaks being revealed as the interfacial charge is reduced or the ionic strength increased. Finally, the peaks in the 3200 cm^{-1} region have slightly more intensity at the FDS interface than at ODS, indicating that water is either more strongly oriented or more water is oriented at the FDS surface than at ODS. However, the lack of signal at 3050 cm^{-1} due to water molecules hydrogen bonding with the monolayer show that this increase is due to a greater attraction at the FDS surface for H^+ and OH^- ions. Neither interface results in significant coordination of interfacial water molecule by virtue of their direct interactions.

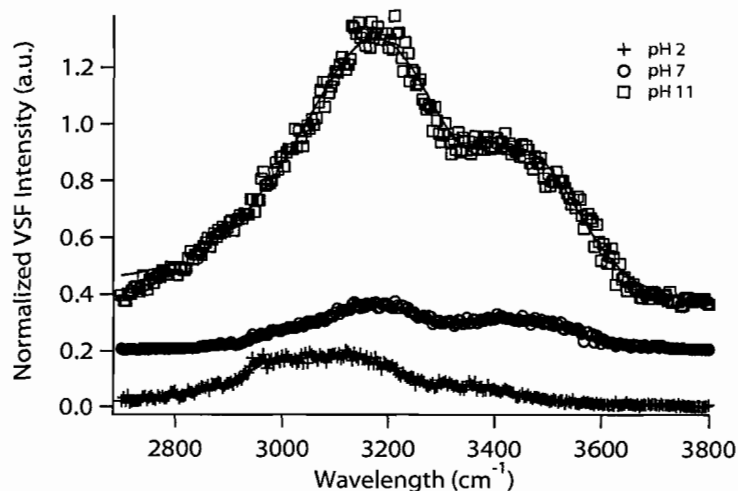


Figure 5.8. VSFS spectra of the Zdol/water interface at selected pH values. The solid lines are fits to the data.

SiO₂/Zdol/Water Interface

The interface of water with Zdol has major differences with those of FDS and ODS monolayers. While the thickness of the coating is similar to the two monolayers (≈ 2 nm), as is the apparent hydrophobicity ($\theta = 109^\circ$), the chemical composition of Zdol is quite different which leads to dramatically different interfacial bonding environments. Silane SAMs are thought to bond to approximately 20% of the available silanols due to their horizontal cross-linking,^[25] whereas Zdol likely bonds to fewer locations given the small number of hydroxyls (2) per chain for condensation. The long polymer chain is also filled with hydrogen bond accepting oxygen atoms which have attractive interactions with water, unlike the two monolayer surfaces. These chemical differences lead to VSFS spectra that are dramatically different from those of the SAMs, as can be clearly seen in Figures 5.8 and 5.9.

Figure 5.8 shows interfacial spectra of a Zdol coating at pH 11, 7 and 2. At high pH, the Zdol/H₂O interface shows the characteristic two lobed spectrum of electrostatically oriented water, indicating a highly negative interfacial charge. A large peak corresponding to strongly coordinated water molecules is apparent near 3200 cm⁻¹ and a smaller peak near 3450 cm⁻¹ originates from the more weakly coordinated species. Decreasing the pH while holding the ion strength constant lowers the surface charge and thus the number of electrostatically oriented interfacial water molecules. This results in the lower intensity of the pH 7 spectrum. However, unlike the two monolayer surfaces, at pH 2 the signal in the coordinated water region does not drop to zero but remains high and appears to redshift from near 3200 cm⁻¹ to near 3100 cm⁻¹. These results indicate that the structure of interfacial hydrogen bonding network is heavily dependant on the interfacial charge.

Whether the differences are due to a changing interfacial speciation due to adsorption of H⁺ ions or the the loss of electrostatically oriented water is investigated by NaCl titration. As shown in the previous sections, the addition of NaCl compresses the double layer and reveals those molecules directly interacting with the solid phase. The results of these experiments are shown in Figure 5.9. The primary feature of these spectra is the strong signal from the coordinated water stretching region. Addition of a small amount of NaCl, 1 × 10⁻⁴ M, increases the VSFS signal slightly and indicates a small attraction to the interface of Cl⁻ just as seen with FDS and ODS. Increasing the ionic strength to 1 mM, reduces the VSFS signal in the 3000-3600 cm⁻¹ region as

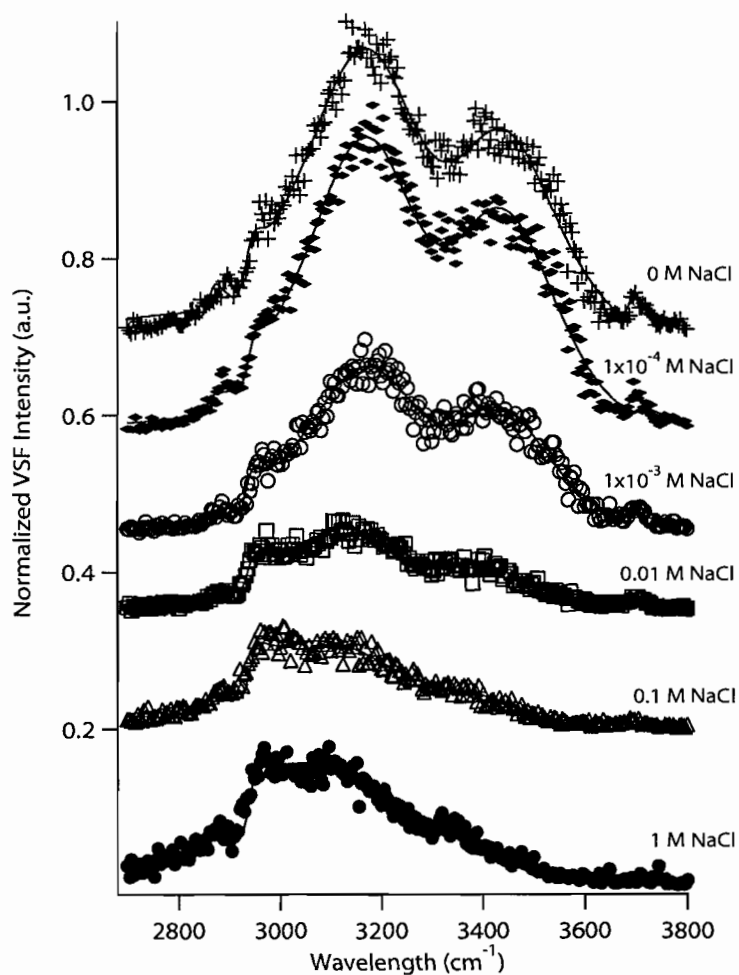


Figure 5.9. VSFS spectra of the Zdol/water interface at pH 5.8 with different NaCl concentrations. The solid lines are fits to the data. The spectra are offset for clarity.

the surface charge is now effectively screened. Adding more NaCl appears to shift the spectral intensity from near 3200 cm^{-1} to 3100 cm^{-1} as the electric double layer thickness becomes very small. The spectrum with 1 M NaCl is qualitatively similar to the pH 2 result in Figure 5.8. This means that the water bonding environment is quite similar at very low surface charge and at high ionic strength.

To understand in detail the behavior of water at the Zdol surface, the spectra were simultaneously analyzed using global fitting. Results of this analysis show that the water region is best described by the same three peak model used for the $\text{SiO}_2/\text{H}_2\text{O}$ interface. The first water peak is out of phase with the other water modes and is located at $3052 \pm 3 \text{ cm}^{-1}$ and represents water molecules directly interacting with protonated silanols on the SiO_2 substrate. The amplitude of this peak does not change with changing ionic strength, only with pH. The second coordinated water peak is located at $3210 \pm 7 \text{ cm}^{-1}$ and represents the more strongly coordinated, electrostatically oriented hydrogen bonded species while the third large water peak is centered at $3430 \pm 8 \text{ cm}^{-1}$ and represents electrostatically oriented hydrogen bonded species in more asymmetric coordination environments. The intensity of both of these peaks decreases with increasing ionic strength.

Similarities between the $\text{SiO}_2/\text{Zdol}/\text{water}$ and $\text{SiO}_2/\text{water}$ interfaces are shown clearly in Figure 5.10, which compares the fit amplitudes of the 3050 cm^{-1} peak and the 3200 cm^{-1} peak for each of these interfaces. The amplitudes of these peaks is nearly identical for each of the solution conditions examined. Figure 5.10(a) shows the fit amplitude of the strongly coordinated electrostatically oriented peak. The amplitude of this peak increases greatly with increasing pH due to the deprotonation of surface silanol groups which increases the interfacial electrostatic field. Holding the pH constant and increasing the ionic strength keeps the surface charge constant and results in a small increase in VSFS amplitude with the addition of Cl^- as it

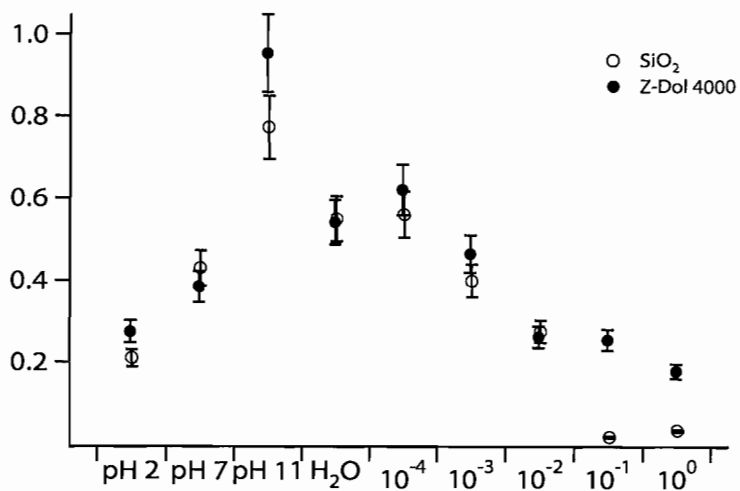
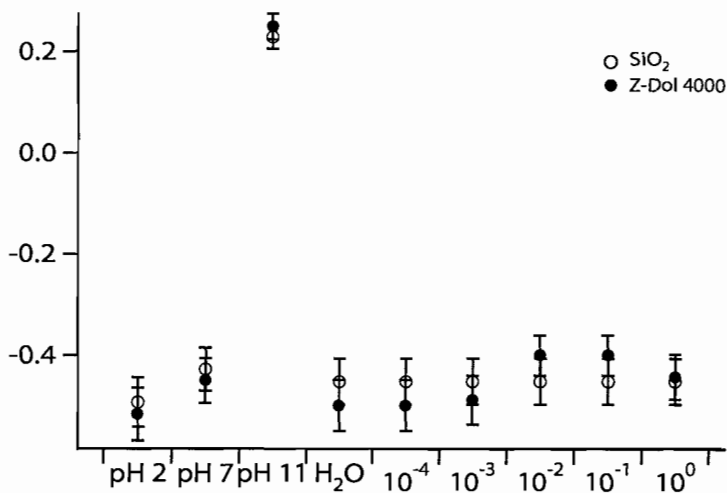
(a) Fit amplitude of $\approx 3200 \text{ cm}^{-1}$ peak(b) Fit amplitude of $\approx 3050 \text{ cm}^{-1}$ peak

Figure 5.10. Nonlinear peak fitting amplitudes of: (a) the 3200 cm^{-1} and (b) the 3050 cm^{-1} peaks used in fitting the SiO_2 and Zdol samples. X-axis shows solution pH values and ionic strengths.

is attracted to the hydrophobic surface, which increases the field. Other than this deviation, the amplitude trend for these field oriented water molecules is identical at both SiO_2 and Zdol interfaces. The similarity of the amplitudes indicates that the surface charge at both surfaces is nearly the same.

Surface charge has a significant effect on the amplitude of the directly interacting peak near 3050 cm^{-1} , as shown in Figure 5.10(b). SiO_2 is largely protonated at pH 7[102] and water molecules hydrogen bond with these protonated surface sites. Decreasing the pH increases the number of protonated silanols and thus the number of molecules hydrogen bonding with the surface, which increases the amplitude of the peak modeling these molecules. At pH 11, the surface is mostly deprotonated and water molecules hydrogen bonding with the surface reverse their orientation, which is shown by the change in sign of the peak from negative to positive. The number of water molecules engaged in hydrogen bonding with the surface stays constant at constant pH, as increasing the ionic strength does not affect these water molecules which are directly interacting with the surface.

The similarity of the fit amplitude of the water peaks at the Zdol interface relative to SiO_2 indicate that these surfaces are nearly identical to water. It is clear that water penetrates the Zdol fully and interacts with the substrate. Thus, water interactions with Zdol are primarily driven by SiO_2 chemistry. Coordination of water at monolayer interfaces is due to the ion attracting behavior of the hydrophobic

surfaces; the only direct interactions are shown by uncoupled OH oscillators and water molecules in alkyl chains.

In addition to the coordinated water peaks, two other features are present in the Zdol spectra: a small positive peak near 3690 cm^{-1} and a dip near 2930 cm^{-1} . From spectral fitting, the location of the small positive peak is $3694 \pm 2\text{ cm}^{-1}$ and the dip is located at $2950 \pm 4\text{ cm}^{-1}$. These peaks are due to free-OH oscillators and the $\text{CH}_2(\text{as})$ stretching vibration of the Zdol molecules themselves. The CH_2 resonance appears shifted because of interference with the coordinated water peaks. The frequency of this CH_2 mode is shifted from the normal $\text{CH}_2(\text{as})$ location near 2915 cm^{-1} because it is bonded directly to silicon. This shift is also seen in FDS monolayers. Because the number of CH_2 groups is quite small, only two per polymer chain, and the chains are likely randomly oriented, the small size of this signal is reasonable. The presence of the free-OH peak indicates that some water molecules are directly interacting with CF_2 domains on the polymer chain. However, the amplitudes of both of these modes decrease with increasing ionic strength. Such decreases are not seen with FDS or ODS monolayers and have been investigated to understand the origin of these changes.

VSFS response is sensitive to both the number of molecules and their orientation; signal decreases can be due to either a decrease in the number of molecules or an change in net orientation. Water is thought to cleave organosilane-substrate bonds[166–168] and if that water penetrates to the substrate, irreversible changes in the coating with exposure to water are expected. Two VSFS experiments were

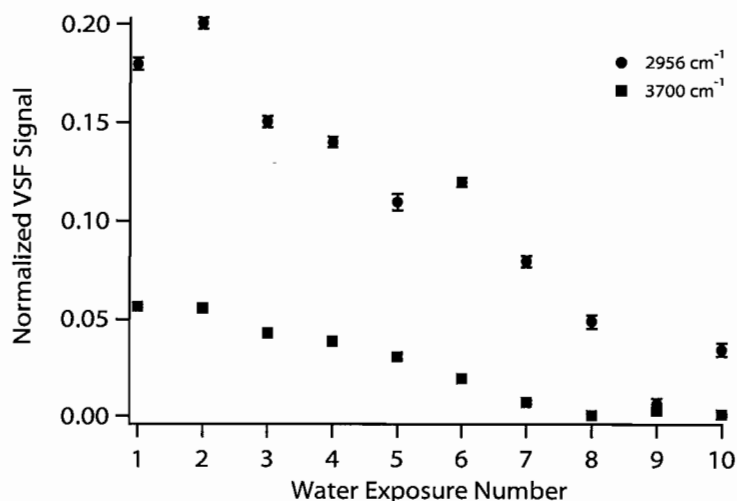


Figure 5.11. Zdol VSFS signal at 3700 cm^{-1} and 2956 cm^{-1} as a function of water exposures. Each data point is the normalized VSFS intensity of 600 pulses.

performed on Zdol films to look at the free-OH and CS stretching region of Zdol to determine the effect of water of the polymer coating. First, if the loss of free-OH intensity is due to swelling induced reorientation, the intensity of the free-OH peak should decrease over time. To examine this possibility, the VSFS intensity at 3700 cm^{-1} was monitored over several hours on a freshly prepared Zdol surfaces. The VSFS signal was found to be unaffected by sitting in water for a prolonged period. This indicates that the effect is not due to polymer reorientation. The CH signal is not a desirable signal to monitor for this as the CH_2 groups are conformationally locked at the bottom of the polymer chain by their bonds to the substrate.

Second, the effects of rinsing the Zdol surfaces with water were tested. If Zdol leaves the surface after repeated rinsing, the surface will restructure and this may reduce the number of CF_2 groups for water to directly interact with, reducing the free-

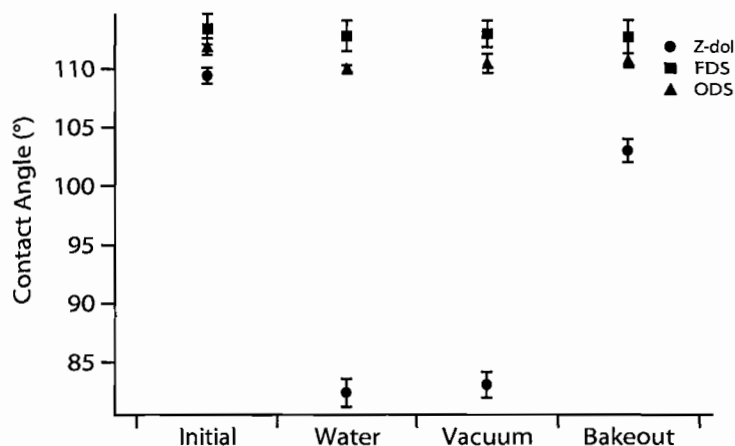


Figure 5.12. Water contact angle of Zdol (●), FDS (■) and ODS (▲) before soaking experiments, after experiments, after overnight in vacuum and after 1 hour bakeout at 110°C. The water contact angle of Zdol is largely recovered after heating.

OH. Removal of polymer will also reduce the number of CH₂ groups at the interface, thus reducing the VSFS amplitude of this mode. To test this effect, a drop of water was placed on a Zdol sample and allowed to equilibrate for 5 minutes after which the VSFS signal at 3700 cm⁻¹ was collected for 1 minute. Following this, the drop was aspirated off and a new drop of water placed in the same location and the procedure repeated. Prior to each drop, VSFS signal was collected at 2956 cm⁻¹ where the CH signal of “dry” Zdol is maximized. The results of these experiments are shown in Figure 5.11. The results show a clear decrease in VSFS response from both the free-OH and CH₂(as) with the number of water exposures. The decrease in CH₂ signal indicates the removal of Zdol from the surface. The loss of free-OH intensity shows that the surface is either becoming more rough due to swelling with water and/or that there are fewer hydrophobic groups on the surface for water to interact with.

If water is perturbing the structure and Zdol and permanently altering the film, then some effect of this should be seen in water contact angle analysis. As Zdol leaves the surface, there will be more exposed SiO_2 which will decrease the contact angle. Results of these contact angle experiments are shown in Figure 5.12. Prior to soaking a Zdol sample in water three times, the water contact angle of Zdol was 109.3° . After soaking the sample in water, the contact angle falls to 82.4° , indicating large changes in the Zdol surface. If this decrease in hydrophobicity is due to a thin surface bound water layer on the top of the Zdol coating, it should readily come off after gentle drying; however, even sitting overnight in a vacuum desiccator cabinet after repeated pump purge cycles left the contact angle unchanged, which means that water is tightly held inside the Zdol layer. To remove this water, the sample was baked at 110°C for 1 hour. This results in a significant recovery of the initial static contact angle to 103° ; additional heating had no effect on the contact angle. That the contact angle does not recover fully indicates that some changes to the sample are permanent, and a portion of Zdol is removed by rinsing. These findings corroborate the VSFS conclusions that water fully permeates Zdol over time and that rinsing removes excess or loosely bound Zdol from the surface. For comparison, ODS and FDS coated samples were exposed to the same set of conditions, but their contact angles were unaffected showing that water does not penetrate to the SiO_2 substrate on the timescales investigated here.

To verify that the Zdol surface restructures after water exposure, the Zdol surface was studied before and after water exposure and bakeout using AFM. Figure 5.13

entire Zdol coating and remains there, as seen by the changes in the water contact angle of the Zdol coating before and after prolonged water exposure. These water molecules primarily interact with the negatively charged SiO_2 substrate, giving rise to the directly interacting water feature near 3050 cm^{-1} in the VSFS spectra, which is affected by pH, but not by ionic strength. These directly interacting species do not readily leave the surface, but remains within the polymer coating until they are thermally evaporated out, resulting in a large contact angle increase. However, a portion of the Zdol is removed from the surface by water as evidenced the partial contact angle recovery. In addition to cleaving the surface bonded linkages of Zdol, some Zdol degradation may be due to the disproportionation reaction of the polymer with acid protons in the water or Lewis acid sites on the substrate; these reaction products can then react with water to form fluorinated carboxylic acids. This type degradation mechanism has been found on Zdol coated magnetic discs[127] and other studies have shown that water can penetrate Zdol surfaces and redistribute them,[7, 132] confirming the results here.

Conclusion

Interactions of water with fluorocarbon, hydrocarbon and Zdol coatings have been studied by VSFS, contact angle and AFM to elucidate the effect of surface functionality on interfacial water bonding environments. Signatures of the direct interactions between water at these coatings have been determined using pH and

ionic strength titrations. For comparison purposes, the $\text{SiO}_2/\text{H}_2\text{O}$ interface was first studied to develop a picture of the different possible bonding environments and to understand the effect the substrate has on interfacial water structure. These VSFS studies have validated the recent picture of the $\text{SiO}_2/\text{H}_2\text{O}$ interface proposed by Ostroverkhov et al.,[153] in which water molecules participating in hydrogen bonding interactions with SiO_2 have a unique spectral signature. At pH values below the second pK_a of SiO_2 , a large portion of the surface is protonated. Water molecules interact with these SiOH species through direct hydrogen bonding interactions, which causes their dipoles to be opposite those species interacting electrostatically to the net negatively charged interface. These molecules are redshifted by $\approx 150 \text{ cm}^{-1}$ from the location of the water molecules affected by the interfacial electrostatic field and provide the first signature of directly interacting water molecules.

This signature is not present in the monolayer/water systems, indicating that the substrate is effectively masked by the silane monolayers investigated. Oriented interfacial water molecules arise from the adsorption of ions at the monolayer surfaces which creates an electrostatic field and causes dipolar alignment of water molecules. The principle signature of the direct interactions between water and hydrophobic SAMs is the free-OH peak, which arises from water molecules straddling the interface and sacrificing a hydrogen bond to minimize their net interactions. This peak is located at 3693 cm^{-1} at the FDS/ H_2O interface and at 3672 cm^{-1} at the ODS/ H_2O interface. The blueshift of this frequency at FDS is indicative of the weaker

interactions between fluorocarbons and water compared to hydrocarbons. Further evidence of this weaker interaction was found by the lack of penetration of water into the FDS monolayer. Water molecules do become enmeshed in the alkyl chains of ODS and have a unique spectroscopic signature near 3600 cm^{-1} .

Penetration into the hydrophobic coating is much more significant in Zdol coatings than ODS. At this interface, despite its great initial hydrophobicity, water readily permeates the coating and accesses the SiO_2 substrate. This gives rise to water molecules that have the same characteristics as those at the $\text{SiO}_2/\text{H}_2\text{O}$ interface and are unaffected by charge screening, only the protonation and deprotonation reactions of silanols. This confirms the picture that for an impermeable coating, such as ODS or FDS, the water coordination is driven by electrostatics and not direct interactions.

Zdol coatings do have some hydrophobic direct interactions as indicated by the free-OH peak. These hydrophobic interactions are minimized as Zdol swells with water and its hydrophobicity decreases. To remove water trapped in the polymer:substrate system requires heating, which shows there are strong hydrogen bonding interactions in the SiO_2 :Zdol system. This relatively rapid penetration of the polymer by water destabilizes and degrades the coating. If water were able to readily penetrate through the FDS or ODS monolayers to the substrate, similar degradation of the monolayers would be observed.

CHAPTER VI
FLUOROCARBON AND HYDROCARBON MONOLAYER INTERACTIONS
WITH METHANOL

Clear differences in the interactions of water with hydrocarbon and fluorocarbon monolayers were found in Chapter V. These include a 20 cm^{-1} frequency difference between the free-OH oscillator of straddling water molecules at the fluorocarbon and hydrocarbon interface and the penetration of water into the hydrocarbon monolayer. Having seen that there are significant differences in the ways the two functionalities interact with water, the next step is to see how the lipophobic nature of FDS affects organic adsorption. The simplest molecule to investigate the adsorption of at fluorocarbon and hydrocarbon monolayer surfaces is methanol. The experiments within this chapter show that methanol is strongly preferred over water at the FDS interface and its orientation is bulk concentration independent. Based on this, the adsorption isotherm is constructed and compared to methanol adsorption isotherms at other surfaces. The results of this comparison show that methanol behaves similarly at different hydrophobic interfaces; the adsorption behavior is explained by a dimer adsorption model. Finally, these studies show a spectroscopically distinct vibrational resonance for methanol at both FDS and ODS monolayers with a clear frequency difference between the mode at the two surfaces investigated.

Introduction

Numerous industrial and chemical processes utilize small chain alcohol:water solutions; in processes ranging from cleaning to electrochemistry, the interfacial behavior of aqueous alcohol solutions plays a critical role.[49, 169–173] Furthermore, small organic molecules are ubiquitous in the environment and are known to cause degradation of lubricant films in microelectromechanical applications.[6, 174] Given these applications and the importance of fluorocarbons in devices, understanding the interactions of small alcohols at the interface with FDS monolayers is a matter of both fundamental and practical import. The differences observed in the interfacial behavior of water at ODS and FDS interfaces, in terms of the frequency of the free-OH mode and the degree of water structuring point to key differences in the interactions of fluorocarbons and hydrocarbons with adsorbates. Determining how the unique chemical properties of fluorocarbons manifest themselves during organic adsorption is the principle concern of both this and the following chapter.

Methanol is an ideal molecule to probe differences in the effects of fluorocarbon and hydrocarbon surfaces on molecular adsorption. First, the molecule is spectroscopically simple compared to long chain alcohols and surfactant molecules because it has only three C-H vibrational modes present in the spectrally accessible window. The primary mode originates from the $\text{CH}_3(\text{ss})$ and is redshifted by around 40 cm^{-1} to near 2836 cm^{-1} from the the typical $\text{CH}_3(\text{ss})$ stretching value ($\approx 2876\text{ cm}^{-1}$) due to

the electron withdrawing C-O bond. This spectrally distinct peak is partially freed from interference with the monolayer modes making interpretation easier and spectral fitting more accurate. Second, methanol is electrically neutral. The previous chapters showed that interfacial charge has a large effect on the spectra of interfacial water molecules at both FDS and ODS surfaces, due to differences in interfacial electrostatic fields. Adsorption of uncharged methanol molecules will be relatively unaffected by the interfacial electrostatic field. Finally, fluorocarbons have long been known to be both lipophobic and hydrophobic. Because methanol lacks a long aliphatic carbon chain that will associate with other aliphatic chains via van der Waals interactions, as has been seen for dodecanol at octadecane thiol monolayers,[175] the degree to which of the two effects, lipophobicity or hydrophobicity, dominates the interaction with the fluorocarbon surface may be determined.

Experimental

VSFS experiments were performed as described in Chapter III. Each spectrum shown in an average of 3 individual spectra collected at 20 shots per data point with a resolution of 2 cm^{-1} or 5 cm^{-1} for the CH stretching region and OH stretching region studies, respectively. The spectra are in the SSP polarization scheme unless otherwise noted. All spectra were background corrected and then normalized for IR energy. Final spectral normalization was carried out using the IR transmission spectrum of the prism and monolayer sample.

FDS samples were deposited via the Langmuir-Blodgett method at a surface pressure of 15 mN/m. Hydrocarbon monolayers were deposited as described in Chapter III with a deposition time of 8 hours. Samples were characterized using the home built goniometer and AFM measurements were made as described in Chapter III. Reported contact angles are averages of 5 individual measurements.

Three different methanols were used in these experiments: CH₃OH (Burdick and Jackson), CH₃OD (Aldrich) and CD₃OD (Cambridge Isotopes). Solutions of CH₃OH/H₂O were used for VSFS studies including the OH stretching region. CH₃OD/D₂O solutions were used for CH stretching region experiments because substituting OD for OH reduces the interferences with coordinated water stretching vibrations. Both types of solutions were made by mass to account for changes in volume due to the mixing of the two liquids. The solution concentrations are measured in mole fraction of methanol and denoted by χ .

Results and Discussion

Fluorocarbon SAM/Methanol Interface: OH Region

Spectra of the neat FDS/H₂O and FDS/CH₃OH interfaces are shown in Figure 6.1. The narrow feature in the water spectrum near 2930 cm⁻¹ is due to the CH₂ groups in the FDS monolayer. The broad features that dominate the spectrum in the region from 3000 to 3600 cm⁻¹ originate from electrostatically oriented water molecules in higher and lower coordination environments, as has been discussed in earlier chapters.

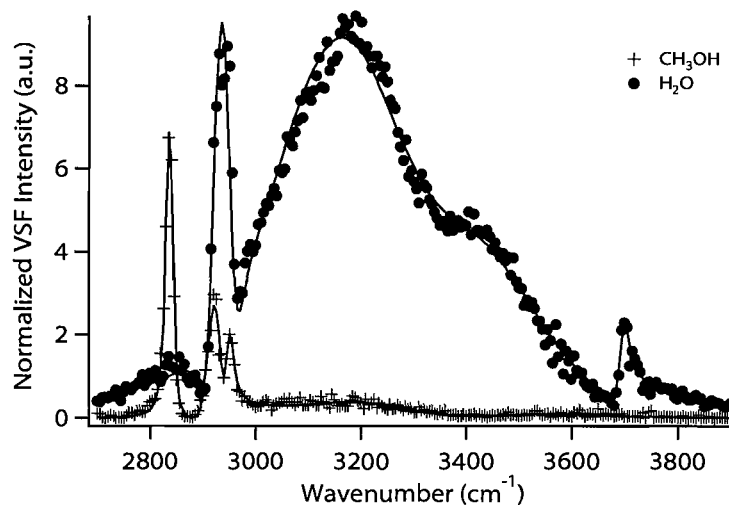


Figure 6.1. VSFS spectra of the neat $\text{CH}_3\text{OH}/\text{FDS}$ and $\text{H}_2\text{O}/\text{FDS}$ interfaces.

There is also the characteristic peak at 3694 cm^{-1} that is seen in all $\text{FDS}/\text{H}_2\text{O}$ spectra arising from vibrationally decoupled OH oscillators of water molecules pointing into the FDS monolayer. The $\text{FDS}/\text{CH}_3\text{OH}$ spectrum has three narrow peaks below 3000 cm^{-1} corresponding to the CH stretching modes of the FDS monolayer and CH_3OH . The methyl symmetric stretch is spectrally distinct from the two monolayer modes and is located at 2838 cm^{-1} . There is also a low, broad feature centered around 3050 cm^{-1} due to $\text{CH}_3\text{OH}\cdots\text{CH}_3\text{OH}$ hydrogen bonding. From these two spectra, it is clear that methanol is adsorbed at the interface with the CH_3 moiety, not the OH group, oriented towards the monolayer. If the OH of methanol were directed into the monolayer, there would be a narrow OH stretching vibration due to this oscillator above 3600 cm^{-1} . Further conclusions regarding the distinct regions of the spectra require more careful investigations of each spectral region. First the OH stretching

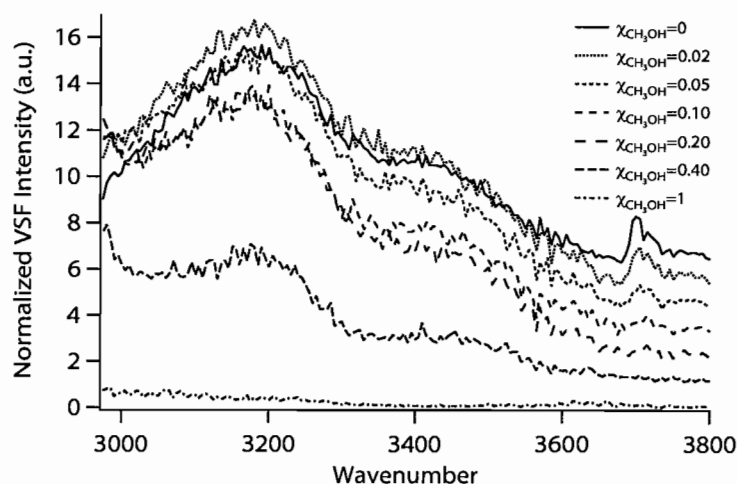


Figure 6.2. VSFS of the FDS/ $\text{CH}_3\text{OH}:\text{H}_2\text{O}$ solution interface. The spectra are offset for clarity.

region from 3000 cm^{-1} to 3800 cm^{-1} will be discussed and then the CH stretching region from 2700 cm^{-1} to 3100 cm^{-1} .

To better understand the changes in the OH stretching region, between pure water and pure methanol, spectra were collected at several intermediate concentrations of methanol. Selected spectra from these experiments are showing in Figure 6.2. The addition of CH_3OH to H_2O has significant effects on the interfacial water structure as seen by the changes in the coordinated water region and the loss of the free-OH. Fitting these spectra in the coordinated water stretching region is possible, but not obviously meaningful due to the wide array of possible spectral fits. At low concentrations of methanol, less than $\chi=0.1$, the amplitude of the VSFS signal increases near 3200 cm^{-1} . This suggests that small amounts of methanol increase the degree of intermolecular hydrogen bonding, possibly as the molecules adsorb to the

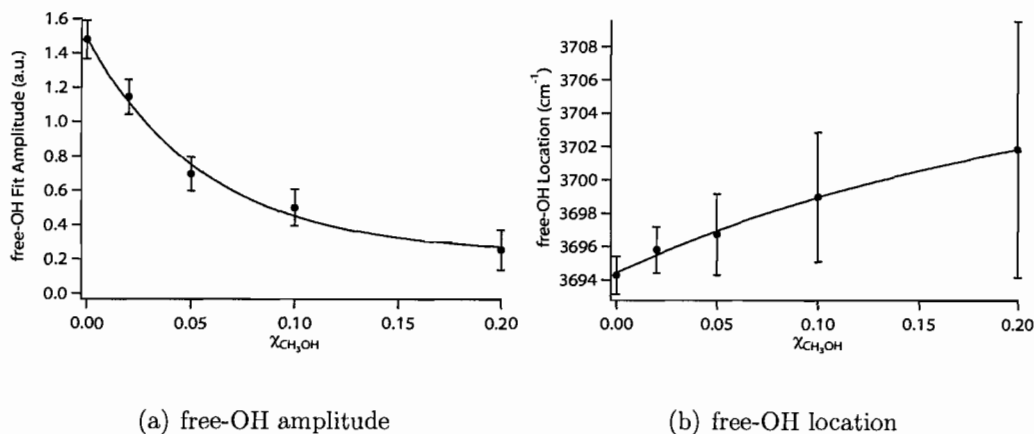


Figure 6.3. Fit (a) amplitude and (b) location of the free-OH peak at different molar percentages of CH_3OH . The solid lines are guides to the eye.

interface and displace straddling water molecules. These straddling molecules are then no longer directly interacting with the FDS monolayer and now form more hydrogen bonds, increasing the number of molecules in this spectral region and thus the VSFS signal. Increasing the bulk concentration of methanol above 10 percent decreases the signal in the coordinated water bonding region, indicating that sufficient methanol is now present at the interface to disrupt the network, either directly or by decreasing the interfacial potential.

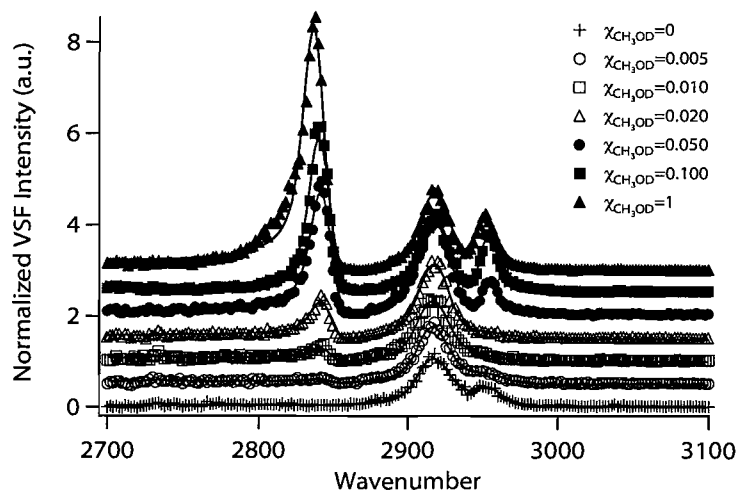
Insight in the displacement of interfacial water molecules can be attained by examination of the free-OH peak, the intensity of which can be assumed to be directly proportional to the number of straddling water molecules. As shown in Figure 6.3(a), the amplitude of the free-OH decreases with increasing methanol concentration. Above $\chi=0.2$, the free-OH peak is no longer distinct from the background indicating that all of the straddling water molecules have been displaced from the interfaces.

Accompanying the displacement of water molecules from the monolayer surface is a frequency shift of these uncoupled OH oscillators, shown in Figure 6.3(b). The free-OH undergoes a small frequency blueshift from 3694 cm^{-1} to 3701 cm^{-1} as methanol displaces water molecules from the interface. A similar frequency shift, has been observed for free-OH modes at the ODS/ $\text{H}_2\text{O}:\text{CH}_3\text{OH}$ interface[92] and is most likely due to the increasingly hydrophobic environment around the water molecules which straddle the interface.

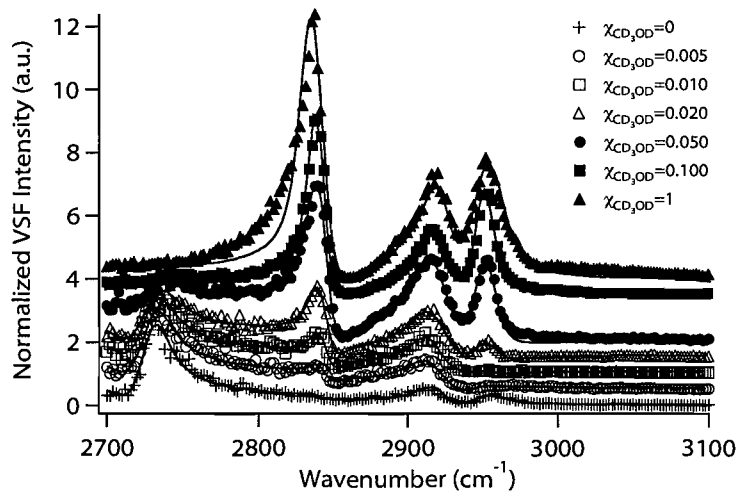
Fluorocarbon SAM/Methanol Interface: CH Region

To generate a complete picture of the behavior of methanol on FDS, the CH stretching region has also been analyzed. This was done using solutions of partially deuterated methanol, CH_3OD in D_2O . This shifts the broad resonance of the O-D coordinated hydrogen bonding, seen in Figure 6.1 out of the spectral window, freeing the data from this interference.

Selected VSFS spectra of the FDS/ $\text{CH}_3\text{OD}:\text{D}_2\text{O}$ system are shown in Figure 6.4 in both SSP and PPP polarization schemes. The monolayer/ D_2O spectrum in Figure 6.4(a) show the distinct CH features of the FDS monolayer. Adding a small amount of methanol to $\chi = 0.005$ has almost no effect on the spectrum, but increasing the concentration to $\chi = 0.010$ results in a small peak near 2840 cm^{-1} due to the methanol. Increasing the concentration further increases the amplitude of this feature. The first monolayer peak at near 2920 cm^{-1} appears to increase in strength with added methanol. The second monolayer peak near 2950 cm^{-1} seems to decrease with the



(a) SSP



(b) PPP

Figure 6.4. SSP (a) and PPP (b) polarized VSFS spectra of $\text{CH}_3\text{OD}:\text{D}_2\text{O}/\text{FDS}$ interface at several mole fractions of CH_3OD (χ). The spectra are fit to three resonances, one pure CH_3 peak and two $\text{CH}_2:\text{CH}_3$ stretches from the monolayer and CH_3OD combined. The spectra are offset for clarity.

addition of CH_3OD through $\chi = 0.020$, and after this mole fraction is reached the peak reappears.

The PPP spectra in Figure 6.4(b) show the same trends as the SSP data; however, there are an additional two peaks. The first of these peaks is the narrow mode at $2727 \pm 2 \text{ cm}^{-1}$ from free-OD oscillators, which are analogous to the previously discussed free-OH groups. The second peak that is present is actually the tailing of the coordinated OD stretching vibrations which occur outside the spectral window. These peaks are much stronger in the PPP spectra than in the SSP spectra because this polarization scheme samples all the elements of $\chi^{(2)}$, as shown in Equation II.7, which results in the increased signal. The methanol peak near 2840 cm^{-1} initially appears as a dip in the $\chi = 0.005$ spectrum and becomes a positive peak as more methanol is added. The free-OD peak disappears with increasing methanol concentration and is no longer present after $\chi = 0.200$, just as in the water stretching region spectra shown in Figure 6.2. The monolayer modes appear as small features near 2920 cm^{-1} and 2950 cm^{-1} and have the same complicated behavior as in the SSP spectra.

The complicated behavior of the monolayer stretching peaks is due to additional vibrational modes of methanol overlapping with the monolayer modes, not changes in the monolayer CH structure. This was verified by comparing spectra of the FDS/ D_2O and FDS/ CD_3OD interfaces in Figure 6.5. These results show that the presence of methanol does not significantly affect the structure of FDS monolayer because the intensity distribution does not change between the two liquids. The

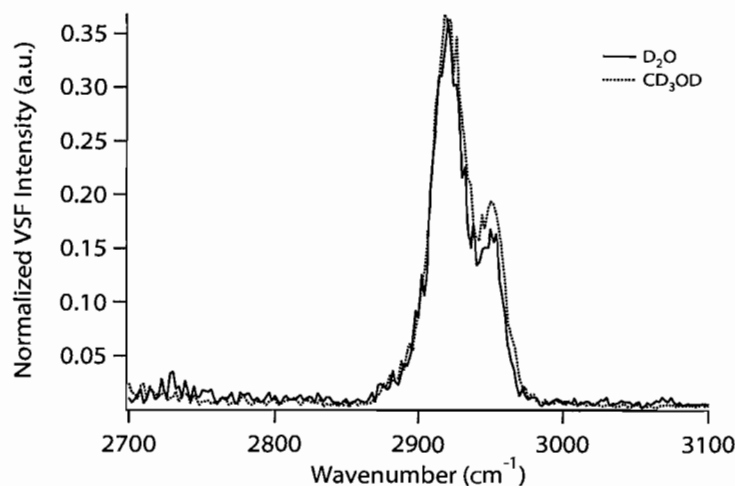


Figure 6.5. VSFS spectra of the CH₂ stretching region of FDS in D₂O and CD₃OD. These spectra are scaled to the same value at 2916 cm⁻¹.

absolute intensity of the monolayer modes is affected by the solvent change, this is most likely due to differences in the refractive indices of the two liquids. Liquid methanol is known to have three peaks in the CH stretching region at 2830 cm⁻¹, 2915 cm⁻¹ and 2940 cm⁻¹ due to Fermi resonance interactions of the CH₃(ss) with two bending overtones.[176–178] The main peak with the most CH₃(ss) character is located at 2830 cm⁻¹ while the other two resonances are principally overtones that interfere with the CH₂(as) stretches of the FDS monolayer.

Spectral fitting was used to deconvolve the SSP and PPP spectra into three CH vibrational modes. While there are a total of five CH vibrations present in the spectra, fitting with three peaks simplifies analysis and has no effect on the parameters of the CH₃(ss) near 2840 cm⁻¹ because of the large (≈ 75 cm⁻¹) separation between this vibrational mode and the center frequencies of the other modes. The two

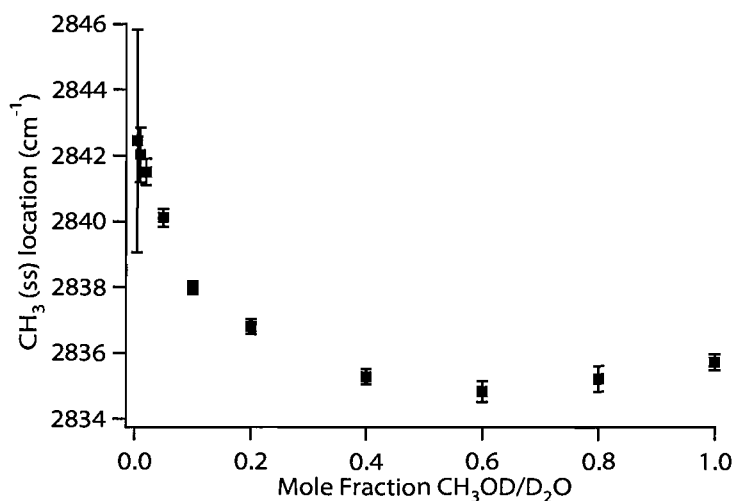


Figure 6.6. Peak location of the CH₃(ss) at the FDS interface as a function of solution composition from spectral fitting.

monolayer modes are located at $2918 \pm 1 \text{ cm}^{-1}$ and $2955 \pm 2 \text{ cm}^{-1}$ with widths of 11 and 9 cm^{-1} based on the FDS/D₂O spectra. These modes were then combined with the two overtone Fermi resonance peaks of methanol. This approach also avoids the requirement of fitting the amplitudes of the monolayer peaks in each spectrum since the changing solution composition alters the Fresnel factors and thus the intensity of these modes. The average locations of the three fit peaks are 2842 ± 3 , 2921 ± 1 and 2952 ± 3 .

Close examination of the spectra and the fitting results shows that the center frequency of the CH₃(ss) is not static, but shifts to lower frequencies with increasing concentration before stabilizing near 40 mole percent. Figure 6.6 shows this trend; the error bars are the errors from the spectral deconvolution. Similar frequency shifts have been observed in bulk CH₃OH:H₂O solutions and at the solution/vapor

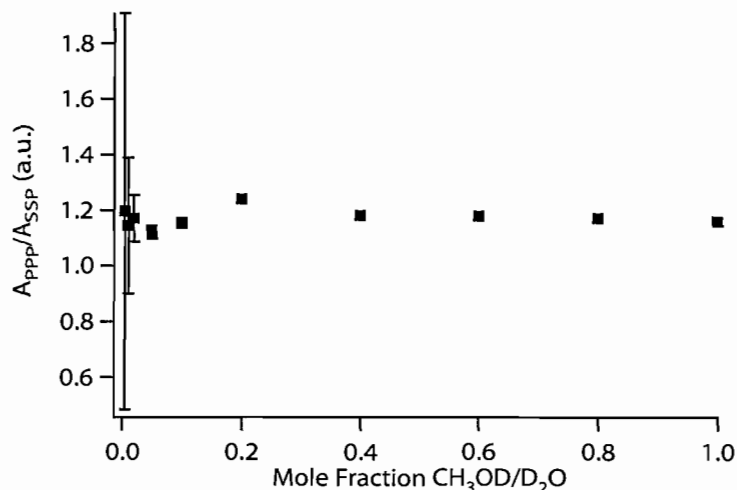


Figure 6.8. Fit amplitude ratio of the $\text{CH}_3(\text{ss})$ peak in the PPP (A_{PPP}) and SSP (A_{SSP}) polarizations at the FDS surface.

Waals forces. The low energy fluorocarbon surface does not have the same degree of attractive interactions with the methyl group resulting in a blueshift of the $\text{CH}_3(\text{ss})$ frequency relative to bulk methanol. In fact, the interfacial methanol frequency at the FDS monolayer surface is nearly the same as that measured for the methanol/air interface,[180] which also lacks attractive interactions between CH_3 groups and other hydrocarbons. This is a clear indication of a weaker interfacial interaction between fluorocarbons and hydrocarbons, just as seen with the free-OH peak of water.

The shifting peak frequency indicates changes in the bonding environment of methanol, which may lead to different molecular orientations as the concentration increases. To investigate this, the ratio of the fit amplitudes of the $\text{CH}_3(\text{ss})$ peak in PPP and SSP polarizations can be examined. Figure 6.8 shows that this ratio is constant across the entire range of concentrations examined and indicates that

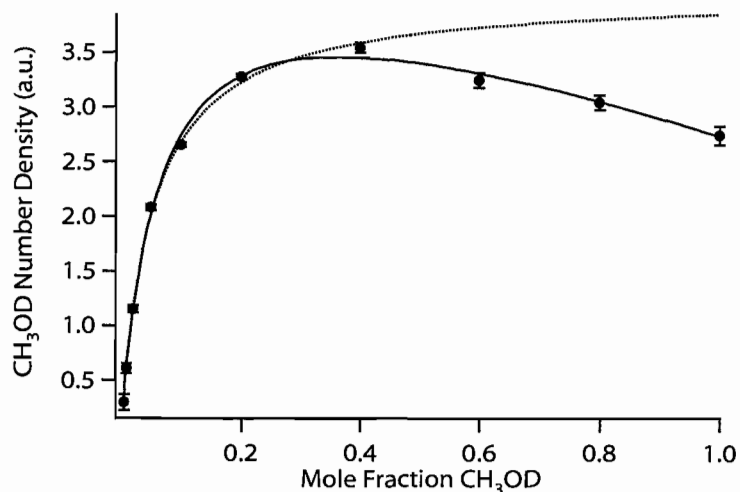


Figure 6.9. Methanol adsorption isotherm on the FDS surface. The solid line is a fit to a two layer adsorption model and the dotted line corresponds to a single Langmuir adsorption isotherm.

methanol adsorbs to the FDS interface with a constant orientation. Unlike long chain alcohols or surfactants that change structure with solution concentration when adsorbing on hydrophobic solids,[149, 151, 175, 184] the small methanol molecules do not experience strong interchain attractions that cause reorientation. Molecular orientation calculations confirming that methanol adsorbs to the FDS interface with a constant angle are in Appendix I. Because the orientation of methanol does not change with concentration, the number of methanol molecules at the interface is directly proportional to the amplitude of the CH₃(ss) peak; thus the amplitude is a measure of the *effective* surface number density. This surface adsorption isotherm is plotted in Figure 6.9. Methanol readily adsorbs to the surface of FDS and the number density increases rapidly to a maximum near $\chi = 0.400$. The apparent surface number density decreases above this concentration.

Two studies at the solution/vapor interface have proposed that the in the number density is due to orientation changes;[60, 180] however, the results in this chapter show that there is no orientation change. It is also possible that changes in hydrogen bonding configuration as the concentration of methanol increase alter the molecular hyperpolarizability,[60] making the amplitude ratio an invalid means for showing changes in orientation. Investigating this possibility requires calculating the hyperpolarizability using computational methods, which is outside the range of this report. A final possibility is that as the concentration of methanol exceeds 40 mole percent, methanol adsorbs in a second layer of opposite, albeit weaker, polar orientation, as has been recently suggested.[145] The VSFS signal from this second layer partially cancels out the signal from the first layer, leading to a drop in the signal. This cancellation has been seen to occur at the interfaces of several small alcohols with SiO₂. [185] To explore this possibility, the adsorption isotherm is modeled using both a single and double layer Langmuir isotherm.

The Langmuir adsorption isotherm is given by the following equation, which can be found in any general surface physical chemistry text:[113]

$$N_{s,eff} = N_{s,max} \frac{k\chi}{1 - \chi + k\chi} \quad (\text{VI.1})$$

where $N_{s,eff}$ is the effective surface number density, $N_{s,max}$ is the maximum surface coverage, k is the adsorption equilibrium constant and χ is the bulk methanol mole fraction. The equation deviates from the standard Langmuir model which has a denominator $1 + k\chi$ because for the high bulk concentrations used here, the

approximation of adsorption from dilute solutions is no longer valid.[186] A fit to Equation VI.1 is shown in Figure 6.9. This model describes the data well to the signal max at $\chi = 0.400$, but does not account for the signal decrease at higher concentration. If a second layer adsorbing with its CH_3 transition dipole moments partially anti-parallel to the first layer, then a double layer adsorption model should explain the data. The derivation of the double layer model follows that in Chen *et al.*[187] In this model, the adsorbed second layer gradually forms an anti-parallel structure with the first layer of methanol, contributing negatively to the VSFS signal. In this case, $N_{s,eff}$ can be written as:

$$N_{s,eff} = N_{s,max}(\Theta - p\sigma) \quad (\text{VI.2})$$

in which Θ is the coverage of the first layer and σ is the second layer coverage; p is an efficiency factor that indicates the degree to which the second layer affects the signal from the first and has values between -1 and 1. A negative p corresponds to constructive interference between the two layers, while $p > 0$ indicates destructive interference. $N_{s,max}$ is now the effective surface density of the full first layer of coverage. Each of these layers, Θ and σ can then be modeled using a Langmuir isotherm as shown below, with adsorption equilibrium constants k_1 and k_2 .

$$\Theta = \frac{k_1\chi}{1 - \chi + k_1\chi} \quad (\text{VI.3})$$

$$\sigma = \frac{k_2\chi}{1 - \chi + k_2\chi} \quad (\text{VI.4})$$

Substituting equation VI.3 and equation VI.4 into equation VI.2 results in the new two layer adsorption model, shown below.

$$N_{s,eff} = N_{s,max} \left(\frac{k_1\chi}{1 - \chi + k_1\chi} \right) \left(1 - \frac{k_2\chi}{1 - \chi + k_2\chi} \right) \quad (\text{VI.5})$$

Equation VI.5 fits the isotherm data quite well across the entire concentration range. From the equilibrium constants, the free energy of adsorption is readily calculated from $\Delta G^\circ = -RT \ln(k_{eq})$ as -1.66 ± 0.07 kcal/mole for the first layer and -0.17 ± 0.14 kcal/mol for the second layer. The energy for the first layer corresponds well with free energies of methanol adsorption calculated at the air/water[145] and ODS/water[92] interfaces, which range from ≈ -1.6 to -2.1 kcal/mol. The adsorption energy of the second layer is near zero, indicating that after the FDS surface is initially covered the interactions of the second layer of methanol with the first layer are similar to those in bulk and that the FDS surface is no longer felt energetically.

To summarize these results on FDS surfaces, methanol adsorbs rapidly to the interface displacing the more polar water molecules. The disappearance of the free-OH peak corresponds with the maximum amplitude of the $\text{CH}_3(\text{ss})$ peak, indicating that methanol has fully displaced the straddling water molecules. The straddling interfacial water molecules are displaced in direct proportion by methanol adsorption, as shown in Figure 6.10. As methanol is added to the interface, the frequencies of the free-OH and $\text{CH}_3(\text{ss})$ peaks shift, due to the changing nature of the hydrogen bonding interactions and interfacial structures. Above 40 mole percent, the free-OH resonance is no longer present and the frequency of the $\text{CH}_3(\text{ss})$ no longer changes;

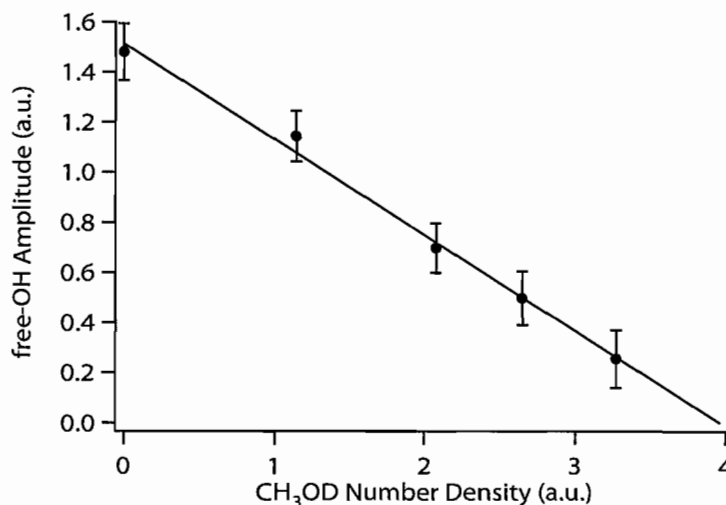


Figure 6.10. The fit amplitude of the free-OH mode versus the effective surface number density of CH₃OH. The solid line is a linear fit to the data.

a additional indicator of the complete displacement of water from the FDS surface. After the first layer is adsorbed, additional ordered adsorption occurs at the interface in an anti-parallel orientation, but the ordering of this layer is weaker than the first layer and the free energy gained by adsorbing the second layer is negligible.

Hydrocarbon SAM/Methanol Interface

In light of the surprising results showing a significant frequency difference between methanol at FDS and bulk methanol, adsorption was studied on ODS to test the hypothesis that weaker van der Waals interactions shift the frequency of interfacial methanol molecules. Methanol adsorption on ODS monolayers has recently been studied,[92] so this analysis serves to verify the literature report and the findings in the previous section. The spectra of CH₃OD:D₂O solutions on ODS in Figure 6.11 are qualitatively similar to those reported in the literature. Increasing the concentration

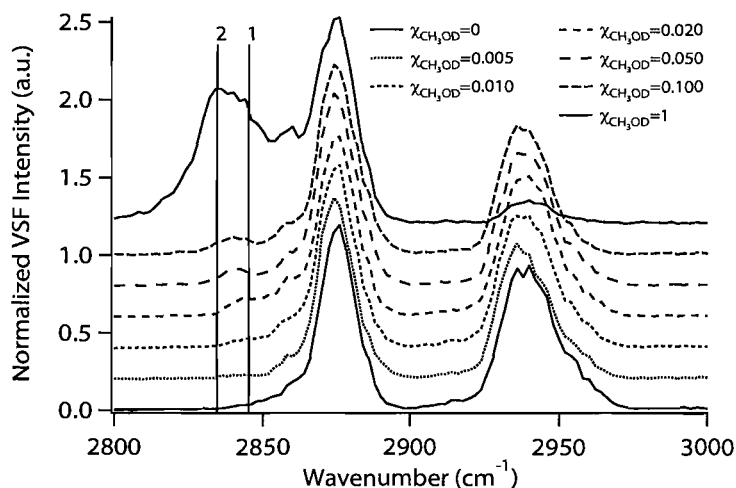


Figure 6.11. VSFS spectra of $\text{CH}_3\text{OD}:\text{D}_2\text{O}/\text{ODS}$ interface at several mole fractions of CH_3OD (χ). The spectra are offset for clarity.

of methanol in the bulk solution appears to shift the frequency of the methanol peak from location 1 to location 2, near 2830 cm^{-1} . Additionally, the $\text{CH}_3(\text{ss})$ of methanol appears to reach maximum intensity near 60 mole percent, which is similar to the literature results, although it is higher than the measurements previously discussed at the FDS interface.

For analytical simplicity in Liu et al.,[92] the authors assumed only two peaks for their spectral analysis, the $\text{CH}_3(\text{ss})$ of methanol near 2830 cm^{-1} and of the monolayer at 2873 cm^{-1} . This works well if the peaks due to the monolayer are unchanged throughout the experiment or the adsorbate peak is free from interference from the ODS layer. However, neither of these points holds for the ODS/methanol system shown in Figure 6.11.

Figure 6.12 contains VSFS spectra of an ODS monolayer in D_2O , shown by the

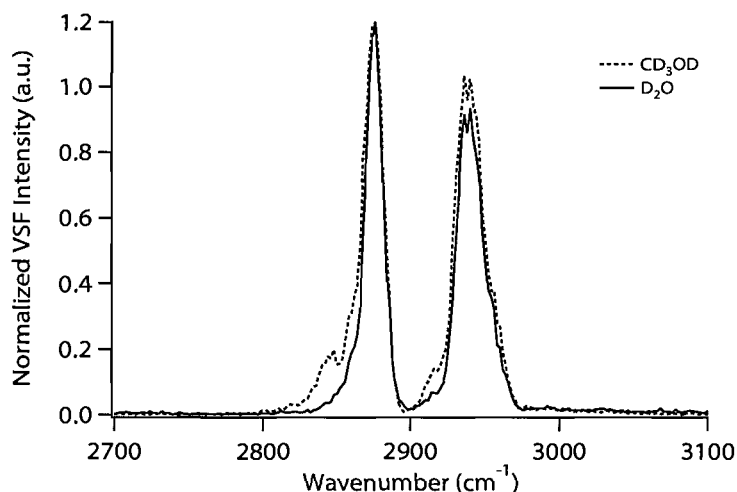


Figure 6.12. VSFS spectra of an ODS/D₂O and ODS/CD₃OD interface. The spectra are scaled to the same value at 2874 cm⁻¹.

solid line, and in CD₃OD, shown by the dotted line. There are clear differences between the spectra. First, the spectrum of the monolayer in fully deuterated methanol is significantly stronger than that of the D₂O spectrum, meaning that the amplitude of the first CH₃(ss) peak of the monolayer cannot be held constant in fitting. Second, in CD₃OD, the spectral shape changes. There is clearly an enhanced resonance near 2850 cm⁻¹ due to changes in the alkyl chains of the monolayer or the interfacial refractive index. This latter change is more significant as it will interfere very strongly with the methanol stretching vibration. As a result, detailed analysis has not been undertaken for all of the methanol spectra at this interface. Preliminary spectral fitting results show that the methanol peak is located at 2830±2 cm⁻¹ for the pure methanol/ODS interface; however further spectral fitting and analysis has not been attempted due to the apparent changes in the interface. Despite this, the

Table 6.1. Comparison of CH₃OH and H₂O figures of merit at FDS, ODS and air interfaces. Vibrational frequencies of CH₃OH and H₂O, ΔG° of CH₃OH and bulk concentration with maximum effective surface density.

	FDS	ODS	Air
CH₃OH - Location (cm⁻¹)	2838±2	2830±2	2836±2[180]
free-OH - Location (cm⁻¹)	3694 ± 2	3674 ± 2	3704 ± 2[100]
CH₃OH - ΔG° (kcal/mol)	-1.7±0.1	-1.6±0.2[92]	-1.6 - 2.1[187]
$\chi_{\text{CH}_3\text{OH}}$ at $N_{s,max}$	0.4	0.5	0.5[187]

general trends in these results match well with those in the literature[92] and the FDS results above.

Conclusion

VSFS studies have been performed at the interfaces of methanol:water solutions on ODS and FDS self-assembled monolayers. Measurement of the polarization dependant VSFS output of the CH₃(ss) mode shows that methanol adsorbs to the FDS interface with constant orientation. Methanol is also more favorably attracted to the interface than water, with a free energy of adsorption near -1.6 kcal/mol. Both of these findings are similar to those at the ODS[92] and air interfaces.[180, 187] Also similar to these interfaces is the concentration at which methanol fully displaces the interfacial water molecules, ≈ 0.5 mole fraction, which is where the VSFS signal is maximized. This displacement of interfacial water molecules leads to a shifting of the frequencies of both the free-OH and CH₃(ss), due to the changing hydrogen bonding configuration of methanol and the increasingly hydrophobic environment in which the straddling water molecules are located as methanol is added to the interface.

Despite these similarities, there are clear spectroscopic differences in the interfaces of methanol with FDS and ODS layers, manifested in the vibrational frequencies of the interfacial methanol molecules. The vibrational frequency of the $\text{CH}_3(\text{ss})$ at the neat methanol/FDS interface is $2838 \pm 2 \text{ cm}^{-1}$, which is near the frequency at the air/methanol interface, but is significantly different from that of the ODS/methanol interface. This result is similar to that seen for the free-OH peak of straddling water molecules, in which the frequency of the free-OH vibration is much closer to that of the air/water interface than the hydrocarbon/water interface. Taken together, these interfacial frequencies confirm that fluorocarbons have weaker intermolecular interactions with both polar and nonpolar functional groups and provide spectroscopic signatures for determining molecular interactions.

CHAPTER VII

FLUOROCARBON AND HYDROCARBON MONOLAYER INTERACTIONS
WITH BUTYLAMINE HYDROGEN CHLORIDE

The interaction strength of fluorocarbon and hydrocarbon monolayers with water and methanol have been found to be different, as measured by shifting interfacial frequencies. The greater hydrophobicity of fluorocarbon surfaces leads to blueshifting of the free-OH oscillator and more oriented interfacial water molecules due to more OH^- and H^+ ions at the interface. The greater lipophobicity of fluorocarbon surfaces leads to a blueshift of the methanol methyl symmetric stretch. Having established these frequency shifts as a measure of interaction strength and examined a neutral polar molecule, the next step is to understand the differences between the adsorption of charged species at FDS and ODS interfaces. A simple amine salt, butylamine HCl, has been investigated at both fluorocarbon and hydrocarbon monolayers via VSFS and contact angle measurements. Using isotopically substituted amines, the effects of adsorption of amines on the interfacial water and monolayers have been analyzed. Analysis of adsorption at pH 2 and pH 5.7 show that adsorption begins at the same bulk concentration, indicating that the electrostatic charge of the hydrophobic surface has little effect the adsorption process. The lipophobic nature of the fluorocarbon surface leads to a different adsorbate conformation than at the ODS interface. The

observed differences are validated by shifting interfacial frequencies of butylamine HCl and thermodynamic measurements.

Introduction

Investigations into charged species adsorption on hydrophobic surfaces by VSFS has primarily focused on relatively large molecules such as surfactants[149, 151, 188–192] and proteins[24, 193–199] adsorbing at polymer surfaces. Of particular interest, but not previously directly investigated at hydrophobic surfaces are amines and amine chlorides. This functional group is ubiquitous biologically and is highly important for a variety of industrial applications. Long chain alkylamine salts are used in flotation of silica[3, 200–204] and adsorption of long chain amines and their salts on SiO₂ has been studied by zeta potential,[200, 203, 204] IR spectroscopy[4, 205, 206] and VSFS.[207, 208] These molecules exhibit complex aggregation and adsorption behavior because of van der Waals or electrostatic intermolecular interactions and, in the case of proteins, structural rearrangement as a function of pH and adsorbed state.[189, 195, 196, 198, 203] Smaller molecules simplify these difficulties, allowing the direct, molecular level interactions between adsorbates and hydrophobic phases to be investigated.

The previous two chapters have characterized adsorption of ions and organics at FDS and ODS surfaces. Specifically, Chapter V showed that both types of monolayer surfaces are strongly affected by pH, but there is little specific adsorption of chloride ions. Analyzed in Chapter VI, methanol adsorption on both ODS and FDS

monolayers begins to displace water at similar bulk concentrations and a comparison with the literature found the adsorption behavior at FDS to be similar to ODS. The primary difference between methanol at FDS and ODS surfaces is the frequency of the $\text{CH}_3(\text{ss})$ vibrational mode at the two interfaces. This frequency difference is a signature of the weak interactions between fluorocarbons and hydrocarbons and helps explain the immiscibility of alkyl and fluoroalkyl molecules. In this chapter the complexity of the system investigated is increased by using a charged, small organic molecule, butylamine hydrogen chloride (BuNH_3Cl).

BuNH_3Cl has been chosen for two principle reasons. First, this molecule exhibits properties between those of simple salts and neutral, polar organics. This salt is highly soluble, but the four carbon alkyl tail is long enough to cause molecular ordering, as has been seen for interfacial butanol.[185] However, the chain is still small enough that inter-chain van der Waals attractions do not drive adsorption. Second, because the K_a is very small, it has a nearly negligible effect on the solution pH and remains ionized even at low pH. These two factors make BuNH_3Cl a good probe for examining the differences between adsorption at fluorocarbon and hydrocarbon surfaces. This chapter combines VSFS and static contact angle measurements to present a thorough analysis of the adsorption of butylamine HCl at FDS and ODS surfaces.

Experimental

VSFS experiments were performed as described in Chapter III. Each spectrum

shown is an average of 3 individual spectra collected at 20 shots per data point with a resolution of 2 cm^{-1} or 4 cm^{-1} for the CH stretching region and OH stretching region studies, respectively. The spectra are in the SSP polarization scheme unless otherwise noted. All spectra were background corrected and then normalized for the IR energy. Final spectral normalization was carried out using the IR transmission spectrum of the prism and monolayer sample.

FDS samples were deposited via the Langmuir-Blodgett method at a surface pressure of 15 mN/m . Hydrocarbon monolayers were deposited as described in Chapter III with a deposition time of 8 hours. All monolayer samples used were characterized using a KSV Attension Theta optical tensiometer. The tensiometer was spot calibrated to the diameter of the needle used to deliver the contacting liquid. Each drop was equilibrated 30 seconds and then 10 images were collected of the drop. This was done for a total of 5 drops per sample or data point. One sample of each monolayer batch was analyzed via AFM measurements as described in Chapter III to that deposited monolayers were smooth and uniform.

The isotopomers of butylamine HCl are shown in Figure 7.1. BuNH_3Cl can be purchased from a number of suppliers, but was found to be contaminated with small amounts of other organic compounds. Instead it was prepared from liquid butylamine(Aldrich) by reacting it stoichiometrically in a closed glass vessel with slowly added concentrated hydrochloric acid. The reaction products were then dissolved in water to produce an $\approx 1\text{ M}$ solution. The solution pH was measured

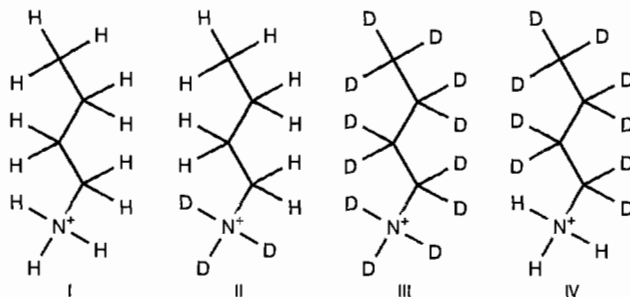


Figure 7.1. Isotopomers of BuNH_3Cl used within are: (I) Butylamine HCl (BuNH_3Cl), (II) Butyl-D2-amine DCl (BuND_3Cl), (III) D9-butyl-D2-amine DCl and (IV) D9-butylamine HCl ($d_9\text{-BuNH}_3\text{Cl}$).

using a 3-point calibrated pH meter and adjusted to the desired level using small amounts of sodium hydroxide or HCl. This stock solution was then diluted the desired amount using pH 2 HCl or Nanopure water to make lower concentration solutions at $\text{pH } 1.9 \pm 0.1$ and 5.7 ± 0.1 . Deuterium substituted BuNH_3Cl were acquired from CDN Isotopes and used without further purification. Solutions of $d_9\text{-BuNH}_3\text{Cl}$ were prepared by dissolving the salt in aqueous pH 2 HCl and diluting to the desired concentration. BuND_3Cl and $d_9\text{-BuND}_3\text{Cl}$ solutions were made by dissolving the molecules in pD 2 solutions of DCl (CDN Isotopes) dissolved in D_2O (Cambridge Isotopes).

Results and Discussion

Measurements were carried out on both fluorocarbon and hydrocarbon monolayer samples at $\text{pH} \approx 2$ and $\text{pH} \approx 5.7$. The pH 2 studies are first discussed, followed by comparisons with the results of those at 5.7. Two pHs have been used because

they separate electrostatically driven from hydrophobically driven adsorption at the interface. At pH 2, the monolayer interfaces are nearly electrically neutral as shown in Chapter V and thus any electrostatic forces driving adsorption are negated. These VSFS results are then correlated with data from contact angle measurements to create a full picture of the adsorption process.

VSFS of BuNH₃Cl Adsorption at pH 2: FDS

BuNH₃Cl adsorption on FDS was studied using the three isotopically substituted forms in Figure 7.1 to isolate the different vibrational modes present - water, monolayer and amine. FDS samples were first investigated with 1 M d₉-BuND₃Cl to determine if the amine has any effect on the CH₂ stretches of the monolayers, indicating significant penetration of the adsorbate into the monolayer. No changes were found in the VSFS spectra of the FDS monolayer, thus any changes in the CH region are due to interferences with water or the ordered adsorption of BuND₃Cl.

VSFS spectra of BuND₃Cl at the FDS/D₂O interface are shown in Figure 7.2. At pH 2, the spectrum contains resonances due to the monolayer alone. There are two large modes at 2917 cm⁻¹ and 2950 cm⁻¹ from the CH₂ groups in the monolayer itself. There is also a small shoulder on the low frequency side of the monolayer peaks at 2873 cm⁻¹. This peak is possibly from unhydrolyzed ethoxy groups in the monolayer; x-ray photoelectron analysis of FDS monolayers occasionally shows an anomalous small peak in the C_{1s} region. Addition of BuND₃Cl causes major changes in the VSFS spectra; new peaks appear between 2850 cm⁻¹ and 2900 cm⁻¹ and the

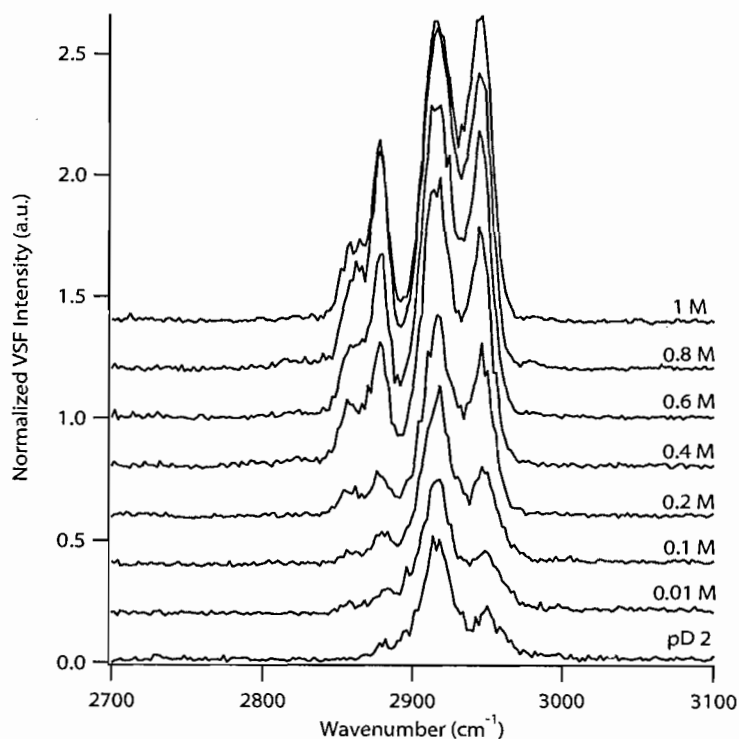


Figure 7.2. VSFS spectra of BuND₃Cl on the FDS surface in pD 2 D₂O. Spectra are offset for clarity.

monolayer CH₂ resonances appear to change. To verify that the changes in the CH region were due to the adsorbed species and not changes in the monolayer, VSFS spectra were collected using d₉-BuND₃Cl in D₂O at 1 M concentration. No changes in the spectra were observed, which confirms that the BuND₃Cl has no effect on the lower portion of the monolayer chains.

The complicated interference with the CH₂ peaks of the monolayer makes fitting this portion of the spectra accurately nearly impossible, thus conclusions will not be drawn from vibrational modes overlapping with these peaks. Analysis of the SSP spectra will be restricted to the spectroscopically isolated modes below 2900 cm⁻¹.

The first mode due to BuND₃Cl is located at 2852 ± 1 originates from CH₂(ss) vibrations. In well-ordered monolayers, the signal from these modes cancels out and the presence of large CH₂(ss) signals is indicative of gauche defects in the chains.[32] However, for the short chains present here, it is not certain if this principle holds. Each of the CH₂ groups is in a unique molecular environment. One is bonded to the amine, one is next to the CH₃ group and the third is between these two groups. Previous research on ODS monolayers has found evidence for distinct signals from CH₂ groups in well-ordered chains when these groups are in unique environments.[87] From this argument, it is highly possible that some amount of the detected CH₂ vibration is intrinsic and not directly related to the chain conformation.

The CH₃(ss) is the second peak present below 2900 cm^{-1} in Figure 7.2. Spectral fitting places this peak at 2882 ± 1 , which is blueshifted by $\approx 10 \text{ cm}^{-1}$ from the normal location of an alkyl chain CH(ss), nominally 2873 cm^{-1} . This frequency shift is similar to that seen in Chapter VI for methanol at FDS versus ODS (2838 cm^{-1} vs. 2830 cm^{-1}) and indicates that the methyl group of BuND₃Cl is pointed towards the FDS monolayer, directly interacting with it. The presence of this peak and the absence of a distinct peak above 2960 cm^{-1} due to the CH₃(as) indicates that the methyl groups are well-ordered with transition dipoles oriented normal to the interface. The methyl asymmetric stretch transition dipole moment is 90 degrees out of alignment with the symmetric stretch and primarily appears in SPS spectra when these groups are well-ordered.

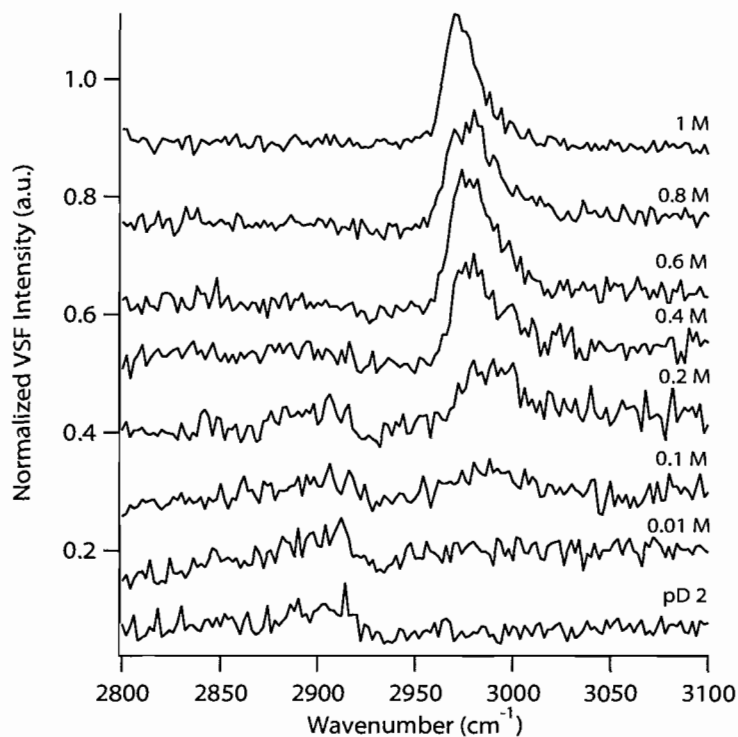


Figure 7.3. SPS polarized VSFS spectra of BuND₃Cl on the FDS surface in pD 2 D₂O. Spectra are offset for clarity.

This is exactly what is seen in the SPS spectra of BuND₃Cl, which probes components of the transition dipole parallel to the interfacial plane. As can be seen in Figure 7.3, there is a sharp resonance near 2968 cm⁻¹ from the CH₃(as) vibration. The small dip in the spectra is due to the CH₂ modes of the monolayer. These modes are interfered with by the CH stretching vibrations of BuND₃Cl to yield a flat background around the CH₃(as) peak. The ratio of CH₃(as) to CH₃(ss) is nearly constant in this polarization (≈ 1.8) over the range in which the asymmetric stretch can be accurately fit (0.6 to 1 M), indicating that the methyl group does not change orientation once this threshold is reached. However, this does not yield information

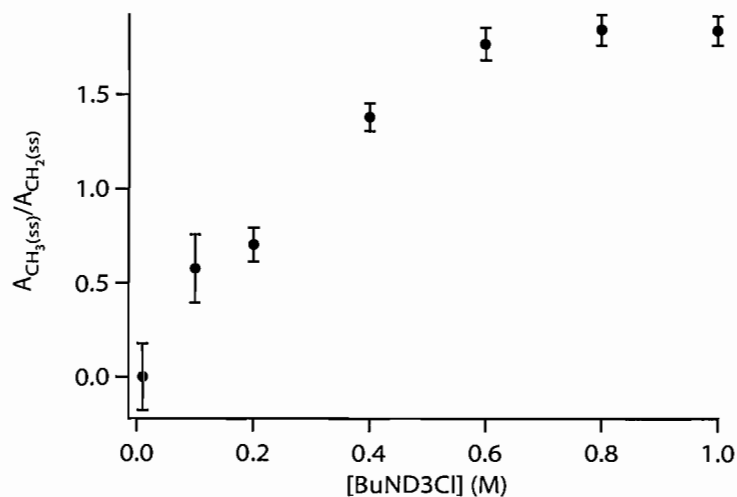


Figure 7.4. SSP fit amplitude ratio of $CH_3(ss)$ to $CH_2(ss)$ as a function of $BuND_3Cl$ concentration at pD 2 on FDS.

about the lower concentrations. For that, careful examination of the SSP spectra is required.

The two peaks that can be most accurately fit using the global fitting routine are the $CH_2(ss)$ and $CH_3(ss)$ from the SSP spectra. The ratio of $CH_3(ss)$ to $CH_2(ss)$ is plotted across the entire concentration range in Figure 7.4. Increasing the $BuND_3Cl$ concentration increases the ratio of $CH_3(ss)$ to $CH_2(ss)$ from near zero to 1.85, showing that the orientation of the adsorbate changes as it adsorbs to the surface. Assuming the increase in this ratio indicates a decrease in gauche defects, then the alkyl chains are becoming more ordered with increasing bulk concentration. This kind of behavior has been seen for surfactant adsorption at several interfaces.[149, 151, 208–210] As bulk concentration increases, more $BuND_3Cl$ adsorbs to the monolayer. To

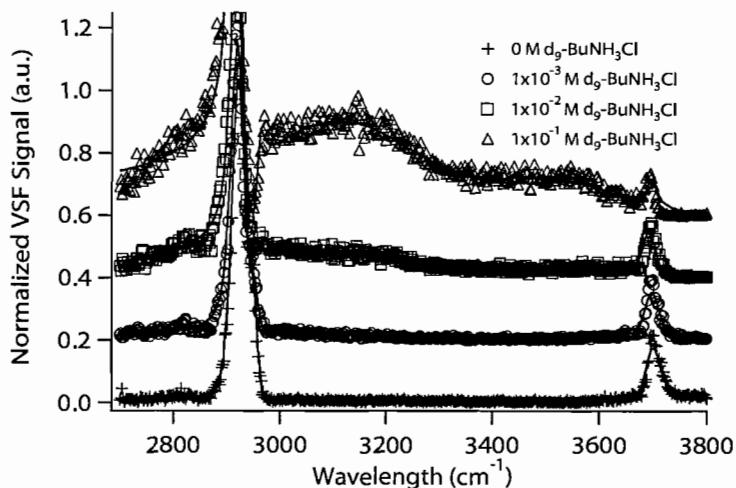


Figure 7.5. VSFS spectra of d_9 -BuNH₃Cl adsorbing onto an FDS monolayer in pH 2 HCl. The spectra have been offset and truncated for clarity.

make room for more adsorbate the BuND₃Cl reorients on the surface to form a more tightly packed layer.

The CH region spectra show no measurable differences below 0.01 M, but the adsorption process may begin at a much lower concentration. Because there is little or no interfacial electrostatic field at this bulk pH, only a small amount of BuNH₃Cl needs to adsorb to the monolayer/water interface to create a net interfacial charge. This interfacial charge will alter the VSFS response of water molecules in the interfacial region. This is shown in Figure 7.5 using d_9 -BuNH₃Cl. Using the deuterated chain means that any apparent changes in the CH modes are only due to interference effects and not from amine adsorption.

With no amine present (only the pH 2 HCl) the monolayer water spectrum shows the two CH₂ modes of the monolayer and the free-OH peak at 3694 cm⁻¹.

At 1 mM d_9 -BuNH₃Cl, there is a very small increase in the coordinated water signal. Increasing the concentration further to 0.01 M results in a small increase in coordinated water; however, the free-OH is unaffected by this small level of adsorption. When the concentration is increased to 0.1 M, the VSFS response due to coordinated water greatly increases while at 0.1 M, the free-OH amplitude is decreased due to the displacement of interfacial water molecules by d_9 -BuNH₃Cl. The increase at 0.01 M correlates well with the first appearance of CH stretching vibrations of BuND₃Cl in Figure 7.2.

The phase relationship between the free-OH and the CH₂ resonances of the monolayer can also be used to confirm the direction of the CH₃(ss) transition dipole. The free-OH points into the monolayer with an assigned phase of π , which is the same as the CH₂(as) of the monolayer at 2917 cm⁻¹ and the CH₃(ss) of the amine. Combined with the frequency shift of the CH₃ compared to the normal CH₃ frequency, it is clear that BuNH₃Cl adsorbs onto FDS with the hydrophobic group pointing towards to the monolayer. It is also clear that BuNH₃Cl begins to adsorb to the interface around 1 mM bulk concentration, but does so without any discernible order until bulk concentration is a few orders of magnitude higher.

VSFS of BuNH₃Cl Adsorption at pH 2: ODS

Using the same isotopic substitution strategy as on FDS, adsorption of ODS has been studied. First, the water stretching spectra were investigated using the d_9 -BuNH₃Cl. Spectra collected in water (Figure 7.6) tell a similar story

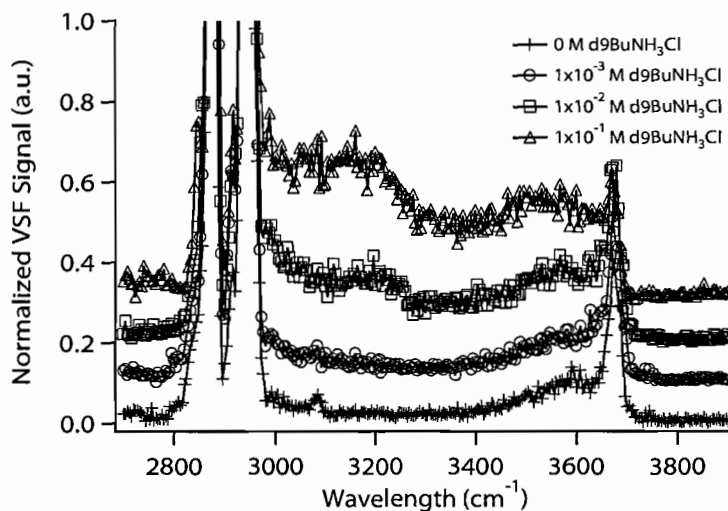
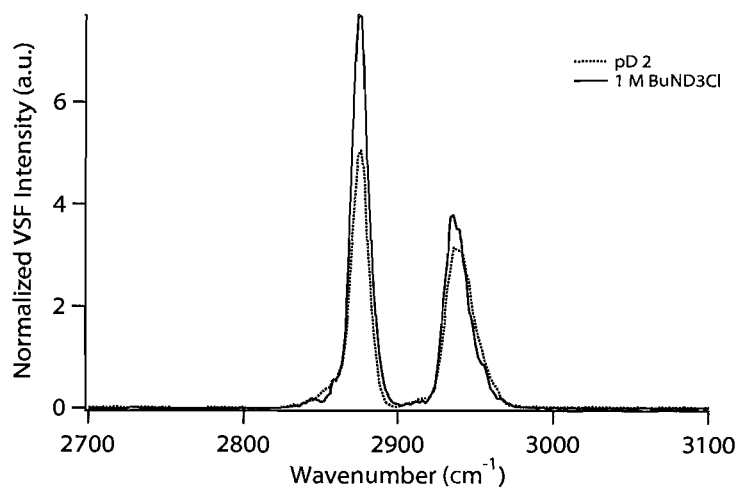


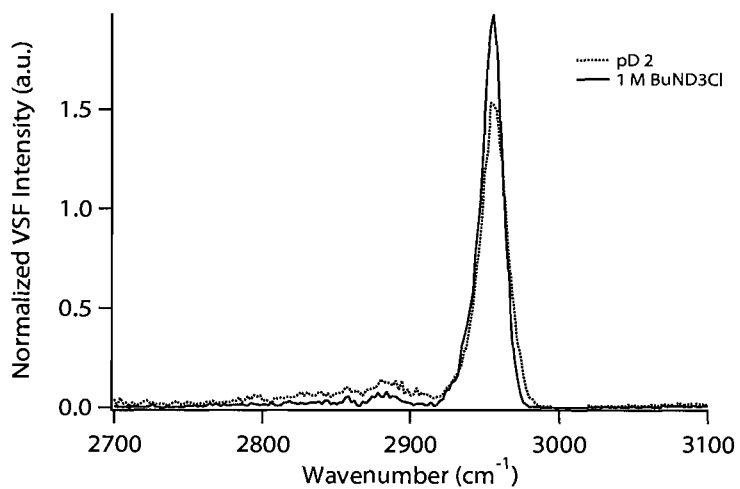
Figure 7.6. Spectra of the CH and OH stretching region of an ODS monolayer with d_9 -BuNH₃Cl at pH 2. Spectra are truncated and offset for clarity.

to those in D₂O. At pH 2, there is no apparent signal from coordinated water molecules. The spectrum shows the CH stretches of the ODS monolayer, the free-OH near 3670 cm⁻¹ and the small broad peak due to solvated water molecules near 3600 cm⁻¹. Addition of d_9 -BuND₃Cl to the interface increases the water signal in the 3000-3600 cm⁻¹ region as the positively charged adsorbate populates the interface, introducing charge which electrostatically orients water molecules in interfacial region. Based on this, amine adsorption begins to occur near 0.01 M, just as in FDS.

Whilst the water region indicates that adsorption begins near 0.01 M, there are no changes in the ODS CH region spectra until 0.1 M. Figure 7.7(a) shows the SSP spectra of 1 M BuND₃Cl on an ODS monolayer. There are two principle differences between the spectra. The first is that the 1 M spectrum has much more intensity in the CH₃(ss) near 2870 cm⁻¹. The second principle difference is the change in the



(a) SSP



(b) SPS

Figure 7.7. (a) SSP and (b) SPS spectra of the CH stretching region of an ODS monolayer with BuND₃Cl in pD 2 D₂O.

shoulder of the $\text{CH}_3(\text{ss})$ peak near 2850 cm^{-1} , indicating a change in the $\text{CH}_2(\text{ss})$ stretching signal with adsorption. SPS spectra Figure 7.7(b) show a clear increase in the intensity of the $\text{CH}_3(\text{as})$ vibration in the spectrum with increasing concentration, and an apparent decrease in the intensity below 2900 cm^{-1} .

These changes are difficult to interpret because the peaks of the monolayer and amine have the same frequencies. To determine if the changes are partially due to the monolayer, spectra have been collected using the fully deuterated $\text{d}_9\text{-BuND}_3\text{Cl}$. With fully deuterated BuNH_3Cl , changes in the monolayer are decoupled from the adsorbate because the CD vibrations of the adsorbate are shifted a few hundred wavenumbers below the CH stretching region. Just as with FDS monolayers, the exposure of ODS monolayers to $\text{d}_9\text{-BuND}_3\text{Cl}$ showed no changes with concentration. This indicates that changes in the CH peaks in Figure 7.7 are caused by added BuND_3Cl no effects of the adsorbate on the monolayer.

Spectral deconvolution has been used to analyze the changes in the ODS spectra in both polarizations. Because the adsorbate and monolayer peaks overlap, all of the spectra have been analyzed using the five monolayer peaks varying only their individual amplitudes. The two largest peaks in Figure 7.7(a) are from the $\text{CH}_3(\text{ss})$ Fermi resonance pair and are located at 2874 ± 1 and $2934 \pm 3\text{ cm}^{-1}$. In Figure 7.7(b), the largest peak arises from the $\text{CH}_3(\text{as})$ at $2955 \pm 2\text{ cm}^{-1}$. There are also two small peaks due to the $\text{CH}_2(\text{ss})$ at $2848 \pm 2\text{ cm}^{-1}$ and the $\text{CH}_2(\text{as})$ at $2914 \pm 3\text{ cm}^{-1}$.

Restricting analysis to the peaks at 2874 cm^{-1} and 2955 cm^{-1} , which can be fit

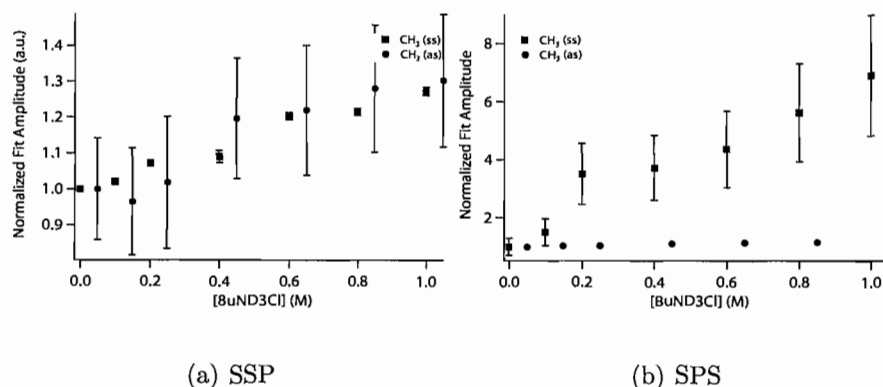


Figure 7.8. Amplitude of (a)SSP and (b)SPS CH₃(ss) and CH₃(as) stretches normalized to 1. The ● traces have been offset by 0.05 M for clarity.

with a relatively high degree of accuracy in one or both spectra, the normalized fit amplitudes of these peaks has been plotted in Figure 7.8. The amplitudes have been normalized to the amplitude with no adsorbate. A normalized amplitude greater than 1 indicates an increase in the amplitude and thus a constructive interference by BuND₃Cl. Figure 7.8(a) shows that the amplitudes of both CH₃ stretches increase monotonically with the addition of BuND₃Cl. Figure 7.8(b) also shows a monotonic increase in the CH₃ stretching amplitudes, but the symmetric stretch increases much more rapidly than the asymmetric stretching mode. Taken together, these plots indicate two things. First, all of the amplitudes increase with adsorption, indicating that the vibrational resonances of the amine CH₃ groups are in phase with those of the monolayer. This means that the CH₃ group of BuNH₃Cl is oriented in the same direction as the ODS methyl group. Second, the relative increase in the amplitude of the CH₃(ss) is much greater in plane than out of plane, which indicates that BuNHD₃Cl adsorbs slightly more parallel to the interface than normal. However, the

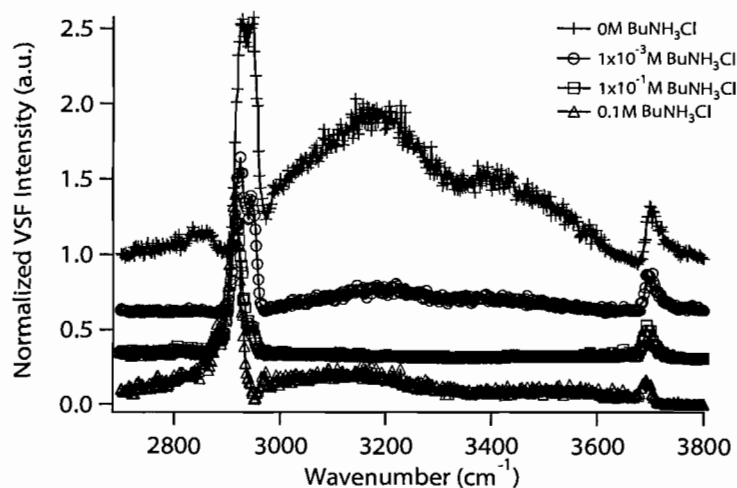


Figure 7.9. VSFS spectra of the FDS/BuNH₃Cl(aq) interface at pH 5.7. Spectra are offset for clarity.

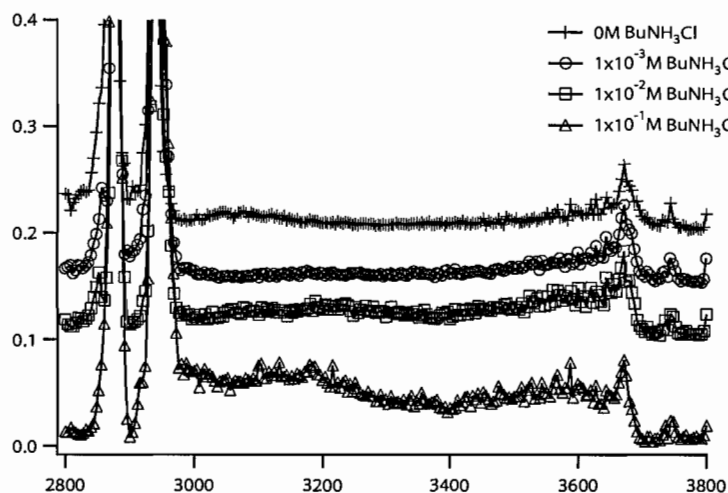


Figure 7.10. VSFS spectra of the ODS/BuNH₃Cl(aq) interface at pH 5.7. Spectra are offset for clarity.

lack of large absolute increase in the intensity of the SPS spectrum in Figure 7.7(b) indicates that adsorption occurs with little in-plane order.

VSFS of BuNH₃Cl Adsorption at pH 5.7

VSFS spectra of BuNH₃Cl solutions at FDS and ODS surfaces at pH 5.7 are

shown in Figures 7.9 and 7.10, respectively. The FDS spectra in Figure 7.9 have three principle regions, as described in previous chapters. The first is the CH stretching region, which is marked by the narrow bands of the $\text{CH}_2(\text{as})$ modes from the monolayer near 2920 cm^{-1} . Second is the coordinated water stretching region from $\approx 3000\text{ cm}^{-1}$ to 3600 cm^{-1} containing the broad bands indicative of coordinated water stretching vibrations by electrostatically oriented water. Third is the narrow mode near 3700 cm^{-1} due to the free-OH of straddling water molecules. The spectra show significant changes in each of these three regions with increasing BuNH_3Cl concentration. There are significant changes in the CH stretching region, but a comparison with the spectra in Figure 7.5 shows that these changes are due to interference with the broad water modes and not organized BuNH_3Cl adsorption. The free-OH peak remains relatively unchanged in this concentration range, with the amplitude decreasing only slightly with increasing concentration. Finally, the coordinated water region decreases rapidly with increasing ionic strength, more rapidly than in the NaCl experiments in Chapter V. This indicates that BuNH_3Cl is more effective at screening the charge than a simple electrolyte, because it is more attracted to the interface than NaCl. Unlike NaCl, BuNH_3Cl decreases the signal in the coordinated water stretching region to zero at 0.01 M after which VSFS signal from coordinated water molecules increases. This is due to interfacial charge reversal and has been seen in several VSFS surfactant adsorption studies.[161, 207–211] It is important to note that at concentrations higher than 0.1 M, the refractive index

of the aqueous phase no longer allows total internal reflection and the VSFS signal ceases to be reliable.

Figure 7.10, shows the same concentration range of BuNH_3Cl solutions at the ODS interface. The CH peaks of these spectra have been truncated so the water region is more visible. Intensity in the coordinated water stretching region decreases slightly at 1 mM BuNH_3Cl , but clearly increases in intensity with higher concentration. The spectrum at 0.1 M has significantly more intensity than the pure water spectrum, indicating that the interfacial charge is now positive. Indicating that sufficient BuNH_3Cl has adsorbed to reverse the interfacial charge. Both sets of spectra in Figures 7.9 and ODSwaterph58 show that significant adsorption occurs at the same bulk concentrations whether the surface is nearly neutral or negatively charged. This means that adsorption is driven by bulk solubility and the hydrophobic interactions of the monolayers with water.

Contact Angle and Interfacial Tension Measurements

To gain further insight into the behavior of BuNH_3Cl solutions at these interfaces, the interfacial thermodynamics were studied using contact angle measurements. Both monolayer interfaces are hydrophobic in their interactions towards water and have high contact angles. As the BuNH_3Cl adsorbs to the monolayer surface, the solid-liquid interfacial tension is reduced because of the presence of the charged adsorbate. This reduction results in decreasing water contact angles.

BuNH_3Cl adsorption as measured by water contact angle is shown in Figure 7.11.

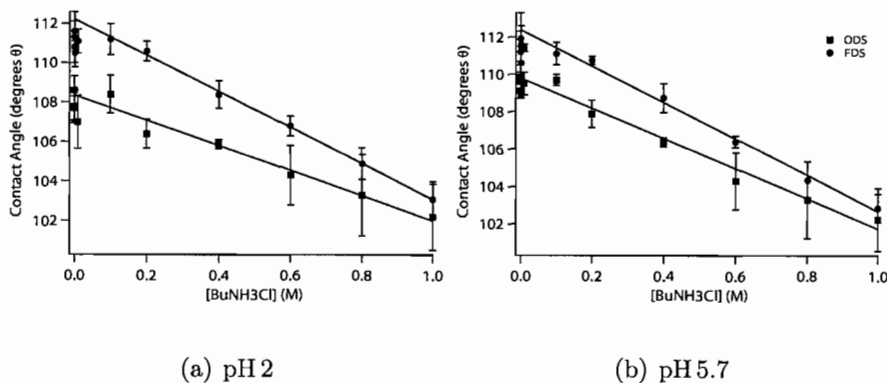


Figure 7.11. Static contact angle measurements of aqueous BuNH₃Cl at (a) pH 2 and (b) pH 5.7 solutions on ODS and FDS monolayers. The lines are linear fits to the data between 0.1 M and 1 M concentrations.

The initial contact angles of pure water and pH 2 HCl are nearly the same; the pH 2 measurements are slightly lower, but this could be sample to sample variation. In the analysis below, a uniform decrease in contact angle has little effect on the computed interfacial tension and adsorption coefficient. The contact angle of water with FDS is 111.9 ± 1.4 and pH 2 HCl is 110.8 ± 0.8 . On the ODS samples used, the contact angles are 109.6 ± 0.4 in water and 108.6 ± 0.8 in pH 2 HCl. The contact angle results show the contact angle decreases monotonically with solution concentration beginning at 0.1 M BuNH₃Cl. Smaller concentrations have no significant effect on the contact angle at either surface. The duplication of this trend at both pHs studied shows that the salt is not strongly attracted to either surface, even when they are negatively charged, confirming the VSFS results.

The partitioning of butylamine HCl at the interface can be described by the Gibbs

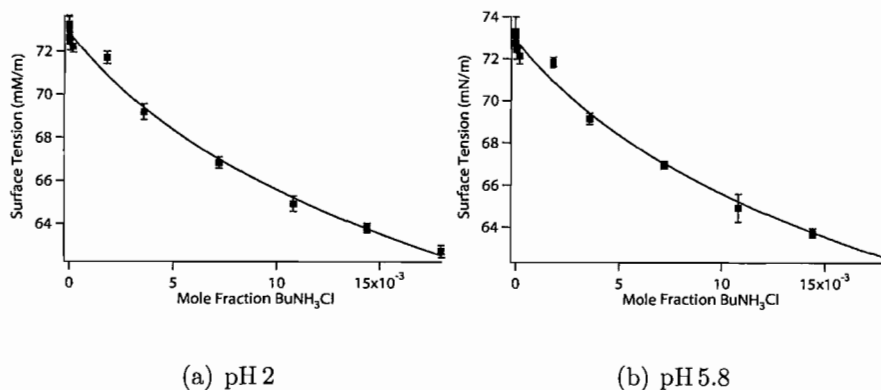


Figure 7.12. Interfacial tension measurements of aqueous BuNH₃Cl solutions at (a) pH 2 and (b) pH 5.7. The solid line is a fit to Equation VII.4.

equation, which relates the surface excess, Γ , to the concentration, χ , of the adsorbate:

$$-RT\Gamma = \left(\frac{\partial \gamma_{SL}}{\partial \ln \chi} \right)_T \quad (\text{VII.1})$$

where R is the gas constant, $8.314 \text{ J mol}^{-1} \text{ K}^{-1}$, T is the temperature and γ_{SL} is the solid-liquid interfacial tension. The solid-liquid interfacial tension cannot be attained directly from the contact angle measurements, but using the Young equation (Equation VII.2), the Gibbs equation can be rewritten as a function of the contact angle, θ and the liquid-vapor surface tension, γ_{LV} .

$$\gamma_{SL} = \gamma_{SV} - \gamma_{LV} \cos(\theta_{eq}) \quad (\text{VII.2})$$

Young's equation describes the equilibrium of a liquid drop in contact with a solid under the influence of three tensions. In this equation, θ_{eq} is the equilibrium contact angle, γ_{LV} is the liquid-vapor interfacial tension and γ_{SV} is the solid-vapor interfacial tension. γ_{LV} is solution dependent and has been measured for each of the solutions used here; the values are shown in Figure 7.12. The surface energy of the solid can be

determined from a Zisman plot of the contact angles of a series of liquids of known surface tensions; in the case of ODS monolayers of similar water contact angle, it has been found to be 20 ± 1 mN/m.[212, 213]. This is nearly the same as the critical surface tension of Teflon, which is ≈ 19 mN/m.[214] It is important to note that γ_{SV} is actually the value of the surface tension of the system in equilibrium with the vapor of the contacting solution. However, the choice of the value for γ_{SV} is inconsequential in the overall analysis because it serves only as an offset for calculating the absolute interfacial tension, this offset is incorporated into the γ_0 term of Equation VII.4 below and has no effect on the calculated quantities. Using these values, the solid-liquid interfacial tension can be calculated; these results are shown in Figure 7.13.

Assuming that the surface excess is much greater than the bulk concentration and that the adsorption energy is constant, adsorption at the surface can be described using the Langmuir isotherm:[113]

$$\Gamma = \frac{k\chi}{\omega(1 + k\chi)} \quad (\text{VII.3})$$

where ω is the cross-sectional molecular area, χ is the bulk solution concentration and k is the adsorption equilibrium constant. Substituting Equation VII.3 into Equation VII.1 and integrating results in the Szyszkowski equation, which can be used to model interfacial tension data:[113]

$$\gamma_{SL} = \gamma_0 - \frac{RT}{\omega} \ln(1 + k\chi) \quad (\text{VII.4})$$

Fits to the line tension are shown in Figure 7.13 and are summarized in Table 7.1.

Table 7.1.. Parameters derived from contact angle and surface tension measurements of BuNH₃Cl solutions.

	pH 2		pH 5.7	
	FDS	ODS	FDS	ODS
ω (m ² /mol)	$6.7 \times 10^4 \pm 3.1$	$1.8 \times 10^5 \pm 0.8$	$6.8 \times 10^4 \pm 3.1$	$1.4 \times 10^5 \pm 0.8$
MMa (Å ² /molecule)	11 ± 5	29 ± 13	11 ± 5	24 ± 13
k	21 ± 10	52 ± 31	23 ± 8	52 ± 27
ΔG (kcal/mol)	-1.8 ± 0.3	-2.3 ± 0.3	-1.9 ± 0.2	-2.3 ± 0.3

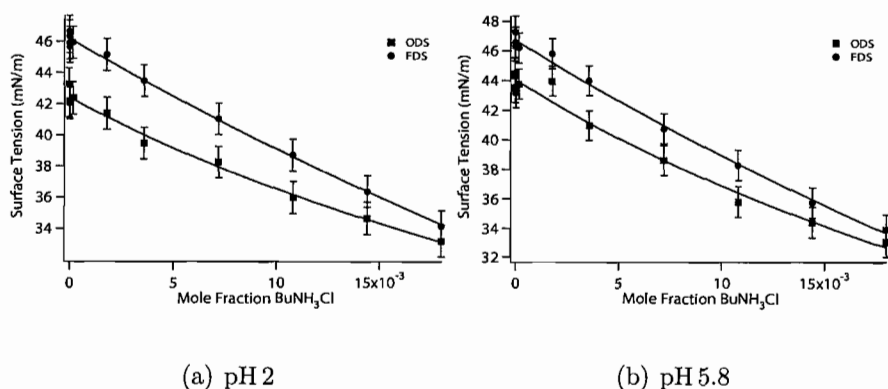


Figure 7.13. Solid-liquid interfacial tension of ODS and FDS monolayers with BuNH₃Cl at (a) pH 2 and (b) pH 5.7. The solid lines are fits to the data using Equation VII.4.

From this analysis it is immediately clear that there is no difference in the interfacial behavior of BuNH₃Cl at pH 2 and pH 5.7. Additionally, the molecular area of BuNH₃Cl is smaller at FDS than ODS. This suggests that there is significantly more adsorbed at the FDS layer than at the ODS layer. From k , the adsorption equilibrium constant, the free energy of adsorption can be computed using $\Delta G = -RT \ln k$. These values are all negative, indicating that adsorption is energetically favorable at the interface, with adsorption being slightly less favorable at the fluorocarbon surface due to the well-documented lipophobicity of the fluorocarbons.[215–218] They are also very similar to the free energy of adsorption reported for methanol Chapter VI, indicating that BuNH₃Cl adsorption is approximately as favorable as methanol. At the fluorocarbon surface, more BuNH₃Cl must adsorb to affect the same magnitude of contact angle decrease as on the hydrocarbon monolayer because of the greater

the interface in a nearly all-trans configuration, such as that seen in Figure 7.14(a). In the case of adsorption at ODS, the addition of BuNH_3Cl increases the intensity of the methyl stretching modes, indicating that this group is oriented in the same direction as the monolayer chains. Coupling this with the small, but disproportionate increase in the in-plane signal of the methyl symmetric stretch, BuNH_3Cl adsorbs with the methyl group facing away from the monolayer, but with a slightly larger component of the transition dipole parallel to the interfacial plane. This requirement is met if the molecule adsorbs with a structure similar to Figure 7.14(b). This configuration requires a larger interfacial area, which has been calculated by the isotherm. Such disordered adsorption has been seen for sodium dodecylsulfate at alkane thiol interfaces.[149, 184]

Conclusions

A combination of VSFS and contact angle measurements have been used to provide a picture of the adsorption of a small surfactant molecule, BuNH_3Cl , at fluorocarbon and hydrocarbon interfaces both in the absence of and with surface charge. At pH 2, the point of zero charge of SiO_2 , the differences between the surface potentials of the two monolayers are negligible. This results in there being no electrostatically oriented water due to the near zero surface potential. Thus, there is neither charge screening due to the addition of BuNH_3Cl nor electrostatic attraction of the positively charged adsorbate to the interface. As BuNH_3Cl is added, it begins to adsorb near

0.01 M concentration at both the FDS and ODS surfaces. This positively charges the interface and electrostatically orients water molecules. This stage of adsorption occurs before there is any change in the macroscopic measure of adsorption, the water contact angle. At this stage of adsorption, what BuNH_3Cl is present at the interface is randomly oriented.

Upon reaching a critical bulk concentration, approximately 0.1 M, the adsorbate molecules begin to adsorb in a more organized fashion. This organization is very clear at the FDS interface where between 0.1 and 0.6 M the BuNH_3Cl molecules transition from disorganized chains with gauche defects to a state that is closer to all-trans for continued adsorption. At the ODS interface, BuNH_3Cl molecules begin to adopt some net orientation in this same concentration range; however, there is no clear change in molecular structure. It is in this region of organized adsorption that the contact angle begins to decrease.

The structure of BuNH_3Cl is clearly different at the two interfaces, with it adopting a more trans conformation at FDS, but lying relatively flat on an ODS monolayer. The thermodynamics of adsorption are energetically unfavorable at the FDS interface and the frequency of the methyl vibrations are blue-shifted by $\approx 10\text{ cm}^{-1}$ from their normal location at this interface. At ODS, adsorption is slightly energetically favorable and the methyl vibrations of BuNH_3Cl are not shifted. This provides experimental verification of the lipophobicity of the fluorocarbon surface and explains the differences in adsorbate conformation. The unfavorable interaction

between BuNH₃Cl and FDS results in the minimization of contact area, while this driving force does not exist at the ODS surface. Since the chain-chain interactions of BuNH₃Cl are weak, this unfavorable interaction helps them orient in a mostly trans configuration. At the ODS surface, this is not the case and the molecules are not driven to become well-ordered.

The effect of the interfacial electrostatics was also analyzed. For the low charge densities studied here, there was no apparent effect of a negative interfacial charge on the adsorption of BuNH₃Cl. The point of interfacial charge reversal is equal for both surfaces at both pH 2 and 5.7, showing that at these low charge densities, BuNH₃Cl is not strongly attracted to either interface, but prefers to remain fully solvated. The small free energies of adsorption and lack of difference between them at the two pH values examined confirm this conclusion. Thus, adsorption appears to primarily be driven by bulk solubility effects, not specific hydrophobic forces. The effect of those forces remains subtle.

Observed differences in adsorbate molecular orientation at fluorocarbon and hydrocarbon surfaces shows that lipophobic interactions between fluorocarbon and hydrocarbons can affect adsorption processes. These results help explain differences in biomolecule adsorption at fluorocarbon and hydrocarbon surfaces and may lead to different lubricant designs for fluorinated and hydrogenated surfaces.

CHAPTER VIII

SPECIFIC ION ADSORPTION AT THE $\text{CaF}_2/\text{WATER}$ INTERFACE

The results in this chapter were published in volume 26 of *Langmuir* in July 2010. Simon Schrödle initially found that specific ions altered carboxylate adsorption at the $\text{CaF}_2/\text{H}_2\text{O}$ interface and performed the preliminary experiments. Adam J. Hopkins performed all of the experiments shown in this chapter and published. Geraldine L. Richmond was the principle investigator.

Calcium fluoride is a slightly soluble compound commonly extracted from ores via flotation at elevated pH, where surfactant molecules bind with hydroxylated surface sites. The addition of F^- (aq) suppresses surfactant adsorption by replacing these sites. In this chapter, the effects of aqueous Cl^- , Br^- , F^- and SO_4^{2-} on the water structure at the $\text{CaF}_2/\text{H}_2\text{O}$ interface at a pH where surface hydroxylation has not yet occurred is examined. Using static and time-resolved VSFS, aqueous Cl^- and Br^- were found to have only electrostatic screening effects on the interface and do not perturb the interfacial water or surface structure. Sulfate was found to be strongly attracted to the interface and affects the interfacial water more than Cl^- or Br^- . This is in contrast to F^- ions that directly interact with the surface and alter the water structure and bonding at the CaF_2 surface in addition to screening the surface charge.

Introduction

The charged solid/aqueous interface is of great importance in a variety of processes, both natural and industrial, and therefore has been the subject of much interest. Processing of mineral ores typically uses chemical flotation, which is dependant on surface chemical properties that are influenced by the dissolution of the surface ions.[219] Commonly these interfaces are investigated through spectroscopic[220, 221] or electrokinetic[222, 223] methods requiring the use of fine powders; however, the random orientation of the crystallographic planes of the powders and the high defect density can yield significantly different results compared to planar crystalline surfaces. For example, the isoelectric point (IEP) of alumina has been reported as pH 5.5 for a single crystal surface and pH 9 for powders.[224] Accessing these interfaces can be done spectroscopically, but interfacial behavior that occurs at the water-salt interface is often difficult to distinguish from the larger effects of the bulk aqueous solution. Vibrational sum-frequency spectroscopy (VSFS), which is used in the studies herein, is ideally suited to these types of studies because it is inherently sensitive to the small number of interfacial species present without regard to those in the bulk phase.

Much effort has been devoted to understanding interactions of adsorbates at the fluorite/water interface. An array of sulfate and carboxylate surfactants adsorbing at this interface have been studied in the Richmond laboratory[158, 161, 209–211, 225–228] and others[5, 229–231] using both static and dynamic measurements. These

studies have found that adsorption processes occur at the interface via interaction with hydroxyl substituted sites, based on the increase in adsorption with increasing pH. Direct spectroscopic evidence for the presence of surface hydroxyls at pH 6.4 and higher has been reported.[158] A recent study by Schrödle *et al.* examined acetate adsorption at the CaF_2 /water interface.[225] It found that acetate adsorption increases with increasing pH but is strongly suppressed by F^- ions added in excess of the solution equilibrium concentration predicted by the CaF_2 solubility equilibrium constant. The authors concluded that F^- replaces significant numbers of surface hydroxyls, which are present at pHs greater than the point of charge neutrality ($\text{pH} \approx 8.5$), reducing the number of surface binding sites where acetate can adsorb. This finding was unexpected given that zeta potential measurements have not found F^- to be a potential determining ion for CaF_2 , suggesting that F^- is not able to directly interact with the CaF_2 surface.[222, 232–235] These studies proposed that breaking of the tightly held solvation shell of F^- was not sufficiently energetically favorable to allow the ion to penetrate the hydration layer of the fluorite surface and bind with the surface.

To reconcile these results, the study within directly interrogates the CaF_2 /water interface with VSFS using aqueous F^- , Cl^- , Br^- , SO_4^{2-} and Ca^{2+} ions. These studies are conducted at a constant pH that is slightly below the point of charge neutrality, in nonequilibrium conditions maintained using a constant flow of solution over the surface. Use of flowing solutions replicates conditions commonly used in

electrokinetic measurements of interfacial potentials while retaining the sensitivity advantages of nonlinear spectroscopy. This is because VSFS directly measures the interfacial structure, not the potential at the shear plane some distance beyond the electric double layer. The selected pH ensures that the surface has a small, net positive charge, but is free of hydroxyl substituted sites that may preferentially interact with the introduced ions. Using a combination of static and dynamic studies, new information has been obtained regarding the direct interaction of F^- and the very different behavior of the other ions with the CaF_2 surface and surrounding interfacial water molecules.

Experimental

Laser System

Work performed in this chapter was done on a different laser system than that in the previous chapters and is briefly described here, details of the laser system have been previously reported.[156, 236] These experiments utilized a commercially available laser and IR generation stage (Ekspla) producing 532 nm pulses and tunable IR (2700-3900 cm^{-1} for this experiment). The visible and IR beams were incident on a 68° CaF_2 prism in a total internal reflection geometry with incident angles 20.5° and 17° from horizontal, respectively. All frequency domain spectra were collected at 4 cm^{-1} resolution, 60 shots per data point. The time resolved experiments were performed averaging 60 shots per point with an acquisition rate of approximately one

point per 16 s. The resulting VSFS signal was filtered by narrow bandpass filters and detected with photomultiplier tube attached to a monochromator. This signal was then normalized to both the visible and IR energy.

The solutions in contact with the prism were kept continuously flowing by means of a peristaltic pump connected to a Kel-F cell via PTFE tubing. This was critical to prevent dissolution of the CaF_2 from affecting the pH of the unbuffered solutions. The cell has a height of 2.5 mm with a volume of 0.15 mL. The flow rate used in these experiments, ≈ 1 mL/min, replaces the contents of the cell six to seven times a minute, a time scale much longer than the diffusion of ions to the interface. The solution reservoir was continually monitored by a glass electrode connected to a calibrated pH meter.

Sample Preparation

The NaCl and NaBr salt solutions were made from 10 M ionic strength stock via serial dilution with H_2O (resistivity $\approx 18.2 \text{ M}\Omega\cdot\text{cm}$) and NaF, Na_2SO_4 and CaCl_2 from 1 M ionic strength stock solutions. The salt solutions were all adjusted to $\text{pH } 5.8 \pm 0.2$ via small additions of HCl or NaOH as needed and continually flowed over the surface. The salts were purchased from Aldrich (SigmaUltra) and baked at 250°C overnight prior to use. All glassware was cleaned by soaking in concentrated sulfuric acid with NoChromix (Godax Laboratories) and rinsing with copious amounts of purified water. The surface of the CaF_2 prism was regularly cleaned by briefly soaking in sulfuric acid, polishing with $0.05 \mu\text{m}$ Al_2O_3 powder and rinsing with purified water.

Results and Discussion

Solution Equilibrium Structure

Upon exposure of CaF_2 to water at pH 5.8 preferential dissolution of the fluoride ions generates a positive interfacial potential. This potential results in the orientation of water molecules in the interfacial region with their dipoles normal to the surface, as measured in these VSFS experiments. These electrostatically oriented molecules occupy the electric double layer. This region defines the optically probed interface and has a thickness that varies with ionic strength and surface charge. VSFS has previously been used to investigate the effects of pH on this interface.[158] As the pH approaches the pH of the point of zero charge, the VSFS signal from the molecules in the double layer decreases due to decreasing surface charge. To probe ion specific effects, the pH is held constant at 5.8, keeping the surface charge constant, and electrolytes of varying concentrations are introduced into the cell. As ions are introduced to the interfacial region, the positive surface charge is screened. Using the Gouy-Chapman model, which has been shown to accurately characterize the interfacial potential for solid/electrolyte systems,[102, 237] the degree of this screening behavior can be understood. The Debye-Hückle length, or thickness of the double layer, can be readily calculated for CaF_2 .[113] Based on the solubility equilibrium constant of CaF_2 , which gives an equilibrium ionic strength of 9.9×10^{-4} M, this depth is 9.7 nm and is decreased to 9.6 Å by a 0.1 M ionic strength solution. The compression

of the double layer region reduces the number of electrostatically oriented interfacial water molecules, resulting in a smaller VSFS signal in this spectral region. As a consequence, water molecules most closely interacting with the surface are revealed.

Recent results from Miller *et al.*[234] found the potential of a flat CaF_2 (111) surface to be negative at pH 5.8, which would appear to be in conflict with previous VSFS studies from Becraft *et al.*[158, 161, 209–211] and Schrödle *et al.*[225–228] However, the crystallographic orientation has a significant effect on the surface charge. The isoelectric point of a (110) CaF_2 plate was recently measured by atomic force microscopy, which found the surface to be positively charged below pH 9.2. The results presented here are collected on an amorphous CaF_2 prism, which bears more similarity to the commonly used powdered CaF_2 used in traditional zeta potential measurements. These measurements have long found that CaF_2 at this pH is positively charged.[233, 234, 238, 239]

Neat CaF_2 /water spectra are shown in Figures 8.1, 8.2, 8.3, 8.5 and 8.6 as the \circ marked spectra. The spectra for all the solutions show the same general features with a large broad peak centered around 3200 cm^{-1} . This spectral region corresponds to water molecules with relatively strong bonding interactions whereas spectral features at higher frequencies ($3400\text{--}3700\text{ cm}^{-1}$) represent interfacial water molecules with weaker hydrogen bonding interactions. To facilitate the comparison of changes in spectral regions for different electrolyte containing solutions, spectral fitting routines that deconvolute the overall spectral envelope into several spectral

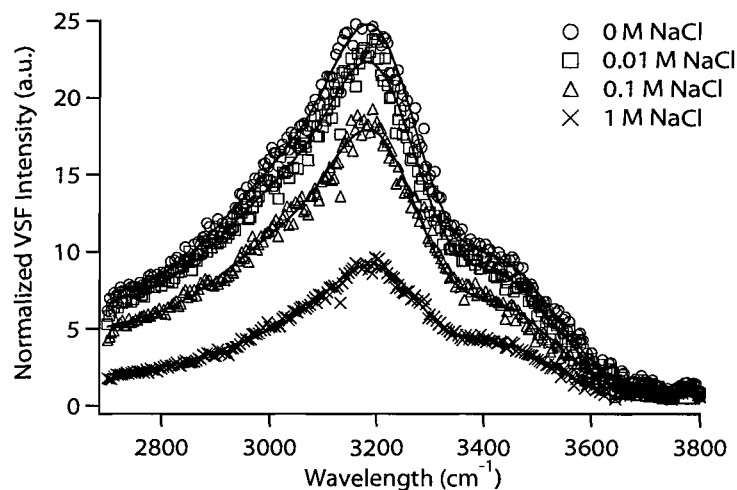


Figure 8.1. Concentration series VSFS spectra of aqueous NaCl solutions at the CaF_2 surface. Increasing the Cl^- concentration uniformly changes the intensity, but not the distribution of the VSFS spectra.

regions are employed.[63, 105] The results for the contributing peaks found from the best fits to the $\text{CaF}_2/\text{water}$ spectra are shown in Table 8.1. The differences between the fit parameters for these water spectra are primarily due to variations of the prism surface between polishings which change the VSFS spectra slightly. Because of the broadness of the reported peaks, the differences in location and amplitude are not significant.

Figure 8.1 shows the VSFS spectra of the $\text{CaF}_2/\text{NaCl}(\text{aq})$ interface as a function of ionic strength. Changes in the water spectrum were not appreciable for concentrations less than 0.001 M ionic strength. At $I = 0.01$ M, a decrease in the VSFS intensity over the whole spectral region was observed. This indicates that the predominant coordination environments at ~ 3050 , ~ 3225 and $\sim 3450 \text{ cm}^{-1}$ are equally affected by the presence of ions near the interface. The $\text{Cl}^-(\text{aq})$ anions are not particularly

Table 8.1. Spectral fitting parameters for H₂O and salt solutions at the CaF₂ surface with the following ionic strengths: $I(\text{NaCl}) = 1 \text{ M}$, $I(\text{NaBr}) = 1 \text{ M}$, $I(\text{Na}_2\text{SO}_4) = 0.1 \text{ M}$, $I(\text{NaF}) = 0.1 \text{ M}$ and $I(\text{CaCl}_2) = 1 \text{ M}$. Negative and positive amplitudes correspond to phases of π and 0, respectively. The reported errors are those of the spectral fits.

Salt	Water Spectra Parameters			Highest Concentration Parameters		
	Location (cm ⁻¹)	Width (cm ⁻¹)	Amplitude	Location (cm ⁻¹)	Width (cm ⁻¹)	Amplitude
NaCl	3059 ± 1	135 ± 2	0.93 ± 0.03	3059 ± 1	135 ± 2	0.54 ± 0.05
	3227 ± 1	114 ± 1	2.96 ± 0.02	3227 ± 1	114 ± 1	1.94 ± 0.04
	3447 ± 1	157 ± 1	2.09 ± 0.02	3447 ± 1	157 ± 1	1.55 ± 0.03
NaBr	3060 ± 1	104 ± 2	0.66 ± 0.02	3060 ± 1	104 ± 2	0.24 ± 0.03
	3232 ± 1	124 ± 1	3.14 ± 0.01	3232 ± 1	124 ± 1	1.30 ± 0.03
	3459 ± 1	159 ± 1	1.83 ± 0.02	3459 ± 1	159 ± 1	1.00 ± 0.02
Na ₂ SO ₄	3039 ± 2	87 ± 2	0.69 ± 0.02	3056 ± 15	76 ± 11	0.07 ± 0.02
	3229 ± 1	115 ± 1	2.99 ± 0.01	3254 ± 5	86 ± 12	0.20 ± 0.02
	3456 ± 1	178 ± 1	2.33 ± 0.02	3483 ± 1	258 ± 1	0.82 ± 0.02
	—	—	—	3615 ± 3	75 ± 5	-0.48 ± 0.03
NaF	3078 ± 3	102 ± 5	0.96 ± 0.11	—	—	—
	3239 ± 6	104 ± 2	3.45 ± 0.09	3225 ± 4	62 ± 5	-0.15 ± 0.01
	3449 ± 5	204 ± 10	2.9 ± 0.1	3464 ± 5	88 ± 3	0.31 ± 0.01
	—	—	—	3622 ± 2	52 ± 2	-0.64 ± 0.01
CaCl ₂	3039 ± 2	86 ± 3	1.03 ± 0.04	3090 ± 8	76 ± 11	0.20 ± 0.02
	3216 ± 1	110 ± 1	3.77 ± 0.08	3234 ± 2	80 ± 3	0.72 ± 0.02
	3417 ± 1	147 ± 1	2.4 ± 0.1	3483 ± 1	258 ± 1	0.82 ± 0.02
	—	—	—	3671 ± 5	120 ± 11	0.27 ± 0.02

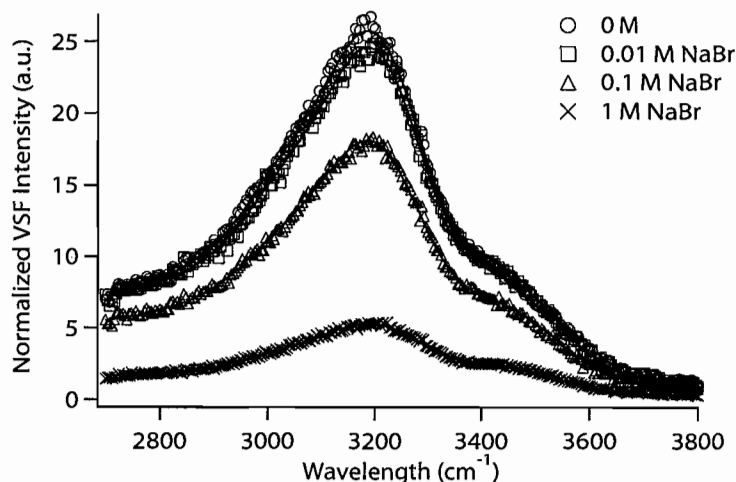


Figure 8.2. Concentration series VSFS spectra of aqueous NaBr solutions at the CaF_2 surface. Adding Br^- primarily decreases the VSFS signal, but does not greatly alter the distribution of the VSFS signal.

effective at screening the charge near the surface or altering the hydrogen bonding network, as the spectral intensity remains strong and both the locations and relative intensities of the spectral regions representing the different coordination environments remain unchanged at $I = 1 \text{ M}$. Even though both $\text{Na}^+(\text{aq})$ and $\text{Cl}^-(\text{aq})$ are considered weakly hydrated ions, the ions do not appear to form a counterion layer close to the charged CaF_2 surface that would significantly screen the surface charge, resulting in a lower water signal, and disrupt the hydrogen bonding network of the interfacial water molecules.

The NaBr solution spectra in Figure 8.2 show similar behavior at the CaF_2 surface compared to NaCl solutions. The spectra were fit to three broad peaks of constant location and width (3060 cm^{-1} , 3231 cm^{-1} and 3459 cm^{-1}), all of which decrease in amplitude with increasing Br^- concentration. Differences between Br^- and Cl^-

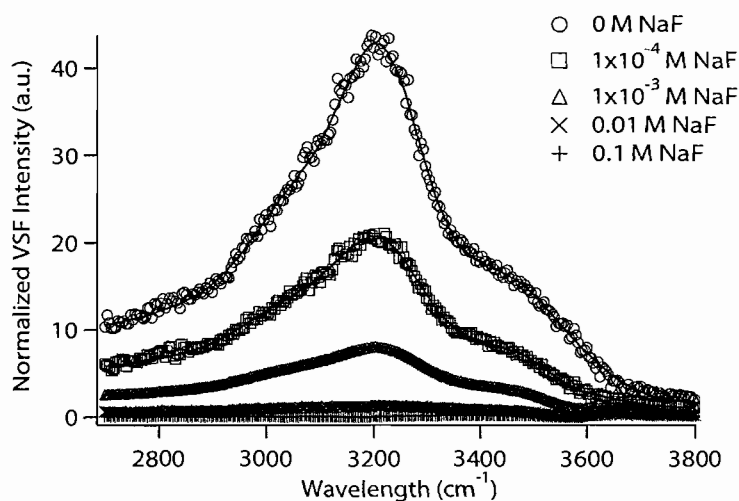


Figure 8.3. VSFS spectra of aqueous NaF solutions of different concentrations at the CaF_2 surface. Adding F^- decreases VSFS signal and changes the intensity distribution. The data for 0.1 M NaF are shown on an expanded scale in Figure 8.4

ion containing solution are negligible until 1 M ionic strength, at which point Br^- decreases the VSFS signal significantly more than Cl^- . For the three water peaks, the average peak amplitude decrease is 20 percent more for 1 M NaBr relative to 1 M NaCl. A likely explanation for this is the greater polarizability of Br^- compared to Cl^- . The greater size of Br^- allows it to be more readily distorted by the surface electric field than Cl^- , resulting in a larger induced dipole, which may increase surface attraction. However, the Br^- ions also do not appear to form dense counterion layers in the interface, as there is only a small decrease in VSFS signal at 0.1 M ionic strength and no significant changes in the best fit parameters, which would represent a change in the interfacial bonding environment.

The final monatomic ion examined was fluoride. The addition of F^- to the $\text{CaF}_2/\text{H}_2\text{O}$ interface results in distinctly different changes in the interfacial water

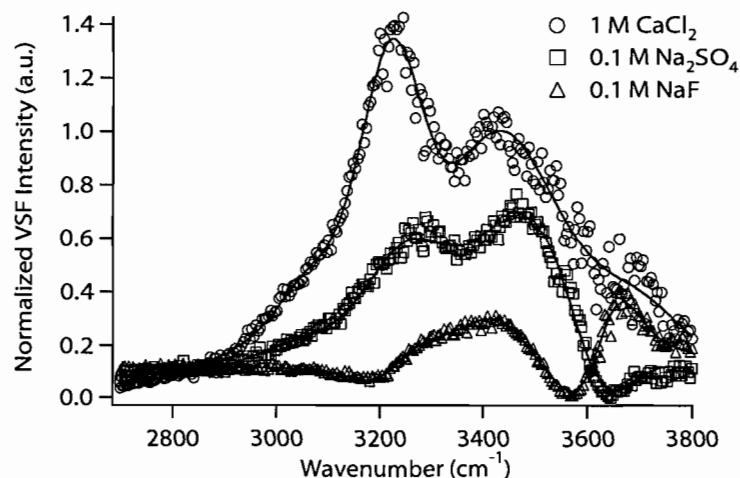


Figure 8.4. VSFS spectra of 0.1 M NaF (Δ), 0.1 M Na_2SO_4 (\diamond) and 1 M CaCl_2 (\square) solutions which show significant deviations from neat water spectra. These spectra demonstrate differences in spectral features and have not been normalized to each other.

spectra compared to Cl^- and Br^- . The interfacial water, as manifested in the VSFS intensity, is far more sensitive to the presence of added F^- than either Cl^- or Br^- . Plots of the spectra in Figure 8.3 clearly show changes with concentration. First, spectral intensity begins to decrease at 1×10^{-4} M, which is two orders of magnitude lower than for Cl^- or Br^- . Second, the overall shapes of the spectra change with increasing ionic strength. By 0.1 M ionic strength, which is shown in Figure 8.4 for clarity, the spectrum is quite different from the neat $\text{H}_2\text{O}/\text{CaF}_2$ spectrum shown in Figure 8.3. At low concentrations, the spectra can be described by three broad modes representing a range of coordination environments which are similar to those seen in the Cl^- and Br^- containing spectra. As the concentration is increased to 0.1 M, ions populate the interfacial region, further screening the surface charge,

altering the hydrogen bonding network, which can be seen by the differences in the fit parameters of water and 0.1 M NaF in Table 8.1. The result is a decrease in VSFS amplitude throughout the spectral region studied, with the largest intensity now coming from water molecules that are much more loosely coordinated. This behavior is clearly different from the other ions studied. This demonstrates that at these high concentrations of F^- , the interfacial water is significantly perturbed throughout the interfacial region by $F^- - H_2O$ interactions that alter and weaken the $H_2O - H_2O$ and $H_2O - CaF_2$ interactions. The best fit to the spectrum for 0.1 M NaF results in three peaks at 3225 cm^{-1} , 3464 cm^{-1} and 3622 cm^{-1} . The 3622 cm^{-1} peak appears at concentrations as low as 1 mM and its amplitude increases with increasing concentration. The phase of this peak is consistently opposite that of the coordinated water environments, as shown by the negative sign in front of the amplitude in Table 8.1. Because of this amplitude increase and the peak location, this mode is attributed to water molecules solvating F^- ions in the interfacial region. The phase difference between this mode and the coordinated water envelope reflects the orientation differences between water hydrating the positively charged CaF_2 surface and the negatively charged ion. This charge difference causes the direction of the water dipoles to be oppositely oriented in the two environments. Fluoride ions are known to be strongly hydrated; the reported enthalpy of solvation of F^- is $\sim 510\text{ kJ/mol}$, which is significantly higher than Cl^- or Br^- . [165] Ion solvating water molecules are commonly found in this spectral region by VSFS and are

likely due to induced asymmetry in the solvation shell of the ion as it nears the charged surface.[111, 161, 162] The small peak at 3225 cm^{-1} is unique to the highest concentration tested. This peak is attributed to water molecules hydrogen bonding with surface bound F^- ions which create local charge environments different from that of the surface overall. Microsolvation studies support these conclusions, with $\text{F}^-/\text{H}_2\text{O}$ hydrogen bonds having been seen near 3200 cm^{-1} and interwater hydrogen bonds of the ion solvation shell near 3600 cm^{-1} . [240, 241] Either or both of these species are likely present in the interface at lower concentrations than seen in the spectra, but they are masked at the lower concentrations where water molecules in the double layer region dominate the spectrum of those molecules closest to the CaF_2 surface. This is not unexpected as the solvated ion effect should be weak. Based on Gouy-Chapman theory, the charge density of the diffuse layer is 0.0061 C/m^2 and that of a F^- ion is 0.721 C/m^2 ; [112] thus solvated ions must be very close to the interfacial plane for there to be sufficient symmetry breaking to generate a signal and that signal will be weak relative to that of the electrically oriented water in the double layer.

Sulfate ions were also examined at this interface. Sulfate ions in the aqueous phase provide an interesting comparison to the other anions studied here because of their divalent character, which should lead to stronger surface bonding at the positively charged aqueous CaF_2 surface, and a tendency to form robust solvation shells.[165] Presented in Figure 8.5 are VSFS spectra that show SO_4^{2-} affects the interface at concentrations as low as $1 \times 10^{-5}\text{ M}$ by a large decrease in VSFS signal.

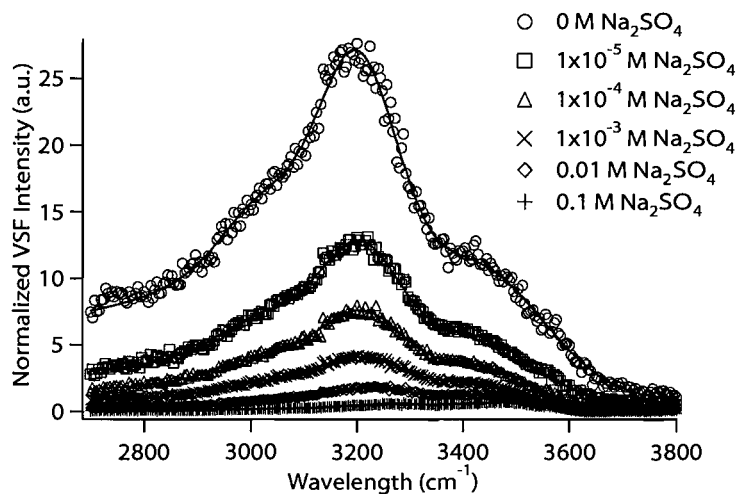


Figure 8.5. VSFS spectra of aqueous Na_2SO_4 solutions at the CaF_2 surface. SO_4^{2-} decreases the VSFS signal at low concentrations and significantly changes the VSFS spectra. The data for the $0.1 \text{ M Na}_2\text{SO}_4$ are shown on an expanded scale in Figure 8.4.

Compared to the monovalent ions, and in particular $\text{NaCl}(\text{aq})$, SO_4^{2-} ions much more effectively screen the surface charge, i.e., they have a high tendency to be located close to the interface even at low concentrations. Additionally, every SO_4^{2-} ion adsorbed at the interface compensates two positive charges and is thus able to reduce the interfacial field more than Cl^- . With regards to spectral fitting, the VSFS spectra of the Na_2SO_4 solutions show a smooth shift in fitted frequency from the values of the $\text{CaF}_2/\text{H}_2\text{O}$ spectrum to those of the $I = 0.1 \text{ M Na}_2\text{SO}_4(\text{aq})/\text{CaF}_2$ spectrum in Table 8.1. The fitting results describing the broad vibrational modes of the coordinated water environment of the highest concentration spectrum are 3056 cm^{-1} , 3554 cm^{-1} and 3483 cm^{-1} . These values are slightly blueshifted than the initial values of the pure water spectrum. This is consistent with a weakening of the $\text{H}_2\text{O}-\text{H}_2\text{O}$ interactions due to the more disruptive nature of the SO_4^{2-} ions

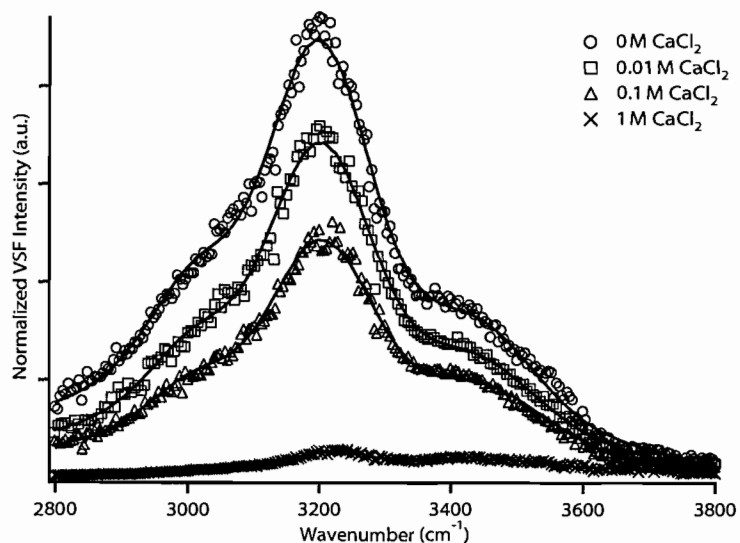


Figure 8.6. VSFS spectra of the $\text{CaF}_2/\text{CaCl}_2(\text{aq})$ interface. Concentrations are in ionic strength.

that are larger and have larger solvation shells than Cl^- or Br^- . As a comparison, the enthalpies of solvation of SO_4^{2-} , Cl^- and Br^- are -1018, -336 and -367 kJ/mol, respectively.[165] Evidence for these solvating water molecules near the surface can be found in the spectra near 3600 cm^{-1} , where significant spectral changes occur at the higher concentrations that reveal interactions closer to the surface. To account for these changes, it is necessary to add a small peak with a phase opposite that of the coordinated water regions at 3597 cm^{-1} to improve the overall fit. Water molecules solvating the ionized headgroup of sodium dodecylsulfate at the $\text{CaF}_2/\text{H}_2\text{O}$ interface have previously been seen near the same location by VSFS.[161]

To study the effect of the Ca^{2+} ion, which is always present in the aqueous phase due to the solubility equilibrium of CaF_2 , CaCl_2 solutions were also examined. While they have minimal effect on bulk pH, Ca^{2+} ions have been shown to affect the zeta

potential of CaF_2 .^[234] This means that the ions can directly interact with the surface by adding to the fluorite lattice. Because of the positive charge of the surface and the weak interaction of Cl^- ions at the interface, very little effect on the VSFS spectra can be seen until 0.01 M ionic strength (see supplemental data). The parameters of the peaks used are shown in Table 8.1 and are similar to those used for the other spectra presented here. Unlike the F^- ion spectra, there is no apparent shifting of the spectral resonances with the addition of CaCl_2 until 1 M ionic strength is reached, shown in Figure 8.6. At this point, it becomes clear that an additional broad peak is required to fit the spectra at 3672 cm^{-1} . This peak is assigned to water molecules hydrating Ca^{2+} ions, because the phase of this peak is opposite that of the solvation peak in the F^- and SO_4^{2-} ion spectra due to the positive charge of the ion. Furthermore, this frequency is close to that found for Ca^{2+} ions in infrared action spectroscopy.^[242]

Ion Kinetics at the $\text{CaF}_2/\text{Water}$ Interface

To augment the insights gained from the spectroscopic experiments, time resolved studies were performed that monitor the change in spectral intensity as a function of time after the addition of the different salts discussed previously. Two wavelengths were measured simultaneously, before and after introduction of the salt solution. The first frequency probed was 3200 cm^{-1} , which probes the strongly coordinated water molecules in the double layer and also those hydrating the surface. The second frequency chosen was 3590 cm^{-1} , which measures more weakly hydrogen bonded species including ion solvating water molecules. The VSFS signal from the $\text{CaF}_2/\text{H}_2\text{O}$

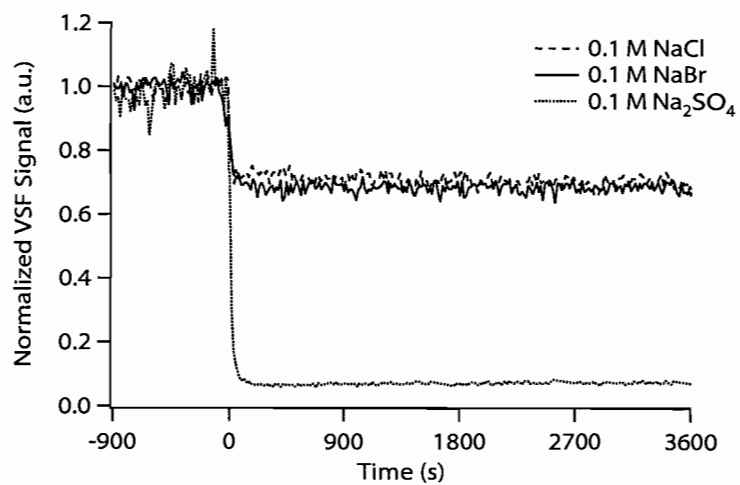
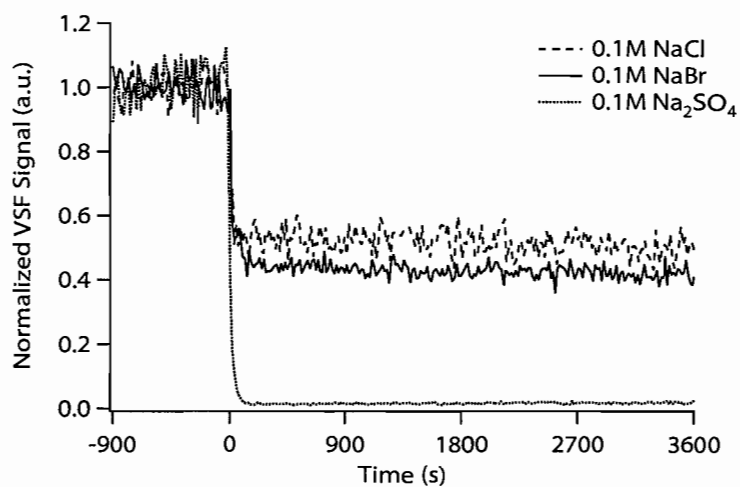
(a) 3200 cm^{-1} (b) 3590 cm^{-1}

Figure 8.7. VSFS signal at (a) 3200 cm^{-1} and (b) 3590 cm^{-1} monitored over time for NaBr, NaCl and Na_2SO_4 at $\text{CaF}_2/\text{water}$ interface. The data values are all normalized to 1 prior to the introduction of the salt solutions and $\text{time} = 0$ corresponds to the beginning of signal decay.

interface was initially allowed to stabilize, after which the desired salt solution was pumped into the cell and monitored until the signal no longer changed. Figure 8.7(a) shows the time-resolved VSFS signal for 0.1 M Cl^- , Br^- and SO_4^{2-} with the initial water signals all normalized to one. All traces show a rapid drop in intensity, on the order of a few seconds, as soon as the salt solution is introduced into the cell at time = 0 seconds. As the ions populate the interfacial region of the charged CaF_2 surface, the number of interfacial water molecules contributing to the spectral response is reduced due to screening of the interfacial potential as the ions diffuse to the interface. Beyond the rapid decrease for Cl^- , Br^- and SO_4^{2-} , the VSFS response remains relatively constant for the duration of the experiment. The traces at 3590 cm^{-1} (Figure 8.7(b)) show identical kinetics, even for the SO_4^{2-} ion, showing that the population of the solvated species tracks with the decrease in the number of water molecules.

For moderately and highly concentrated solutions of NaF, different results are obtained as shown in Figure 8.8(a) and Figure 8.8(b). Initially a fast drop in intensity is observed at both frequencies, similar to the other ions. However, this sharp decline is followed by a decrease in VSFS signal that takes about 1800-3600 seconds, which can be seen most clearly in the 0.1M traces for both wavelengths. The similarity in the intermediate decays at these two frequencies at high concentrations indicates the changes in the interfacial water in this time frame are at least influenced by the same interfacial process and possibly originate from the same source. Previous electrochemical and spectroscopic studies have made note of long time scale (tens of

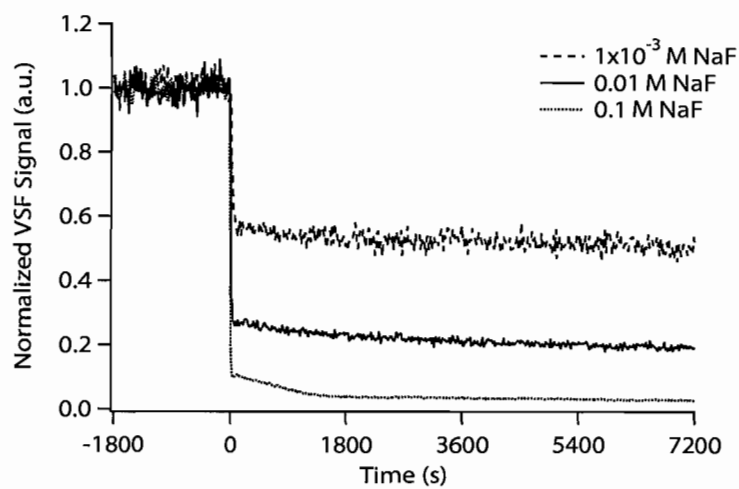
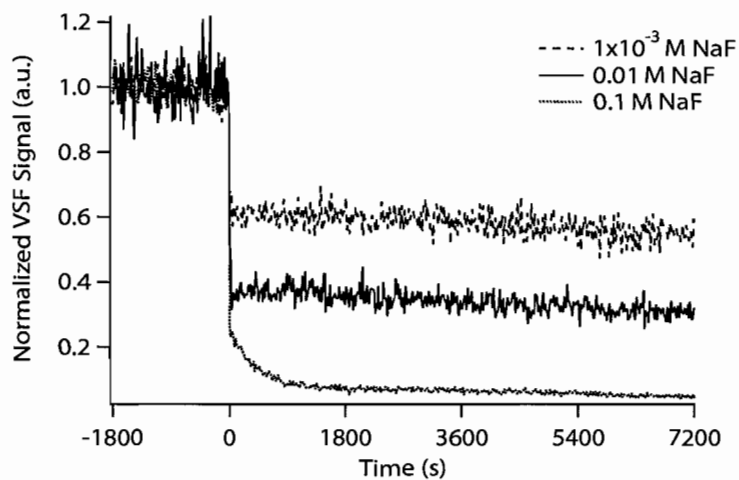
(a) 3200 cm^{-1} (b) 3590 cm^{-1}

Figure 8.8. VSFS signal at (a) 3200 cm^{-1} and (b) 3590 cm^{-1} monitored over time for three concentrations of NaF: $1 \times 10^{-3}\text{ M}$, 0.01 M and 0.1 M at $\text{CaF}_2/\text{water}$ interface. The data are all normalized to 1 and time = 1 corresponds to the beginning of signal decay

hours) instability for fluorite/water interfaces[233, 234] and attributed it to surface restructuring. However, those results were observed over a longer time scale, not the intermediate time scale phenomenon of an hour seen here. Studies over a longer time scale show small changes in the VSFS spectra, but they are difficult to decouple from instrumental drift.

Drawing from the results of the spectroscopic studies discussed above that attribute the spectral features near 3200 cm^{-1} and 3590 cm^{-1} , respectively, to water directly hydrating the CaF_2 surface with excess F^- and water solvating F^- ions in the interfacial region, changes in this intermediate time regime are caused by direct interactions between F^- and the CaF_2 surface. Unlike the other anions, F^- is a constituent of the solid CaF_2 . It has long been known that the CaF_2 surface is fluoride deficient in contact with water. Exposing such surfaces to solutions containing more than the equilibrium concentration of aqueous F^- will naturally shift the chemical equilibrium at the interface and thus affect surface speciation. Note that very strongly hydrated F^- can immediately screen surface charges when adjacent to the surface, but for direct bonding to CaF_2 sites at the surface, at least part of the hydration shell must be removed. Removing this solvation shell and displacing the surface hydration layer will slow down reactions between F^- ions and the surface, which rely on direct F^- contact.

To test these ideas further, the same experiments at 3200 cm^{-1} and 3590 cm^{-1} were performed with CaCl_2 at 0.01 M, 0.1 M and 1 M ionic strengths at pH 5.8 as shown

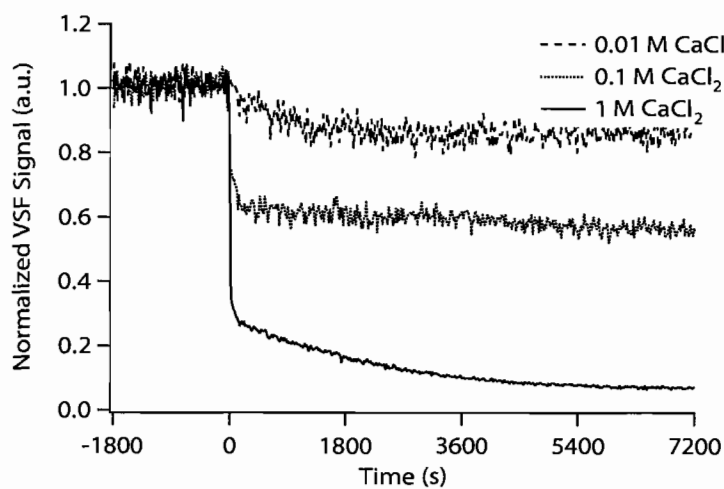
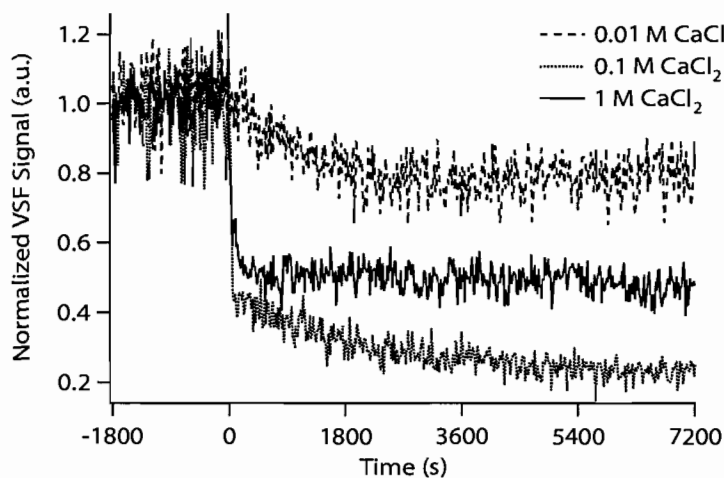
(a) 3200 cm^{-1} (b) 3590 cm^{-1}

Figure 8.9. VSFS signal at (a) 3200 cm^{-1} and (b) 3590 cm^{-1} monitored over time for three concentrations of CaCl_2 : 0.01 M, 0.1 M and 1 M at $\text{CaF}_2/\text{water}$ interface. The data are all normalized to 1 and time = 1 corresponds to the beginning of signal decay.

in Figure 8.9(a) and Figure 8.9(b). Calcium has been previously shown to be a potential determining ion for flat CaF_2 surfaces[234], meaning that it can directly interact with the surface, but have no significant effect on the zeta potential of powdered CaF_2 below 0.01 M.[238] The kinetic traces bear this out, with no significant change in the VSFS signal when the ionic strength is greater than 0.01 M. Given the strongly hydrated nature of CaF_2 , [233, 239] it might be expected that there would be a significant time lag between the introduction of Ca^{2+} ions to the interface and equilibrium due to the ions having to displace the surface bound water molecules. This is evidenced by the CaCl_2 kinetic traces at both wavelengths. The kinetic traces show two distinct signal decay processes: a rapid decrease and an intermediate time scale decay. The intermediate time scale component is most clearly apparent when the surface is exposed to the 1 M Ca^{2+} solution. The time scale of this feature, around 3600 seconds, is longer than that seen in the NaF traces. This may be due to the flow rate as solubility studies have shown that small changes in the flow rate and pH in the range from 5 to 7 can have a very large effect on the dissolution rate.[243] More likely, it is due to the electrostatically unfavorable interaction of Ca^{2+} with the positively charged surface and differences in the hydration of Ca^{2+} and F^- . Calcium ions have an absolute hydration enthalpy of $-1602 \text{ kJ mol}^{-1}$, which is significantly greater than the -510 kJ mol^{-1} of F^- . This larger enthalpy indicates a larger hydration shell that must be shed for direct interactions with the CaF_2 substrate, which may take more time than the shell of F^- . [165]

Given the similarity of the kinetic results of the F^- and Ca^{2+} , it can be concluded that these ions have similar interactions with the interface. These interactions are governed by at least two different time scale processes based on the interfacial structure. The processes are screening and direct surface interaction. The initial rapid decrease in signal is accounted for by the presence of ions in the interfacial region, which screen the surface charge and reduce the thickness of the diffuse layer in a few seconds. The second process, direct interaction, is most clearly seen in the ion kinetics studies at high concentrations which reveal the dynamics of the surface layers. This process is most likely due to the direct interactions of F^- and Ca^{2+} with the CaF_2 surface in which the ions chemically adsorb to the surface and displace hydrating water molecules and has a time scale on the order of an hour. It is evident that the decay at 3200 cm^{-1} is related to ion adsorption, as it tracks closely with the decay at 3590 cm^{-1} , which monitors the solvated ion peak. This conclusion seems to run counter to recent electrokinetic studies showing that F^- is not a potential determining ion, in which the strong hydration of CaF_2 and F^- has been used to explain the inability of F^- to reverse the zeta potential.[233, 234] However, these studies do not find an orientation reversal of the coordinated interfacial water molecules, which would be expected if F^- adsorption reversed the surface charge. Rather, there is new evidence for direct adsorption on the surface as seen by the strong presence solvated F^- at 3617 cm^{-1} , a peak that is attributed to water hydrogen bonded to surface bound F^- at 3225 cm^{-1} and a time scale component in the adsorption process similar

to that of an ion, Ca^{2+} , known to affect the zeta potential of the surface and alter the chemical equilibrium.

Conclusions

VSFS experiments in the frequency and time domains were performed to examine the behavior of aqueous Cl^- , Br^- , F^- and SO_4^{2-} at the $\text{CaF}_2/\text{H}_2\text{O}$ interface. These experiments have been performed under constant flow conditions to allow rapid changes of solution and to prevent a buildup of surface dissolution products, which have affected previous VSFS studies in this spectral region. The primary effect of the addition of Cl^- and Br^- ions is to screen the electrostatic field existing at the $\text{CaF}_2/\text{water}$ interface due to its positively charged surface. Aqueous Cl^- and Br^- slightly alter the water bonding structure with Br^- appearing to have the larger effect. This is due to the greater polarizability of Br^- relative to Cl^- . The strongly hydrated SO_4^{2-} ion has a more disruptive effect on the interfacial water-water hydrogen bonding network; solvated SO_4^{2-} ions are clearly present near the surface. Due to its greater charge, SO_4^{2-} is more effective at screening the surface charge and more strongly attracted to the interface than Cl^- or Br^- . However, the kinetic studies show that the effects of SO_4^{2-} , as well as Cl^- and Br^- , on interfacial water are primarily electrostatic in nature. The kinetic studies show a clear difference in the surface interaction of F^- relative to the other ions. The addition of F^- to the system results in both the rapid electrostatic effect of compressing the double layer as seen in Cl^- , Br^- and SO_4^{2-} and

a slower direct interaction with the mineral surface. Fluoride significantly disturbs the interface as its strong ion-water interactions disrupt the interfacial H₂O-H₂O and H₂O-CaF₂ interactions. The presence of added F⁻ shifts the solubility equilibrium of the surface, resulting in F⁻ ions possibly adding to sites on the CaF₂ lattice, shedding their own hydration shells and partially displacing the surface hydration layer. The direct interaction of F⁻ ions with the surface is supported by the VSFS spectrum of interfacial water. Based on these measurements, it is critical to control the solution concentration of F⁻ and Ca²⁺ for accurate measurements of surfactant adsorption on fluorite.

CHAPTER IX

CONCLUSIONS

The buried solid/liquid interface plays a critical role in applications from mineral flotation,[5, 158] to boundary lubrication[129, 147] and biocompatibility.[79, 124] Answering questions regarding the design of systems for these applications requires an understanding of the structures at the target interface. Surfactant adsorption in flotation is affected by the mix of aqueous ions in solution. Lubricant films must be oriented such that the molecules slide over each other and the surface. Biocompatible surfaces must be tuned to have the right degree of nonspecific and specific interactions to survive the harsh and chemically complex environment within the body.

The work within this dissertation uses experimental methods to arrive at several conclusions with applications to these kinds of questions. Methods for producing the hydrophobic surfaces were analyzed, revealing that VSFS is indirectly sensitive to the quality of self-assembled monolayers. Examination of the pH effects on the monolayers, which alters the orientation of interfacial water molecules, shows that the VSFS response of an aggregate coated layer changes significantly with interfacial charge whereas a well-formed surface is unaffected. For fluorocarbon surfaces, the monolayer modes accessible in these experiments were unaffected by differences in surface morphology, possibly due to their location at the base of the carbon chain.

Salt screening and constant ionic strength pH results on the fluorocarbon and hydrocarbon films have shown conclusive evidence for differences in the interactions of water with fluorocarbons and hydrocarbons. Directly interacting water molecules have clear spectroscopic signatures that shift with the strength of their interaction with hydrophobic surfaces. From observations on water permeation, it is clear that the water signal measured at the monolayer/water interface originates from water molecules above the interface and that the charging behavior of the FDS and ODS surfaces is due to adsorption of ions from solution.

Studies with two example organic molecules revealed that fluorocarbon and hydrocarbon surfaces interact differently with organic species as well. Shifting interfacial frequencies at fluorocarbon surfaces, similar to that seen with directly interacting water molecules, were found for organic adsorbates. This frequency shift indicates a weak direct interaction between fluorocarbons and hydrocarbons, explaining their tendency to phase separate in mixed monolayers and emulsions.[244–246] This weaker interaction leads to different molecular orientations of adsorbates at these surfaces.

Salt experiments in using combination of equilibrium and nonequilibrium VSFS measurements to reveal that calcium and fluoride ions disrupt the tightly bound surface hydration layer of CaF_2 . Equilibrium measurements show that all of the ions added screen the interfacial electrostatic field, to varying degrees. Chloride, bromide and calcium are relatively ineffective at screening the charge whereas sulfate

and fluoride compress the double layer at low concentrations. Kinetic studies reveal more detail about this behavior, showing that chloride, bromide and sulfate are only electrostatically attracted to the interface. Calcium and fluoride not only screen the interfacial charge, but actually penetrate the tightly bound layer of water on the surface, possibly adding to surface sites.

Taken together, the studies within this dissertation present a compelling picture of how aqueous adsorbate structure is dependent on the solid phase. This information would scarcely be attainable using techniques other than VSFS. The ability to directly observe interfacial species shows how they differ from the bulk and from surface to surface. Shifting frequencies, structural changes and alterations of chemical kinetics are all symptoms of direct interactions between adsorbates and solid subphases.

APPENDIX

METHANOL ORIENTATION CALCULATION

The ability to compute molecular orientation is one of the strengths of VSFS. To demonstrate this ability and justify the treatment the SSP amplitude of the $\text{CH}_3(\text{ss})$ as directly proportional to the number of molecules adsorbed, the polar orientation of methanol is calculated here.

The first step in making this calculation is to normalize and fit the VSFS spectra, the methods for this are discussed in Chapter III. Once the spectra have been processed and broken into resonant components, both the amplitude and wavelength are used to compute the orientation.

The second step is to take the wavelength and compute the Fresnel coefficients for that wavelength. As seen in Equation II.7, the intensity of VSFS spectra is dependent on these factors and their computation is nontrivial. Because methanol and water have significantly different refractive indices, the refractive index of the solution varies with composition. Thus, the first step is to compute the solution bulk refractive index using the Lorentz-Lorenz relation for a two component mixture, as shown below in Equation A.1.

$$\frac{n^2 - 1}{n^2 + 2} \frac{M}{\rho} = \frac{n_{d2o}^2 - 1}{n_{d2o}^2 + 2} \frac{f_{d2o} M_{d2o}}{\rho_{d2o}} + \frac{n_{meod}^2 - 1}{n_{meod}^2 + 2} \frac{f_{meod} M_{meod}}{\rho_{meod}} \quad (\text{A.1})$$

In this expression terms have the following meanings: n is the solution refractive

index, M is the molecular mass, ρ is the density, f is the mole fraction and V is the molar volume. The subscripts refer to the particular solution component CH₃OD or D₂O. If unlabeled, they refer to the solution itself. The quantity M can be calculated by the relation $M = f_{d2o}M_{d2o} + f_{meod}M_{meod}$ and ρ can be measured in the laboratory. The refractive indices of deuterated methanol and D₂O are available in the literature.[247, 248]

Equation A.1 is used to compute the solution refractive index at all wavelengths in the system, VSFS, visible and IR for each solution; $n_{solution,VSF}$, $n_{solution,vis}$ and $n_{solution,IR}$, respectively. For this particular case, the imaginary component of the refractive index was ignored for the VSFS and visible light because they are very small.

The next step is to choose a model for the interfacial refractive index as the refractive index is not the same as either the solution bulk or the solid phase. A common approach to this is to assume the interfacial refractive index at a given wavelength is the average of the two bulk refractive indices. A better approach was developed by Zhuang et al. by computing the components of the an electric field perpendicular and parallel to the interface[249] which has been extended from the air/liquid interface to the solid/liquid interface below.

$$n_{int} = \frac{\sqrt{n_{solution}^4 - n_{solution}^2 n_{sio2}^2 - 6n_{solution}^4 n_{sio2}^2}}{\sqrt{-2n_{solution}^2 + 2n_{sio2}^2 - 6n_{solution}^2 n_{sio2}^2}} \quad (A.2)$$

Once again, the subscript refers to the solution phase or the fused silica substrate. It is important to note that no express consideration has been made for the presence of

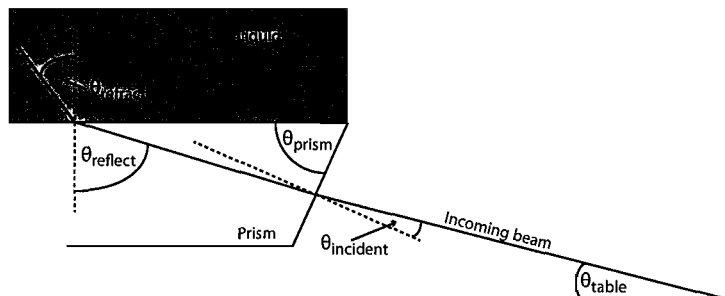


Figure A.1. Diagram of VSFS experiment geometry used to define the beam angles. The different beams have different indices, e.g. IR or vis attached to their symbols.

the organosilane monolayer, which has some effect on the refractive index. However, this layer is very thin and the internal reflection geometry is set for SiO_2 in the experiment such that the refracted angles are unaffected by the monolayer within the accuracy of the experiment. The interfacial refractive index is calculated using the above relation for each of the three beams in the experiment.

Having calculated the interfacial refractive index, it is now necessary to compute the angles at the interface. Because the input beams are somewhat refracted by their incidence with the prism, it is necessary to convert from the measured beam angles, which are relative to the optical table to angles relative to the prism face. The model for this is shown in Figure A.1. This angular conversion is done first by converting Θ_{Table} into an angle relative to the prism face, $\theta_{incident}$:

$$\theta_{incident} = \pi/2 - \theta_{Table} - \theta_{prism} \quad (\text{A.3})$$

$\theta_{incident}$ is then converted to an angle relative to the interface normal, $\theta_{reflect}$ by the equations below for the IR and visible beams:

$$\theta_{IR,reflect} = \sin^{-1} \left[\frac{n_{air,IR} \sin \theta_{IR,incident}}{n_{sio2,IR}} \right] + \theta_{prism} \quad (A.4)$$

$$\theta_{vis,reflect} = \sin^{-1} \left[\frac{n_{air,vis} \sin \theta_{vis,incident}}{n_{sio2,vis}} \right] + \theta_{prism} \quad (A.5)$$

The angle of the generated VSFS beam is computed using the angles of the IR and visible beams; $\theta_{IR,reflect}$ and $\theta_{vis,reflect}$, respectively, using the nonlinear version of Snell's law where ν is the frequency of light and the indices indicate which beam.

$$\theta_{VSF,reflect} = \sin^{-1} \left[\frac{\nu_{vis} n_{sio2,vis} \sin \theta_{vis,reflect} + \nu_{IR} n_{sio2,IR} \sin \theta_{IR,reflect}}{\nu_{VSF} n_{sio2,VSF}} \right] \quad (A.6)$$

The angles of the refracted beams are then computed for the interface using the interfacial angles in Equations A.4 through A.6 using Snell's law as shown in A.9. These angles are $\Theta_{VSF,refract}$, $\Theta_{vis,refract}$ and $\Theta_{IR,refract}$. They are necessary to account for the losses to the interface.

$$\theta_{IR,refract} = \frac{\sin^{-1} [n_{IR,sio2} \sin \theta_{IR,reflect}]}{n_{IR,solution}} \quad (A.7)$$

$$\theta_{vis,refract} = \frac{\sin^{-1} [n_{vis,sio2} \sin \theta_{vis,reflect}]}{n_{vis,solution}} \quad (A.8)$$

$$\theta_{VSF,refract} = \frac{\sin^{-1} [n_{VSF,sio2} \sin \theta_{VSF,reflect}]}{n_{VSF,solution}} \quad (A.9)$$

Having computed the refractive indices and angles of the reflected and refracted beams, the Fresnel coefficients can be calculated. The formulations of the Fresnels used here is from Zhuang et al.:[249] however, the different formulations in the literature lead to only slight variations in the results.

$$L_{xx,IR} = \frac{2n_{sio2,IR} \cos \theta_{IR,refract}}{n_{sio2,IR} \cos \theta_{IR,refract} + n_{solution,IR} \cos \theta_{IR,reflect}} \quad (A.10)$$

$$L_{yy,IR} = \frac{2n_{sio2,IR} \cos \theta_{IR,reflect}}{n_{sio2,IR} \cos \theta_{IR,reflect} + n_{solution,IR} \cos \theta_{IR,refract}} \quad (A.11)$$

$$L_{zz,IR} = \frac{2n_{solution,IR} \cos \theta_{IR,reflect}}{n_{sio2,IR} \cos \theta_{IR,refract} + n_{solution,IR} \cos \theta_{IR,reflect}} \left(\frac{n_{sio2,IR}}{n_{int,IR}} \right)^2 \quad (A.12)$$

The Fresnel factors are then computed for each wavelength used and are entered into the amplitude equations. In the case of methanol, no VSFS of the CH₃(ss) was detected in SPS, so we only need to use the VSF amplitudes, F_{ssp} and F_{ppp} , not intensity, for SSP and PPP. These are given in reference [92].

$$F_{ssp} = A_{yyz} L_{yy,VSF} L_{yy,vis} L_{zz,IR} \sin \theta_{IR,reflect} \quad (A.13)$$

$$\begin{aligned} F_{ppp} = & \sin(\theta_{VSF,reflect}) L_{zz,VSF} A_{zzz} \sin(\theta_{vis,reflect}) L_{zz,vis} \sin(\theta_{IR,reflect}) L_{zz,IR} \\ & + \sin(\theta_{VSF,reflect}) L_{zz,VSF} A_{zzx} \cos(\theta_{vis,reflect}) L_{xx,vis} \cos(\theta_{IR,reflect}) L_{xx,IR} \\ & - \cos(\theta_{VSF,reflect}) L_{xx,VSF} \cos(\theta_{vis,reflect}) L_{xx,vis} \sin(\theta_{IR,reflect}) L_{zz,IR} A_{xxz} \\ & - \cos(\theta_{VSF,reflect}) L_{xx,VSF} A_{zzx} \sin(\theta_{vis,reflect}) L_{zz,vis} \cos(\theta_{IR,reflect}) L_{xx,IR} \quad (A.14) \end{aligned}$$

A_{ijk} are the nonvanishing tensor elements of $\chi^{(2)}$. Assuming a delta function distribution of the polar angle of the methyl C_3 symmetry axis to the surface normal, Θ , the microscopic elements of the hyperpolarizability, β can be related to the macroscopic elements as shown below:[55]

$$A_{yyz} = A_{xxz} = \frac{\beta_{zzz}}{2} N \left[\left(\frac{\beta_{xxz}}{\beta_{zzz}} + 1 \right) \cos \Theta + \left(\frac{\beta_{xxz}}{\beta_{zzz}} - 1 \right) \cos^3 \Theta \right] \quad (\text{A.15})$$

$$A_{xzx} = A_{zxx} = \frac{\beta_{zzz}}{2} N \left(1 - \frac{\beta_{xxz}}{\beta_{zzz}} \right) (\cos \Theta + \cos^3 \Theta) \quad (\text{A.16})$$

$$A_{zzz} = \beta_{zzz} N \left[\frac{\beta_{xxz}}{\beta_{zzz}} \cos \Theta - \left(\frac{\beta_{xxz}}{\beta_{zzz}} - 1 \right) \cos^3 \Theta \right] \quad (\text{A.17})$$

N is the effective surface number density of methyl groups contributing the VSFS intensity. Raman and VSFS measurements have found the depolarization ratio, $\beta_{xxz}/\beta_{zzz} \approx 1.7$. [55, 250] Substituting Equations A.15- A.17 into Equation A.14 and taking the square root of the fit amplitude ratio allows Θ to be solved for. When this is done, the average polar angle was found to be $60 \pm 3^\circ$ over the concentration range examined. The consistency of this orientation shown that the amplitude of the SSP polarized VSFS signal is directly proportional to the number of interfacial molecules and can be used to construct an adsorption isotherm.

The calculated orientation angled deviates significantly from those found in the literature of methanol at air [60, 187], fused silica [185] and at ODS [92] interfaces, but is primarily determined by the experimental ratio of SSP to PPP, which is highly reproducible across numerous samples. The only parameter that significantly affects the outcome of this calculation are the refractive indices. The Lorentz-Lorenz relation is widely applied to calculate the refractive index of mixtures and is probably not the source of error. Likely, the calculated interfacial refractive indices are wrong; if they values are lowered slightly to below 1.3, the computed orientation angles

align well with those in the literature. It is highly likely that the FDS monolayer has a significantly lower refractive index than SiO_2 ; fluorocarbon liquids such as perfluorohexane have visible light refractive indices near 1.25.

BIBLIOGRAPHY

- [1] Sanders, J. E.; Greve, J. M.; Mitchell, S. G., S. B. and Zachariah *Journal of Rehabilitation Research and Development* **1998**, *35*, 161–176.
- [2] Langmuir, I. *Journal of the American Chemical Society* **1917**, *39*, 1848–1906.
- [3] Fuerstenau, D. W. *Transactions of the American Institute of Mining, Metallurgical and Petroleum Engineers* **1957**, *208*, 1365–1367.
- [4] Chernyshova, I. V.; Rao, K. H.; Vidyadhar, A.; Shchukarev, A. V. *Langmuir* **2000**, *16*, 8071–8084.
- [5] Fa, K. Q.; Tao, J. A.; Nalaskowski, J.; Miller, J. D. *Langmuir* **2003**, *19*, 10523–10530.
- [6] Lei, R. Z.; Gellman, A. J.; McFadden, C. F. *Langmuir* **2001**, *17*, 6240–6247.
- [7] Liu, H.; Bhushan, B. *Ultramicroscopy* **2003**, *97*, 321–340.
- [8] Frechette, J.; Maboudian, R.; Carraro, C. *Journal of Microelectromechanical Systems* **2006**, *15*, 737–744.
- [9] Shafrin, E. G.; Zisman, W. A. *Journal of Physical Chemistry* **1962**, *66*, 740, Contact Angle.
- [10] Shafrin, E. G.; Zisman, W. A. *Journal of Physical Chemistry* **1957**, *61*, 1046, Contact Angle.
- [11] Ellison, A. H.; Zisman, W. A. *Journal of Physical Chemistry* **1954**, *58*, 260–265, Contact angle.
- [12] Ellison, A. H.; Fox, H. W.; Zisman, W. A. *Journal of Physical Chemistry* **1953**, *57*, 622–627, Contact Angle.
- [13] Bhushan, B.; Cheng, Y. P. *Journal of Applied Physics* **1997**, *81*, 5390–5392.
- [14] Yoshino, N.; Yamauchi, T.; Kondo, Y.; Kawase, T.; Teranaka, T. *Reactive and Functional Polymers* **1998**, *37*, 271–282.

- [15] Mayer, T. M.; de Boer, M. P.; Shinn, N. D.; Clews, P. J.; Michalske, T. A. *Journal of Vacuum Science & Technology B* **2000**, *18*, 2433–2440.
- [16] Barriet, D.; Lee, T. R. *Current Opinion In Colloid & Interface Science* **2003**, *8*, 236–242.
- [17] Kamitani, K.; Teranishi, T. *Journal of Sol-Gel Science and Technology* **2003**, *26*, 823–825.
- [18] Ashurst, W. R.; Carraro, C.; Maboudian, R. *IEEE Transactions on Device and Materials Reliability* **2003**, *3*, 173–178.
- [19] Yamauchi, A.; Togami, K.; Chaudry, A. M.; El Sayed, A. M. *Journal of Membrane Science* **2005**, *249*, 119–126.
- [20] Tao, Z. H.; Bhushan, B. *Wear* **2005**, *259*, 1352–1361.
- [21] Massa, T. M.; Yang, M. L.; Ho, J. Y. C.; Brash, J. L.; Santerre, J. P. *Biomaterials* **2005**, *26*, 7367–7376.
- [22] Hoque, E.; DeRose, J. A.; Hoffmann, P.; Bhushan, B.; Mathieu, H. J. *Journal of Chemical Physics* **2007**, *126*, 114706.
- [23] Klein, E.; Kerth, P.; Lebeau, L. *Biomaterials* **2008**, *29*, 204–214.
- [24] Wang, D.; Oleschuk, R. D.; Horton, J. H. *Langmuir* **2008**, *24*, 1080–1086.
- [25] LeGrange, J. D.; Markham, J. L.; Kurkjian, C. R. *Langmuir* **1993**, *9*, 1749–1753.
- [26] Parikh, A. N.; Allara, D. L.; Azouz, I. B.; Rondelez, F. *Journal of Physical Chemistry* **1994**, *98*, 7577–7590.
- [27] Tripp, C.; Hair, M. *Langmuir* **1995**, *11*, 1215–1219.
- [28] Allara, D. L.; Parikh, A. N.; Rondelez, F. *Langmuir* **1995**, *11*, 2357–2360.
- [29] Parikh, A. N.; Schivley, M. A.; Koo, E.; Seshadri, K.; Aurentz, D.; Mueller, K.; Allara, D. L. *Journal of the American Chemical Society* **1997**, *119*, 3135–3143.
- [30] Fadeev, A. Y.; McCarthy, T. J. *Langmuir* **1999**, *15*, 3759–3766.
- [31] Bunker, B. C.; Carpick, R. W.; Assink, R. A.; Thomas, M. L.; Hankins, M. G.; Voigt, J. A.; Sipola, D.; de Boer, M. P.; Gulley, G. L. *Langmuir* **2000**, *16*, 7742–7751.
- [32] Liu, Y.; Wolf, L. K.; Messmer, M. C. *Langmuir* **2001**, *17*, 4329–4335.

- [33] Hozumi, A.; Sugimura, H.; Yokogawa, Y.; Kameyama, T.; Takai, O. *Colloids and Surfaces, A: Physicochemical and Engineering Aspects* **2001**, *182*, 257–261.
- [34] Henry, M. C.; Wolf, L. K.; Messmer, M. C. *Journal of Physical Chemistry B* **2003**, *107*, 2765–2770.
- [35] Wang, Y. L.; Lieberman, M. *Langmuir* **2003**, *19*, 1159–1167.
- [36] Sagiv, J. *Journal of the American Chemical Society* **1980**, *102*, 92–98.
- [37] Gun, J.; Iscovici, R.; Sagiv, J. *Journal of Colloid and Interface Science* **1984**, *101*, 201–213.
- [38] Maoz, R.; Sagiv, J. *Journal of Colloid and Interface Science* **1984**, *100*, 465–496.
- [39] Sagiv, J.; Maoz, R. *Journal of Colloid and Interface Science* **1984**, *100*, 465–495, Monolayer structure.
- [40] Gun, J.; Sagiv, J. *Journal of Colloid and Interface Science* **1986**, *112*, 457–472.
- [41] Guyot-Sionnest, P.; Hunt, J. H.; Shen, Y. R. *Physical Review Letters* **1987**, *59*, 1597–.
- [42] Zhu, X. D.; Suhr, H.; Shen, Y. R. *Physical Review B: Condensed Matter and Materials Physics* **1987**, *35*, 3047–.
- [43] Guyot-Sionnest, P.; Superfine, R.; Hunt, J. H.; Shen, Y. R. *Chemical Physics Letters* **1988**, *144*, 1–5.
- [44] Shen, Y. *Nature* **1989**, *337*, 519–525.
- [45] Bain, C. D. *Journal of the Chemical Society, Faraday Transactions* **1995**, *91*, 1281–96.
- [46] Richmond, G. L. *Chemical Reviews* **2002**, *102*, 2693–2724.
- [47] Lambert, A. G.; Davies, P. B.; Neivandt, D. J. *Applied Spectroscopy Reviews* **2005**, *40*, 103–145.
- [48] Shen, Y. R. *The Principles of Nonlinear Optics*; John Wiley: New York, 1984.
- [49] Miranda, P. B.; Shen, Y. R. *Journal of Physical Chemistry B* **1999**, *103*, 3292–3307.
- [50] Hopkins, A. J.; McFearin, C. L.; Richmond, G. L. *Current Opinion In Solid State & Materials Science* **2005**, *9*, 19–27.

- [51] Bloembergen, N.; Pershan, P. S. *Physical Review* **1962**, *128*, 606–.
- [52] Zhao, X. L.; Ong, S. W.; Eisenthal, K. B. *Chemical Physics Letters* **1993**, *202*, 513–520.
- [53] Gragson, D. E.; McCarty, B. M.; Richmond, G. L. *Journal of the American Chemical Society* **1997**, *119*, 6144–6152.
- [54] Gragson, D. E.; Richmond, G. L. *Journal of the American Chemical Society* **1998**, *120*, 366–375.
- [55] Lobau, J.; Wolfrum, K. *Journal of the Optical Society of America B-Optical Physics* **1997**, *14*, 2505–2512, Article.
- [56] Yang, Y. J.; Pizzolatto, R. L.; Messmer, M. C. *Journal of the Optical Society of America B-optical Physics* **2000**, *17*, 638–645.
- [57] Hayes, P. L.; Chen, E. H.; Achtyl, J. L.; Geiger, F. M. *Journal of Physical Chemistry A* **2009**, *113*, 4269–4280.
- [58] Hirose, C.; Akamatsu, N.; Domen, K. *Applied Spectroscopy* **1992**, *46*, 1051–1072.
- [59] Hirose, C.; Yamamoto, H.; Akamatsu, N.; Domen, K. *Journal of Physical Chemistry* **1993**, *97*, 10064–10069.
- [60] Wolfrum, K.; Graener, H.; Laubereau, A. *Chemical Physics Letters* **1993**, *213*, 41–46.
- [61] Chen, H.; Gan, W.; Wu, B.-h.; Wu, D.; Guo, Y.; Wang, H.-f. *Journal of Physical Chemistry B* **2005**, *109*, 8053–8063.
- [62] Ji, N.; Ostroverkhov, V.; Chen, C. Y.; Shen, Y. R. *Journal of the American Chemical Society* **2007**, *129*, 10056–+.
- [63] Bain, C. D.; Davies, P. B.; Ong, T. H.; Ward, R. N.; Brown, M. A. *Langmuir* **1991**, *7*, 1563–1566.
- [64] Goates, S. R.; Schofield, D. A.; Bain, C. D. *Langmuir* **1999**, *15*, 1400–1409.
- [65] Herminghaus, S. *Journal of Physics: Condensed Matter* **2005**, *17*, S261.
- [66] Young, T. *Philosophical Transactions of the Royal Society of London* **1805**, *95*, 65–87.
- [67] Cassie, A. B. D. *Discussions of the Faraday Society* **1948**, *3*, 11–16.

- [68] Acosta, E.; Mesbah, A.; Tsui, T. *Journal of Surfactants and Detergents* **2006**, *9*, 367–376.
- [69] Ikonen, M.; Murtomki, L.; Kontturi, K. *Colloids and Surfaces B: Biointerfaces* **2009**, *71*, 107–112.
- [70] Li, X. Q.; Messmer, M. C. *Journal of Chromatography A* **2003**, *984*, 19–28.
- [71] Ohnishi, S.; Ishida, T.; Yaminsky, V. V.; Christenson, H. K. *Langmuir* **2000**, *16*, 2722–2730.
- [72] Tambe, N. S.; Bhushan, B. *Nanotechnology* **2005**, *16*, 1549–1558.
- [73] de Gennes, P. G. *Reviews of Modern Physics* **1985**, *57*, 827–863.
- [74] Janssen, D.; De Palma, R.; Verlaak, S.; Heremans, P.; Dehaen, W. *Thin Solid Films* **2006**, *515*, 1433–1438.
- [75] Stalder, A. F.; Kulik, G.; Sage, D.; Barbieri, L.; Hoffmann, P. *Colloids and Surfaces, A: Physicochemical and Engineering Aspects* **2006**, *286*, 92–103.
- [76] Coelho, M. A. N.; Vieira, E. P.; Motschmann, H.; Moehwald, H.; Thuenemann, A. F. *Langmuir* **2003**, *19*, 7544–7550.
- [77] Sethuraman, A.; Belfort, G. *Biophysical Journal* **2005**, *88*, 1322–1333.
- [78] Balamurugan, S.; Ista, L. K.; Yan, J.; Lopez, G. P.; Fick, J.; Himmelhaus, M.; Grunze, M. *Journal of the American Chemical Society* **2005**, *127*, 14548–14549.
- [79] Guo, Z.; Meng, S.; Zhong, W.; Du, Q. G.; Chou, L. L. *Applied Surface Science* **2009**, *255*, 6771–6780.
- [80] Maboudian, R.; Carraro, C. *Annual Review of Physical Chemistry* **2004**, *55*, 35–54.
- [81] Kasai, T.; Bhushan, B.; Kulik, G.; Barbieri, L.; Hoffmann, P. *Journal of Vacuum Science & Technology B* **2005**, *23*, 995–1003.
- [82] Lorenz, C. D.; Chandross, M.; Grest, G. S.; Stevens, M. J.; Webb, I., Edmund B. *Langmuir* **2005**, *21*, 11744–11748.
- [83] Khatri, O. P.; Biswas, S. K. *Journal of Physical Chemistry C* **2007**, *111*, 2696–2701.
- [84] DeRose, J. A.; Hoque, E.; Bhushan, B.; Mathieu, H. J. *Surface Science* **2008**, *602*, 1360–1367.

- [85] Silberzan, P.; Leger, L.; Ausserre, D.; Benattar, J. J. *Langmuir* **1991**, *7*, 1647–1651.
- [86] McGovern, M. E.; Kallury, K. M. R.; Thompson, M. *Langmuir* **1994**, *10*, 3607–3614.
- [87] Chow, B. C.; Ehler, T. T.; Furtak, T. E. *Applied Physics B: Lasers and Optics* **2002**, *74*, 395.
- [88] Du, Q.; Freysz, E.; Shen, Y. R. *Science* **1994**, *264*, 826–828, Article.
- [89] Ye, S.; Nihonyanagi, S.; Uosaki, K. *Physical Chemistry Chemical Physics* **2001**, *3*, 3463–3469.
- [90] Nihonyanagi, S.; Ye, S.; Uosaki, K. *Electrochimica Acta* **2001**, *46*, 3057–3061.
- [91] Henry, M. C.; Piagessi, E. A.; Zesotarski, J. C.; Messmer, M. C. *Langmuir* **2005**, *21*, 6521–6526.
- [92] Liu, W.-T.; Zhang, L.; Shen, Y. R. *Journal of Chemical Physics* **2006**, *125*, 144711/1–144711/6.
- [93] Zhang, L. N.; Liu, W. T.; Shen, Y. R.; Cahill, D. G. *Journal of Physical Chemistry C* **2007**, *111*, 2069–2076.
- [94] Dove, P. M.; Rimstidt, J. D. Silica-Water Interactions. In *Silica: Physical Behavior, Geochemistry, and Materials Applications*; Heany, P. J., Prewitt, C. T., Gibbs, G. V., Eds.; Mineralogical Society of America: Washington, D. C., 1994; Vol. 29, p 259.
- [95] Pizzolatto, R. L.; Yang, Y. J.; Wolf, L. K.; Messmer, M. C. *Analytica Chimica Acta* **1999**, *397*, 81–92.
- [96] Walba, D. M.; Liberko, C. A.; Korblova, E.; Farrow, M.; Furtak, T. E.; Chow, B. C.; Schwartz, D. K.; Freeman, A. S.; Douglas, K.; Williams, S. D.; Klitnick, A. F.; Clark, N. A. *Liquid Crystals* **2004**, *31*, 481–489.
- [97] Lane, J. M. D.; Chandross, M.; Lorenz, C. D.; Stevens, M. J.; Grest, G. S. *Langmuir* **2008**, *24*, 5734–5739.
- [98] Tian, C. S.; Shen, Y. R. *Proceedings of the National Academy of Sciences of the United States of America* **2009**, *106*, 15148–15153.
- [99] Scatena, L. F.; Brown, M. G.; Richmond, G. L. *Science* **2001**, *292*, 908–912.
- [100] Raymond, E. A.; Tarbuck, T. L.; Richmond, G. L. *Journal of Physical Chemistry B* **2002**, *106*, 2817–2820.

- [101] Zhao, X. L.; Kopelman, R. *Journal of Physical Chemistry* **1996**, *100*, 11014–11018.
- [102] Ong, S.; Zhao, X.; Eisenthal, K. B. *Chemical Physics Letters* **1992**, *191*, 327–335.
- [103] Tripp, C. P.; Hair, M. L. *Langmuir* **1992**, *8*, 1120–1126.
- [104] Bascom, W. D. *Journal of Physical Chemistry* **1972**, *76*, 3188–3192.
- [105] Scatena, L. F.; Richmond, G. L. *Journal of Physical Chemistry B* **2001**, *105*, 11240–11250.
- [106] Sugimura, H.; Hozumi, A.; Kameyama, T.; Takai, O. *Surface and Interface Analysis* **2002**, *34*, 550–554.
- [107] Hore, D. K.; Beaman, D. K.; Richmond, G. L. *Journal of the American Chemical Society* **2005**, *127*, 9356–9357.
- [108] Dominguez, H.; Berkowitz, M. L. *Journal of Physical Chemistry B* **2000**, *104*, 5302–5308.
- [109] Schweighofer, K. J.; Essmann, U.; Berkowitz, M. *Journal of Physical Chemistry B* **1997**, *101*, 3793–3799.
- [110] Park, S. H.; Carignano, M. A.; Nap, R. J.; Szleifer, I. *Soft Matter* **2010**, *6*, 1644–1654.
- [111] Raymond, E. A.; Richmond, G. L. *Journal of Physical Chemistry B* **2004**, *108*, 5051–5059.
- [112] Lyklema, J. *Fundamentals of interface and colloid science*; Academic Press, 1995; Vol. 2.
- [113] Adamson, A. W.; Gast, A. P. *Physical Chemistry of Surfaces*, 6th ed.; John Wiley & Sons: New York, NY, 1997.
- [114] Walker, S. L.; Bhattacharjee, S.; Hoek, E. M. V.; Elimelech, M. *Langmuir* **2002**, *18*, 2193–2198.
- [115] Behrens, S. H.; Grier, D. G. *Journal of Chemical Physics* **2001**, *115*, 6716–6721.
- [116] *Handbook of Chemistry and Physics*, 76th ed.; Lide, D. R., Ed.; CRC Press: Boca Raton, FL, 1995.
- [117] Ulman, A.; Eilers, J. E.; Tillman, N. *Langmuir* **1989**, *5*, 1147–1152.

- [118] Gibbs, G. V.; Hill, F. C.; Boisen Jr., M. B. *Physics and Chemistry of Minerals* **1997**, *24*, 167–178.
- [119] Chen, P. J.; Rodger, D. C.; Humayun, M. S.; Tai, Y. C. *Journal of Microelectromechanical Systems* **2008**, *17*, 1352–1361.
- [120] Yu, H. Y.; Ai, L. S.; Rouhanizadeh, M.; Patel, D.; Kim, E. S.; Hsiai, T. K. *Journal of Microelectromechanical Systems* **2008**, *17*, 1178–1186.
- [121] Hassler, C.; von Metzen, R. P.; Ruther, P.; Stieglitz, T. *Journal of Biomedical Materials Research Part B-applied Biomaterials* **2010**, *93B*, 266–274.
- [122] Butterwick, A.; Huie, P.; Jones, B. W.; Marc, R. E.; Marmor, M.; Palanker, D. *Experimental Eye Research* **2009**, *88*, 22–29.
- [123] Hsu, J. M.; Rieth, L.; Normann, R. A.; Tathireddy, P.; Solzbacher, F. *IEEE Transactions on Biomedical Engineering* **2009**, *56*, 23–29.
- [124] Wasikiewicz, J. M.; Roohpour, N.; Paul, D.; Grahn, M.; Ateh, D.; Rehman, I.; Vadgama, P. *Applied Surface Science* **2008**, *255*, 340–343.
- [125] Hsu, J. M.; Rieth, L.; Kammer, S.; Orthner, M.; Solzbacher, F. *Sensors and Materials* **2008**, *20*, 87–102.
- [126] Sharifi, H.; Lahiji, R. R.; Lin, H. C.; Ye, P. D.; Katehi, L. P. B.; Mohammadi, S. *IEEE Transactions on Advanced Packaging* **2009**, *32*, 84–92.
- [127] Kasai, P. H.; Raman, V. *Tribology Letters* **2003**, *15*, 15–28.
- [128] Parker, E. E.; Ashurst, W. R.; Carraro, C.; Maboudian, R. *Journal of Microelectromechanical Systems* **2005**, *14*, 947–953.
- [129] Khatri, O. P.; Math, S.; Bain, C. D.; Biswas, S. K. *Journal of Physical Chemistry C* **2007**, *111*, 16339–16344.
- [130] Kasai, P. H.; Raman, V. *Tribology Letters* **2004**, *16*, 29–36.
- [131] Sano, H.; Maeda, H.; Ichii, T.; Murase, K.; Noda, K.; Matsushige, K.; Sugimura, H. *Langmuir* **2009**, *25*, 5516–5525.
- [132] Tao, Z. H.; Bhushan, B. *Langmuir* **2005**, *21*, 2391–2399.
- [133] Genzer, J.; Efimenko, K.; Fischer, D. A. *Langmuir* **2002**, *18*, 9307–9311.
- [134] Liu, R. C. W.; Cantin, S.; Perrot, F.; Winnik, F. M. *Polymers for Advanced Technologies* **2006**, *17*, 798–803.

- [135] Trimbach, D. C.; Keller, B.; Bhat, R.; Zankovych, S.; Pohlmann, R.; Schroter, S.; Bossert, J.; Jandt, K. D. *Advanced Functional Materials* **2008**, *18*, 1723–1731.
- [136] Gibbs-Davis, J. M.; Hayes, P. L.; Scheidt, K. A.; Geiger, F. M. *Journal of the American Chemical Society* **2007**, *129*, 7175–7184.
- [137] Konek, C. T.; Musorrafiti, M. J.; Al-Abadleh, H. A.; Bertin, P. A.; Nguyen, S. T.; Geiger, F. M. *Journal of the American Chemical Society* **2004**, *126*, 11754–11755.
- [138] Chiu, C. S.; Lee, H. M.; Gwo, S. *Langmuir* **2010**, *26*, 2969–2974.
- [139] Kanazaki, S.; Kawakami, H.; Nagaoka, S.; Kubota, S. *Journal of Biomaterials Science, Polymer Edition* **2003**, *14*, 469–479.
- [140] Kawakami, H.; Kanno, M.; Nagaoka, S.; Kubota, S. *Journal of Biomedical Materials Research, Part A* **2003**, *67A*, 1393–1400.
- [141] Kim, C.; Gurau, M. C.; Cremer, P. S.; Yu, H. *Langmuir* **2008**, *24*, 10155–10160.
- [142] Lu, X. L.; Han, J. L.; Shephard, N.; Rhodes, S.; Martin, A. D.; Li, D. W.; Xue, G.; Chen, Z. *Journal of Physical Chemistry B* **2009**, *113*, 12944–12951.
- [143] Kweskin, S. J.; Komvopoulos, K.; Somorjai, G. A. *Applied Physics Letters* **2006**, *88*, 134105.
- [144] Chen, C. Y.; Wang, J.; Chen, Z. *Langmuir* **2004**, *20*, 10186–10193.
- [145] Chen, C. Y.; Clarke, M. L.; Wang, J.; Chen, Z. *Physical Chemistry Chemical Physics* **2005**, *7*, 2357–2363.
- [146] Basnayake, R.; Peterson, G. R.; Casadonte, D. J.; Korzeniewski, C. *Journal of Physical Chemistry B* **2006**, *110*, 23938–23943.
- [147] Noguchi, H.; Hiroshi, M.; Tominaga, T.; Gong, J. P.; Osada, Y.; Uosaki, K. *Physical Chemistry Chemical Physics* **2008**, *10*, 4987–4993.
- [148] Dreesen, L.; Humbert, C.; Hollander, P.; Mani, A. A.; Ataka, K.; Thiry, P. A.; Peremans, A. *Chemical Physics Letters* **2001**, *333*, 327–331.
- [149] Bain, C. D.; Davies, P. B.; Ward, R. N. *Langmuir* **1994**, *10*, 2060–2063.
- [150] Laibinis, P. E.; Bain, C. D.; Nuzzo, R. G.; Whitesides, G. M. *Journal of Physical Chemistry* **1995**, *99*, 7663–76.

- [151] Ward, R. N.; Davies, P. B.; Bain, C. D. *Journal of Physical Chemistry B* **1997**, *101*, 1594–1601, Article.
- [152] Daschbach, J. L.; Fischer, P. R.; Gragson, D. E.; Demarest, D.; Richmond, G. L. *Journal of Physical Chemistry* **1995**, *99*, 3240–3250.
- [153] Ostroverkhov, V.; Waychunas, G. A.; Shen, Y. R. *Physical Review Letters* **2005**, *94*, 046102/1–046102/4.
- [154] Ostroverkhov, V.; Waychunas, G. A.; Shen, Y. R. *Chemical Physics Letters* **2004**, *386*, 144.
- [155] Hopkins, A. J.; Schrödle, S.; Richmond, G. L. *Langmuir* **2010**, *26*, 10784–10790.
- [156] McFearin, C. L.; Richmond, G. L. *Journal of Physical Chemistry C* **2009**, *113*, 21162–21168.
- [157] Du, Q.; Freysz, E.; Shen, Y. R. *Physical Review Letters* **1994**, *72*, 238–241, Article.
- [158] Becraft, K. A.; Richmond, G. L. *Langmuir* **2001**, *17*, 7721–7724.
- [159] Pivovarov, S. *Journal of Colloid and Interface Science* **2008**, *319*, 374–376.
- [160] Melnikov, S. M.; Holtzel, A.; Seidel-Morgenstern, A.; Tallarek, U. *Journal of Physical Chemistry C* **2009**, *113*, 9230–9238.
- [161] Becraft, K. A.; Moore, F. G.; Richmond, G. L. *Physical Chemistry Chemical Physics* **2004**, *6*, 1880–1889.
- [162] Scatena, L. F.; Richmond, G. L. *Journal of Physical Chemistry B* **2004**, *108*, 12518–12528.
- [163] Scatena, L. F.; Richmond, G. L. *Chemical Physics Letters* **2004**, *383*, 491–495.
- [164] Tang, E.; Di Tommaso, D.; de Leeuw, N. H. *Journal of Chemical Physics* **2009**, *130*, 234502–9.
- [165] Marcus, Y. *Journal of the Chemical Society, Faraday Transactions 1: Physical Chemistry in Condensed Phases* **1987**, *83*, 339–349.
- [166] Haller, I. *Journal of the American Chemical Society* **1978**, *100*, 8050–8055.
- [167] Popat, K. C.; Johnson, R. W.; Desai, T. A. *Surface and Coatings Technology* **2002**, *154*, 253–261.
- [168] Marcinko, S.; Fadeev, A. Y. *Langmuir* **2004**, *20*, 2270–2273.

- [169] Franks, F.; Desnoyers, J. E. *Water Science Reviews* **1985**, *1*, 171–232.
- [170] Eisenthal, K. B. *Chemical Reviews* **1996**, *96*, 1343–1360.
- [171] Dixit, S.; Poon, W. C. K.; Crain, J. *Journal of Physics-condensed Matter* **2000**, *12*, L323–L328.
- [172] Dixit, S.; Crain, J.; Poon, W. C. K.; Finney, J. L.; Soper, A. K. *Nature* **2002**, *416*, 829–832.
- [173] Guo, J. H.; Luo, Y.; Augustsson, A.; Kashtanov, S.; Rubensson, J. E.; Shuh, D. K.; Agren, H.; Nordgren, J. *Physical Review Letters* **2003**, *91*, 157401.
- [174] Ambekar, R. P.; Bogy, D. B.; Bhatia, C. S. *Journal of Tribology-transactions of the Asme* **2009**, *131*, 031901.
- [175] Ward, R. N.; Davies, P. B.; Bain, C. D. *Journal of Physical Chemistry* **1993**, *97*, 7141–7143.
- [176] Schwartz, M.; Moradi-Araghi, A.; Koehler, W. H. *Journal of Molecular Structure* **1980**, *63*, 279–285.
- [177] Schwartz, M.; Moradi-Araghi, A.; Koehler, W. H. *Journal of Molecular Structure* **1982**, *81*, 245–252.
- [178] Lavalley, J. C.; Sheppard, N. *Spectrochimica Acta Part A-molecular Spectroscopy* **1972**, *A 28*, 2091–&.
- [179] Gruenloh, C. J.; Florio, G. M.; Carney, J. R.; Hagemester, F. C.; Zwier, T. S. *Journal of Physical Chemistry A* **1999**, *103*, 496–502.
- [180] Ma, G.; Allen, H. C. *Journal of Physical Chemistry B* **2003**, *107*, 6343–6349.
- [181] Buck, U.; Huisken, F. *Chemical Reviews* **2000**, *100*, 3863–3890.
- [182] Gonzalez, L.; Mo, O.; Yanez, M. *Journal of Chemical Physics* **1998**, *109*, 139–150.
- [183] Huisken, F.; Mohammad-Pooran, S.; Werhahn, O. *Chemical Physics* **1998**, *239*, 11–22.
- [184] Ward, R. N.; Duffy, D. C.; Davies, P. B.; Bain, C. D. *Journal of Physical Chemistry* **1994**, *98*, 8536–8542.
- [185] Liu, W.-T.; Zhang, L.; Shen, Y. *Chemical Physics Letters* **2005**, *412*, 206–209.
- [186] Wang, H. F.; Yan, E. C. Y.; Liu, Y.; Eisenthal, K. B. *Journal of Physical Chemistry B* **1998**, *102*, 4446–4450.

- [187] Chen, H.; Gan, W.; Lu, R.; Guo, Y.; Wang, H. F. *Journal of Physical Chemistry B* **2005**, *109*, 8064–8075.
- [188] Windsor, R.; Neivandt, D. J.; Davies, P. B. *Langmuir* **2001**, *17*, 7306–7312.
- [189] Casford, M. T. L.; Davies, P. B.; Neivandt, D. J. *Langmuir* **2003**, *19*, 7386–7391.
- [190] Windsor, R.; Neivandt, D. J.; Davies, P. B. *Langmuir* **2002**, *18*, 2199–2204.
- [191] Kim, J.; Koffas, T. S.; Lawrence, C. C.; Somorjai, G. A. *Langmuir* **2004**, *20*, 4640–4646.
- [192] Casford, M. T. L.; Davies, P. B.; Neivandt, N. J. *Langmuir* **2006**, *22*, 3105–3111.
- [193] Chen, Z.; Ward, R.; Tian, Y.; Malizia, F.; Gracias, D. H.; Shen, Y. R.; Somorjai, G. A. *Journal of Biomedical Materials Research* **2002**, *62*, 254–264.
- [194] Kim, J.; Somorjai, G. A. *Journal of the American Chemical Society* **2003**, *125*, 3150–3158.
- [195] Wang, J.; Even, M. A.; Chen, X.; Schmaier, A. H.; Waite, J. H.; Chen, Z. *Journal of the American Chemical Society* **2003**, *125*, 9914–9915.
- [196] Chen, X.; Clarke, M. L.; Wang, J.; Chen, Z. *International Journal of Modern Physics B: Condensed Matter Physics, Statistical Physics, Applied Physics* **2005**, *19*, 691–713.
- [197] Chen, X. Y.; Wang, J.; Sniadecki, J. J.; Even, M. A.; Chen, Z. *Langmuir* **2005**, *21*, 2662–2664.
- [198] Wang, J.; Clarke, M. L.; Chen, X.; Even, M. A.; Johnson, W. C.; Chen, Z. *Surface Science* **2005**, *587*, 1–11.
- [199] Phillips, D. C.; York, R. L.; Mermut, O.; McCrea, K. R.; Ward, R. S.; Somorjai, G. A. *Journal of Physical Chemistry C* **2007**, *111*, 255–261.
- [200] Gaudin, A. M.; Fuerstenau, D. W. *Transactions of the American Institute of Mining, Metallurgical and Petroleum Engineers* **1955**, *202*, 66–72.
- [201] Fuerstenau, D. W. *Journal of Physical Chemistry* **1956**, *60*, 981–985.
- [202] Fuerstenau, M. C.; Han, K. N. *Journal of Colloid and Interface Science* **2002**, *256*, 175–182.

- [203] Fuerstenau, D. W.; Jia, R. H. *Colloids and Surfaces A-physicochemical and Engineering Aspects* **2004**, *250*, 223–231.
- [204] Fuerstenau, D. W.; Pradip, *Advances In Colloid and Interface Science* **2005**, *114*, 9–26.
- [205] Chernyshova, I. V.; Rao, K. H.; Vidyadhar, A.; Shchukarev, A. V. *Langmuir* **2001**, *17*, 775–785.
- [206] Vidyadhar, A.; Rao, K. H.; Chernyshova, I. V.; Pradip,; Forssberg, K. S. E. *Journal of Colloid and Interface Science* **2002**, *256*, 59–72.
- [207] Tyrode, E.; Rutland, M. W.; Bain, C. D. *Journal of the American Chemical Society* **2008**, *130*, 17434–17445.
- [208] Wang, X. M.; Liu, J.; Du, H.; Miller, J. D. *Langmuir* **2010**, *26*, 3407–3414.
- [209] Becraft, K. A.; Moore, F. G.; Richmond, G. L. *Journal of Physical Chemistry B* **2003**, *107*, 3675–3678.
- [210] Becraft, K. A.; Richmond, G. L. *Journal of Physical Chemistry B* **2005**, *109*, 5108–5117.
- [211] Moore, F. G.; Becraft, K. A.; Richmond, G. L. *Applied Spectroscopy* **2002**, *56*, 1575–1578.
- [212] Tillman, N.; Ulman, A.; Schildkraut, J. S.; Penner, T. L. *Journal of the American Chemical Society* **1988**, *110*, 6136–6144.
- [213] Mirji, S. A. *Surface and Interface Analysis* **2006**, *38*, 158–165.
- [214] Israelachvili, J. *Intermolecular and Surface Forces*; Academic Press: San Diego, CA, 1992.
- [215] Smart, B. E. In *Organofluorine Chemistry: Principles and Commercial Applications*; Banks, R. E., Smart, J. C., B. E. and Tatlow, Eds.; Topics in Applied Chemistry; Plenum Press: New York, New York, 1994; Chapter 3, pp 57–89.
- [216] Stone, M. T.; da Rocha, S. R. P.; Rossky, P. J.; Johnston, K. P. *Journal of Physical Chemistry B* **2003**, *107*, 10185–10192.
- [217] Nordstierna, L.; Furo, I.; Stilbs, P. *Langmuir* **2006**, *22*, 7969–7974.
- [218] Rogers, S. E.; Eastoe, J.; Hudson, L.; Gold, S.; Heenan, R. K.; Grillo, I. *Journal of Colloid and Interface Science* **2009**, *330*, 437–442.

- [219] *Flotation : A. M. Gaudin Memorial Volume*; Fuerstenau, M., Ed.; American Institute of Mining, Metallurgical, and Petroleum Engineers: New York, 1976; Vol. 278.
- [220] Kanan, S. M.; Tripp, C. P. *Langmuir* **2001**, *17*, 2213–2218.
- [221] Li, H. Y.; Tripp, C. P. *Langmuir* **2005**, *21*, 2585–2590.
- [222] Wu, L.; Forsling, W. *Journal of Colloid and Interface Science* **1995**, *174*, 178–184.
- [223] Fa, K. Q.; Paruchuri, V. K.; Brown, S. C.; Moudgil, B. M.; Miller, J. D. *Physical Chemistry Chemical Physics* **2005**, *7*, 678–684.
- [224] Franks, G. V.; Meagher, L. *Colloids and Surfaces, A: Physicochemical and Engineering Aspects* **2003**, *214*, 99–110.
- [225] Schrodle, S.; Moore, F. G.; Richmond, G. L. *Journal of Physical Chemistry C* **2007**, *111*, 10088–10094.
- [226] Schrodle, S.; Moore, F. G.; Richmond, G. L. *Journal of Physical Chemistry C* **2007**, *111*, 8050–8059.
- [227] Schrodle, S.; Richmond, G. L. *ChemPhysChem* **2007**, *8*, 2315–2317.
- [228] Schrodle, S.; Richmond, G. L. *Journal of the American Chemical Society* **2008**, *130*, 5072–5085.
- [229] Drelich, J.; Jang, W. H.; Miller, J. D. *Langmuir* **1997**, *13*, 1345–1351.
- [230] Free, M. L.; Miller, J. D. *Langmuir* **1997**, *13*, 4377–4382.
- [231] Mielczarski, E.; Mielczarski, J. A.; Cases, J. M.; Rai, B.; Pradip, *Colloids and Surfaces, A: Physicochemical and Engineering Aspects* **2002**, *205*, 73–84.
- [232] Holmgren, A.; Wu, L. M.; Forsling, W. *Spectrochimica Acta, Part A: Molecular and Biomolecular Spectroscopy* **1994**, *50*, 1857–1869.
- [233] Hu, Y.; Lu, Y.; Veeramasuneni, S.; Miller, J. D. *Journal of Colloid and Interface Science* **1997**, *190*, 224–231.
- [234] Miller, J. D.; Fa, K.; Calara, J. V.; Paruchuri, V. K. *Colloids and Surfaces, A: Physicochemical and Engineering Aspects* **2004**, *238*, 91–97.
- [235] Assemi, S.; Nalaskowski, J.; Miller, J. D.; Johnson, W. P. *Langmuir* **2006**, *22*, 1403–1405.

- [236] McFearin, C. L. Ph.D. thesis, University of Oregon, 2009.
- [237] Mifflin, A. L.; Gerth, K. A.; Geiger, F. M. *Journal of Physical Chemistry A* **2003**, *107*, 9620–9627.
- [238] Gonzalez-Caballero, F.; Pardo, G.; Bruque, J. M. *Anales de Quimica* **1976**, *72*, 345–348.
- [239] Miller, J. D.; Hiskey, J. B. *Journal of Colloid and Interface Science* **1972**, *41*, 567–573.
- [240] Robertson, W. H.; Diken, E. G.; Price, E. A.; Shin, J. W.; Johnson, M. A. *Science* **2003**, *299*, 1367–1372.
- [241] Cabarcos, O. M.; Weinheimer, C. J.; Lisy, J. M.; Xantheas, S. S. *Journal of Chemical Physics* **1999**, *110*, 5–8.
- [242] Bush, M. F.; Saykally, R. J.; Williams, E. R. *ChemPhysChem* **2007**, *8*, 2245–2253.
- [243] Zhang, R.; Hu, S.; Zhang, X. *Aquatic Geochemistry* **2006**, *12*, 123–159.
- [244] Pelzl, G.; Diele, S.; Lose, D.; Ostrovski, B. I.; Weissflog, W. *Crystal Research and Technology* **1997**, *32*, 99–109.
- [245] Davey, T. W.; Warr, G. G.; Asakawa, T. *Langmuir* **2003**, *19*, 5266–5272.
- [246] Broniatowski, M.; Minones, J.; Macho, I. S.; Dynarowicz-Latka, P. *Polish Journal of Chemistry* **2005**, *79*, 1047–1061.
- [247] Bertie, J. E.; Zhang, S. L. L. *Applied Spectroscopy* **1994**, *48*, 176–189.
- [248] Bertie, J. E.; Lan, Z. *Journal of Chemical Physics* **1995**, *103*, 10152–10161.
- [249] Zhuang, X.; Miranda, P. B.; Kim, D.; Shen, Y. R. *Physical Review B* **1999**, *59*, 12632–12640.
- [250] Colles, M. J.; Griffith, J. E. *Journal of Chemical Physics* **1972**, *56*, 3384–3391.